Structural and Kinetics Study of Quantum Size Effect Pb islands grown on Si(111)

A Thesis
Presented to
The Academic Faculty

by

Rui Feng

In Partial Fulfillment
of the Requirements for the Degree
Doctor of Philosophy

School of Physics
Georgia Institute of Technology
December 2006

Structural and Kinetics Study of Quantum Size Effect Pb islands grown on Si(111)

Approved by:

Dr. Edward H. Conrad, Advisor
School of Physics
Georgia Institute of Technology

Dr. Mei-Yin Chou
School of Physics
Georgia Institute of Technology

Dr. Walter A. De Heer
School of Physics
Georgia Institute of Technology

Dr. Phillip First
School of Physics
Georgia Institute of Technology

Dr. W. Brent Carter
School of Materials Science and Engineering
Georgia Institute of Technology

Date Approved: July, 12, 2006

To my parent.

ACKNOWLEDGEMENTS

I would like to express my deepest gratitude to my advisor, Professor Ed. H. Conrad, for his support and guidance in performing this research, and my thesis committee, Professor Mei-Yin Chou, Phil First, Walt De Heer and Brent Carter for their expertise and advise. Special thanks are extended to Professor Andrew Zangwill for his advise and help. I am also grateful to the School of Physics of Georgia Tech. Finally, I would like to thank my parents for their love and support over the years.

TABLE OF CONTENTS

DEDICATION . . . . . **iii**

ACKNOWLEDGEMENTS . . . . . **iv**

LIST OF TABLES . . . . . **vii**

LIST OF FIGURES . . . . . **viii**

SUMMARY . . . . . **xiii**

I INTRODUCTION **1**

1.1 Thin film growth 3

1.1.1 Growth process and modes 3

1.1.2 Theory of Nucleation 6

1.2 Theory of Coarsening 9

1.3 Quantum Size Effect 11

1.3.1 Quantum Well States 12

1.3.2 QSE in physical properties 14

1.3.3 Preferred thickness and stability 16

II SURFACE X-RAY DIFFRACTION EXPERIMENTS **19**

2.1 Introduction 19

2.2 Crystal Lattice 20

2.3 Surface Reconstruction 22

2.4 Experimental Methods 24

2.4.1 Synchrotron X-ray Source at the APS 24

2.4.2 Surface Diffractometer 25

2.4.3 UHV Technology 28

2.4.4 Sample Preparation 29

2.5 Kinematic Theory 31

2.5.1 X-ray Diffraction by a Crystal 31

2.5.2 X-ray Diffraction by a Surface 33

2.6 Specular Reflectivity of Pb/Si(111) System 35

2.6.1 Transverse Rod Scan 37

III INTERFACE STRUCTURE OF PB ISLANDS ON SI(111) 7×7 . . 43

3.1 Introduction . . . 43

3.2 X-ray Scattering at Pb(111) Bragg position . . . 45

3.2.1 Scattering Model . . . 45

3.2.2 Experimental Results . . . 47

3.2.3 Analysis and Discussions . . . 49

3.3 Specular Reflectivity Analysis . . . 52

3.3.1 Structural Model . . . 52

3.3.2 Experimental Results and Analysis . . . 55

3.4 Pb-Si interface Formation during Early Growth . . . 59

3.4.1 Scattering Model . . . 59

3.4.2 Experimental Results and Discussion . . . 60

IV ISLAND COARSENING BEHAVIOR OF PB/SI(111) 7×7 . . . 68

4.1 Introduction . . . 68

4.2 Specular Reflectivity . . . 70

4.3 Diffuse X-ray Scattering . . . 73

4.4 STM Results . . . 82

4.5 Discussions . . . 85

APPENDIX A — GEOMETRY CORRECTION . . . 90

REFERENCES . . . 92

VITA . . . 95

LIST OF TABLES

1.1 Parameter dependencies of the maximum cluster density in the regime of complete condensation. Table from Venables et.al [26]. 9

LIST OF FIGURES

1.1 Schematic diagram of atomic processes in nucleation and growth on surface. Film atoms are shown as open circle and substrate atom as dark circles. Figure from Venables [26]. 4

1.2 Schematic plot of the three epitaxial growth modes: (a) layer by layer or Frank-van-der-Merwe, (b)layer plus island or Stranski-Krastanov with a one-layer wetting layer, (c)island or Volmer-Weber growth mode. Figure from Venables *et al.*[26] 5

1.3 Calculated relative surface energy per surface atom as a function of layer thickness of an integer number N, for (a) freestanding Pb films; (b) Pb films on Si. The dotted curves represent envelope functions for the quantum oscillations. Figure from Hong *et al.*[17] 16

1.4 (a) A 300x300nm STM image of 3.2ML Pb deposited on the Si(111) 7x7, growing into flat-topped, steep-edge islands; (b) the island height histogram with preferred heights at 4, 5 and 7 monolayers of Pb. Figure from Su *et al.*[27] 17

1.5 A kinetic Phase diagram for Pb grown on Si(111) 7x7 for coverage up to 10ML in a temperature range of 120-250K. Preferred island height will increase with bi-layer increment as the coverage or temperature are increased. Figure from Hupalo *et al.*[4] 18

2.1 (a) Cubic unit cell of the *fcc* lattice. The primitive unit cell is shown as the shaded region which contains one atom. (b) Cubic unit cell of the diamond lattice, which is the *fcc* lattice with a two-point basis. The additional atoms to the normal *fcc* sites are shown in open circles. Nearest neighbor bonds have been drawn in solid lines. The (111) direction is shown in a blue dot-dashed line while the plane outlined with red dashed lines is the (111) atomic plane. Figures from Ashcroft *et al.*[49] 21

2.2 Side view of Si(111) atomic layer structure with interlayer spacings shown. A unit cell is marked in a blue frame, which indicates totally six atoms per unit cell. The surface termination is between double layers that has less number of dangling bonds. 22

2.3 The surface structure of Si(111) 7×7 reconstruction.(a) Top view of the first three layers. (b) Side view of the structure that indicating the faulted and unfaulted halve of the 7x7 unit cell. Figure from Takanagi *et al.* [10] 23

2.4 A schematic draw of the structure of an insert device (wriggler or undulator). Magnets of alternating polarities, are separated with distance λ. 25

2.5 The surface diffractometer and UHV chamber in Station 6ID-C, μCAT. Major components are marked. 27

2.6 A schematic drawing of the '4S+2D' diffractometer.[33] The ϕ axis is actually fixed in the experiments. The sense of rotations, laboratory frame, and the incoming X-ray directions are shown as arrows. 28

2.7 X-ray reflectivity growth oscillation measured at anti-Bragg position (l = 1.64). The irregular period of the oscillations at low coverages is due to disordering in the early growth. Beyond ~ 6 oscillations, the period becomes regular and has been used to calibrate the deposition flux. 31

2.8 Surface diffraction rod of the (001) surface of a simple cubic lattice. Figures from Conrad *et al.*[51] 35

2.9 (a) The scattering geometry of the rocking curve method. Since the point detector only measures one point in space, the sample normal is rotated within the scattering plane with incident beam and the detector fixed. (b) Typical transverse scan at Pb(111) Bragg position. The lobe structure is due to inter-islands scattering. 38

2.10 The scattering geometry using a CCD detector from a surface with presence of islands. The incident and reflected angels are lined up then fixed at Bragg reflection positions. The CCD image plate is placed perpendicular to the reflected beam. The top view exhibits the 2D feature of the image. The detector collects scattering within a range of q_y and q_x(perpendicular to q_y along the detector surface). 40

2.11 Images taken with a Mar-165 CCD detector during early growth and after a certain amount of Pb has been deposited. The big bright circular area at the right side of the two images are diffuse around Si(111) Bragg peaks. The small bright spot within the dashed frame are Pb(111) Bragg peaks. A diffuse ring structure shows up with Pb islands present on the surface. . . 42

3.1 Transverse scans measured across the Pb(111) Bragg peak for selected coverages after stepwise depositions. The sample temperature is 227K and the deposition flux was 0.39 ML/min. Solid curves are fits using a Gaussian central peak and a pair of Lorentzians for the diffuse lobes. 48

3.2 Integrated Bragg(open triangle), diffuse(open circle) and total(filled circle) intensity vs. Pb coverage taken at the Pb(111) Bragg position. The dashed curve is the Bragg intensity calculated for $\sigma = 0$. 49

3.3 A schematic structural model illustrating the basic conclusion that the Pb nanocrystals have an interface with the Si substrate rather than with the wetting layer. 51

3.4 Comparison of transverse scans across the Pb(111) and Pb(222) Bragg position. (a) For $\Theta = 3ML$ the diffuse scattering scales with $q_{||}$, indicating correlated inter-island scattering. (b) For $\Theta = 22.25ML$, the diffuse scattering scales with the sample rocking angle $\triangle\omega$, indicating a mosaic-like disorder arising from crystalline defects. 52

3.5 A schematic plot of Pb fcc islands grown on Si(111) substrate. For specular reflectivity, all islands n-layer thick can be represented as one island with a fractional surface coverage parameter, p_n. Note that the wetting layer sits at a height, D_w, that can be different from the island-Si spacing D_0. 54

3.6 X-ray Reflectivity data of 3ML Pb on Si(111)7×7 at 227K(open circles). The intense peaks with certain widthes at $l = 3.27, 6.54$ and 9.81 are the Pb(111), (222) and (333) Bragg peaks, respectively. Blue solid line is the best fit using the model described in the text with wetting layer roughness σ_1 partially 1.02Å&0.0Å and island roughness $\sigma = 0.0$Å. Black dashed line is calculated from the same fit with $\sigma_1 = \sigma = 0.0$Å. Red dashed line is calculated from the same fit with $\sigma_1 = \sigma = 1.02$Å. Green dashed-dot line is the fit with the wetting layer uniformly rough $\sigma_1 = 0.3$Å. 57

3.7 Reflectivity near to Pb(222) and fits with island height distribution peaked at 7, 8 and 9, which are blue dashed, black solid and red dashed lines, respectively. 58

3.8 The Pb Bragg (111), $l = 3.27$, intensity versus Pb coverage for different deposition fluxes((△) 0.032ML/min, (□) 0.062ML/min, (•) 1.36ML/min). Substrate temperature is 227K. Solid lines are fits to model discussed in the text. Insert shows the low coverage intensity and a fit with (solid lines) and without (dashed lines) a 3-site wetting layer model 61

3.9 Ball models for different Pb coverages on the 7×7 unit cell. Black spheres are Si adatoms and large grey spheres are Pb atoms. Small grey spheres are top layer Si atoms and white circles are 2nd layer Si atoms. (a) 0.10ML of Pb on T_1 Si rest atom sites. Side view shows vertical spacing of Pb above the T_1 Si atom. (b) 0.61ML of Pb with 6-, 5-, and 4-fold rings filling the space between Si adatoms. Side view shows vertical spacing of Pb above the Si adatoms. (c) 0.92ML, Pb covers all sites in (b) plus sites above the Si dimers. 63

3.10 A Pb incommensurate film on the Si(111)7×7 surface. Black circles are Si adatoms and open circles are Pb atoms above the surface. The optimum hollow and bridge site Pb positions based on the experimentally determined island-substrate distance. 66

4.1 Specular reflectivities of a 3ML Pb film grow on Si(111)7×7 under different conditions as indicated. Data (a)-(c) were collected with the sample held at the same temperature as deposition. In data set(d) the sample was quenched to 55K immediately after deposition. Solid lines are best fits from the model described in the text, with two wetting layer sites: one rough $\sigma_{w,1} = 1.02$Å and one smooth $\sigma_{w,2} = 0.0$Å. In data (a) we also show fits with island roughness equal to wetting layer roughness $\sigma = \sigma_{w,1}$ (dashed line), smooth wetting layer $\sigma_{w,1} = 0$ (dotted line), and a uniformly rough wetting layer $\sigma_{w,2} = \sigma_{w,1} = 0.3$Å (dashed dot-dot line). Vertical dashed lines mark the position of two prominent interference fringes for scans (a)-(c). Solid vertical lines mark the position of two prominent interference fringes for scan (d). . 71

4.2 Island height histogram for two different 3ML Pb films grown at 227K. Solid bars are for a film that was quenched to 55K after deposition with a mean island height of 8ML. Grey bars are for a film held at 227K after deposition showing a mean island height of 10ML. 72

4.3 Island densities versus temperature for 1.2ML Pb on Si(111). It demonstrates the exponential dependence on substrate temperature T. These data were obtained from X-ray diffuse scattering measured after the deposition of 1.2 ML of Pb for various temperature at deposition flux 0.404 ML/min. The solid line is a exponential fit with energy barrier of 0.316 eV. 74

4.4 (a) Island densities vs time after deposition. The time evolution of the island density were obtained from X-ray diffuse scattering measured after the deposition of 1.2 ML of Pb at 208 K for various deposition fluxes F. The solid curves are fits using Eqn.(4.1a) with $\beta = 1$. It demonstrates the breakdown of the Ostwald ripening scaling: The curves do not approach each other at long times. (b) Normalized island density n/n_0 versus time scaled by flux. The curves tend to overlap, implying that n_0 is independent of the decay time, and the decay time is inversely proportional to the flux. 75

4.5 Simulated values of island density for coarsening (Ostwald ripening) versus time. The solid curve is for a high initial density and the dashed curve is for a low initial density. 76

4.6 (a) Coarsening time constant versus flux rate. The time constant changes quickly with flux $\tau \propto F^{-0.98\pm0.10}$, showing that islands formed with faster deposition tend to coarsen faster. (b) Initial island density n_0 versus flux rate, indicating that n_0 depends only weakly on flux $n_0 \propto F^{0.16\pm0.06}$. . . . 77

4.7 (a) Island densities versus time after deposition. These data are collected by a CCD detector after the deposition of 1.2 ML of Pb at 227 K for various deposition fluxes F. The solid curves are a fit using Eqn.(4.1a) with $\beta = 1$. (b) Normalized island density n/n_0 versus time scaled by flux. The curves tend to overlap, implying that n_0 is independent of the decay time, and the decay time is inversely proportional to the flux. 78

4.8 (a) Coarsening time constant versus flux rate. These data are collected by a CCD detector after the deposition of 1.2 ML of Pb at 227 K for various deposition fluxes F. The time constant vary strongly with flux $\tau \propto F^{-1.14}$, showing that islands formed with faster deposition tend to coarsen faster. (b) Initial island density n_0 versus flux rate, indicating that n_0 has a power law dependence on flux. 79

4.9 ((a) Island coarsening time versus flux rate at two coverages: 1.2ML and 2.0ML. The substrate temperature was maintained at 227K. The power law dependence on flux are given. (b) Initial island density versus flux rate for the two coverages. 81

4.10 (a) Coarsening time versus $1/k_BT$ at different flux rates. The Pb coverage is 2ML. (b) Initial island density versus $1/k_BT$ at different flux rates. . . . 82

4.11 STM images of the coarsening of 1.6 ML Pb deposited on Si(111) 7×7at 203 K at a flux of 0.5ML/min. The times after deposition are shown for each image. The scale is $250 \times 250\text{nm}^2$ for (a) and $500 \times 500\text{nm}^2$ for (d). The tunnelling parameters were 2V at 1 nA. Each scan takes 0.5 min. The island height is marked on top of each island for image (a), (d), and (f) (height is measured with respect to the Pb wetting layer.) It can be seen that 3-layer islands are less stable than 4-layer ones and both of these are less stable than 7-layer islands. 83

4.12 Histograms of the island height distribution for 1.6 ML grown at 203 K, measured 5 min after (black) and 74 min after deposition (cross-hatched). (a) shows a high flux rate deposition, 0.5ML/min, leading to a broad initial island height distribution with fast decay of unstable islands. (b) shows a low flux deposition, 0.05ML/min, leading to a narrower initial island height distribution with little change over time. 84

SUMMARY

The growth of Pb film on Si(111) is an unusual metal-semiconductor system. For a certain temperature range, Pb films have been found to grow in steep-edge and flat-top islands with uniform height on the surface. This specific film morphology has been correlated to Quantum Size Effect (QSE) that the objects size or film thickness affects the electronic structure of the films and results in a certain thickness more stable than others. The technique of X-ray diffraction has the advantages of long penetration length and high statistics over a large area, therefore it has been used to investigate the influence of QSE on the growth of Pb on the Si(111) 7×7 surface. It is demonstrated that the structure of Pb islands and the associated wetting layer are consistent with effects of quantum confinement. Specular reflectivity of 3 monolayer (ML) Pb films grown on the substrate at 227K has conclusively shown that the Pb islands do not reside on top of a Pb wetting layer, but directly on top of the Si substrate. The nucleating Pb nanocrystals transform the highly disordered Pb wetting layer beneath the islands into well-ordered *fcc* Pb. The surface then consists of *fcc* Pb islands directly on top of the Si surface with the disordered wetting layer between the islands. Moreover, it is found that QSE leads to novel behavior for the coarsening evolution of the Pb islands. The diffuse X-ray scattering experiments have been carried out as functions of temperature, deposition rate and coverage. A structural evolution of Pb islands was observed after deposition at very low coverages ($0.2 - 1.0$ ML above the wetting layer coverage). Contrary to the classical scaling theory of nucleation and Ostwald ripening, a much lower island density is achieved with coarsening after deposition at high rather than low flux rates. The time constants of coarsening are found to be orders of magnitudes shorter than what is expected from the Gibbs-Thompson analysis. The rapid evaporation of unstable 3-layer islands shown in complementary STM suggests the role of QSE in the more efficient decay mechanism operating at low temperatures. These results have important applications for the controlled growth of nanostructures.

CHAPTER I

INTRODUCTION

Epitaxial growth of thin films is interesting from both a technological and a fundamental point of view. As devices reach nanometer-length scales, existing fabrication methods have physical limitations such as the wavelength limit for lithographical methods. Therefore the fabrication of well-ordered self-assembled nanostructure is very desirable. Furthermore, as the size of a metallic nanostructure shrinks, effects due to electron confinement become significant and introduce new electronic levels. These effects highly depends on the object's size, thus they are known as Quantum Size Effect (QSE). A fundamental understanding of how QSE influence the physical properties of devices' as their size shrinks becomes important. Epitaxial growth is a widely used technique to make such materials with atomic control of the grown structures. The study of epitaxial film growth is motivated by the requirement on the quality of thin films and the structural control of the growth at the atomic level.

A model study of molecular beam epitaxial (MBE) growth typically involves vapor deposition of a certain amount of atoms on a crystalline substrate at a set of growth conditions such as substrate temperature, coverage and deposition flux rate etc. Epitaxial growth of thin films from atoms deposited from the gas phase is a non-equilibrium process which is determined by competition between kinetics and thermodynamics. Understanding this competition makes it possible to control the growth and improve the quality of thin film. Nucleation and growth processes determines the structure of thin film on surfaces. Atomistic structure, the geometrical arrangement of atoms in space, is also an important aspect of thin film growth and has a significant influence on the morphology of a surface or interface. For instance, the interatomic forces determine whether metal atoms on a semiconductor substrate grow layer by layer or into islands. Therefore, the problem of a surface or interface needs to be approached from both macroscopic and atomistic point of view.

Pb on Si(111) is one model system for studying metal-semiconductor interface growth. Since Si is the most widely used material in the semiconductor industry, systems based on Si surfaces are of great technological interest. Furthermore, the structures of Si surfaces have been studied exhaustively over decades and there are sophisticate methods to prepare reproducible Si surfaces such as the well-known Si(111) 7×7 reconstruction.[28] Pb was chosen not only because it neither reacts nor interdiffuses with Si, but also because studies have shown strong quantum confinement effect in the Pb/Si system[3, 5]. Quantum size effects were first observed in Ag/GaAs[30], and later in some other systems such as Pb/Si(111)[1, 2]. When the dimensions of a structure approach the atomic level, or comparable to the Fermi wavelength (λ_F) of electrons in the material, quantum mechanics has a significant impact on the geometry or morphology of the structure. The confinement of electron wave functions in small objects leads to new discrete energy levels that affect its total energy. Conversely, the confinement influences the object's size by selecting those sizes or shapes that minimizes the total energy. Due to this effect, there are size dependences in many properties of the system such as the surface energy, crystal lattice structure and morphology etc. With film thickness on the order of monolayer (ML), a consequence of such an effect is that certain film thicknesses or island heights are more stable than others[5].

In the study of nucleation and coarsening of Pb islands on Si(111) presented here, the role of QSE in the final island morphology after coarsening is clarified. The Pb island density has been found to evolve in time to lower densities in the temperature range of island growth, especially when the films are grown at high flux rates.[59] The initial island nucleation exhibits a weak dependence on the deposition flux, as in standard nucleation theory. However, much lower island densities were observed after deposition at high rather than low flux rates, contrary to the classical scaling theory of nucleation and Ostwald ripening. The coarsening time constants were found to be orders of magnitudes shorter than those determined from Gibbs-Thomson driven decay previously measured on larger Pb crystals.[60, 61] The rapid evaporation of unstable 3-layer islands suggests the presence of another efficient decay mechanism that is related to QSE. These observations indicate that the role of QSE in islands stability has a direct impact on coarsening in this system.

In this chapter, the theory of thin film growth such as growth modes and standard nucleation theory will be reviewed. The theory of the quantum size effect, its role in the growth of Pb on Si(111) and the recent work on it will be briefly reviewed as well.

1.1 Thin film growth

1.1.1 Growth process and modes

Epitaxial thin film growth is a far from equilibrium kinetic process where the growth process is not reversible. Fundamental physical processes involved in thin film growth are nucleation, island growth and island coalescence. The process of epitaxial growth usually starts with nucleation of an initial distribution of two-dimensional or three-dimensional stable clusters from the deposition atom gas. These clusters continue to grow by capturing single atoms from the supersaturated adatom sea on the surface. Eventually stable clusters start to impinge on each other as their size becomes comparable to their separation or by direct mobility of the cluster across the substrate [31].

The early stage of thin film growth involves the arrival and condensation of atoms on the surface, their diffusion along the surface and their nucleation into stable clusters. The individual atomic processes that determine the initial stage of growth are illustrated in Fig. 1.1. When atoms approach the surface of a substrate, condensation or a solid-state phase transformation takes place when the atoms dissipate most of their kinetic energy into substrate lattice vibrations during the collision, and end up with energies below the adsorption energy. Condensation of atoms from the vapor phase is represented by an arrival rate, $R = p(2\pi mkT_0)^{-1/2}$ where m is the molecular weight, k is Boltzmann's constant and T_0 is the source temperature. When an atom arrives on the substrate, it might re-evaporate or be adsorbed and become a single atom or adatoms on the surface. The single atom then diffuses on the surface until it is lost by one of several processes. These processes include, (i)nucleation of clusters; (ii) capture by special sites or existing clusters; (iii) possibly interdiffusion in the substrate and re-evaporation. There is a characteristic energy related with each of thermally activated process. For a metal atom impinging on a semiconductor substrate at low temperatures, the energy transfer is highly efficient and

re-evaporation cannot take place, which is the so-called complete condensation limit[26].

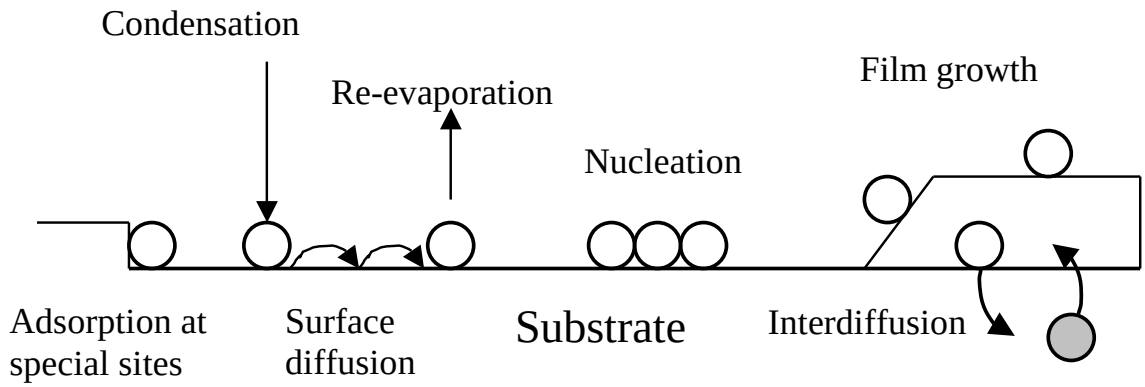

Figure 1.1: Schematic diagram of atomic processes in nucleation and growth on surface. Film atoms are shown as open circle and substrate atom as dark circles. Figure from Venables [26].

The final macroscopic state of the film is kinetically determined by the route taken through the various reaction paths indicated in Fig. 1.1. Some of the processes might be kinetically forbidden, such as interdiffusion with the substrate. Some other processes might be in local thermodynamic equilibrium such as the growth of small clusters which decay rapidly, where the growth and decay processes proceed in two opposite direction at equal rates. Due to the non-equilibrium nature of the processes, the theory of film growth requires each process be described by kinetic rate equations that will be introduced in the next section 1.2.

In addition to the theoretical approach, the process of film growth can be described more phenomenologically. It is generally accepted that there are three possible modes of thin film growth on surfaces, the island (Volmer-Weber) mode, the layer plus island (Stranski-Krastanov) mode, and the layer-by-layer (Frank-van der Merwe) mode [26], shown in Fig. 1.2(a), 1.2(b) and 1.2(c), respectively. The growth mode that a system chooses is mainly determined by comparing the binding energy between atoms and the substrate E_s to the binding energy between two deposited atoms E_b. The lattice mismatch between substrate and the film also affects the growth mode since a strain energy introduced by the mismatch increases with the film thickness.

The layer mode occurs when $E_s > E_b$ so that the depositing atoms are more strongly

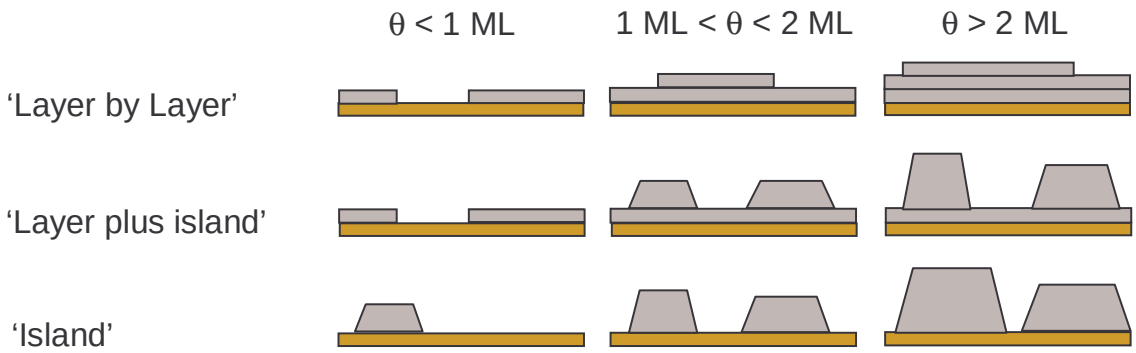

Figure 1.2: Schematic plot of the three epitaxial growth modes: (a) layer by layer or Frank-van-der-Merwe, (b)layer plus island or Stranski-Krastanov with a one-layer wetting layer, (c)island or Volmer-Weber growth mode. Figure from Venables *et al.*[26]

bound to the substrate than to each other, and the decrease of the binding energy with film thickness is monotonically towards the value of a bulk crystal. In this mode, it is expected that two-dimensional (2D) clusters will form on the top layer, and grow into a complete monolayer on the surface. Each new layer will only starts to grow after the last one has been completed. The layer growth mode is observed in some metal-metal systems and semiconductor growth on semiconductor systems etc. Island mode growth has the opposite characteristic in that small clusters, nucleated on the substrate in the formation stage, will grow into islands. It occurs when $E_s < E_b$ so that the depositing atoms are more strongly bound to each other than to the substrate. In this mode small three-dimensional (3D) clusters form directly on the bare substrate. This mode is observed in many systems of metals growing on insulators.

The layer plus island growth mode is an intermediate case, which is found to be common in growth systems such as metal-metal and metal-semiconductors. After the first, or a couple monolayers are formed on the substrate surface, the monotonic decrease in binding energy is disturbed, therefore islands could grow from either 2D or 3D clusters on top of the wetting layer. The film switches to the island growth mode because the binding energy between the atoms and the intermediate layer increases so that the layer growth mode is no longer favorable any more. There are many factors influencing when this mode happens such as the lattice mismatch or when the symmetry of the overlayer is not able to continue in the

bulk of the crystal. The lattice of the film manages to adjust to the substrate lattice at the expense of a strain energy. The strain energy results in a high free energy of the interface and therefore makes the transition from layer to islands growth mode occur.

1.1.2 Theory of Nucleation

The diffusion of adatoms across the surface is the mechanism by which atoms find their path to incorporate and reproduce the crystal structure. A simple model of surface diffusion is derived from a two-dimensional random walk of an adatom on adsorption sites [36]. The diffusion coefficient D, is typically written as,

$$D = \frac{\nu}{4N_0}, \tag{1.1}$$

where ν is the hopping frequency and N_0 is the number of adsorption sites per unit area. The constant in the denominator is 4 for two-dimensional diffusion. The hopping frequency is usually determined by surface vibrations and follows an Arrhenius law,

$$\nu = \nu_0 e^{-E_D/k_B T}, \tag{1.2}$$

where the prefactor ν_0 is referred to as the attempt frequency and E_D is the energy barrier for diffusion. The dependence of thin film morphology on the surface temperature mainly originates from the fact that surface diffusion is a thermally activated process.

The process known as nucleation occurs when an adatom finds one or more other adatoms to form a cluster, or join an existing cluster. It is assumed that the cluster becomes stable (i.e, grows in size rather than shrinking on average) once it exceeds a critical size i. At low temperature, i is expected to be 1. The nucleation process is important in thin film growth because what happens during the nucleation stage influences the ultimate film structure. The driving force for cluster nucleation and growth can be described by the Gibbs free energy of formation of a cluster of size r. In the continuum thermodynamic limit, the total Gibbs free energy is given as [31],

$$G(r) = -V_c(r)\triangle\mu\triangle\rho + \sum_{i=1}^{3}\gamma_i S_i(r), \tag{1.3}$$

with $V_c(r)$ the volume of the cluster, $\triangle\mu$ and $\triangle\rho$ the differences of chemical potential and atomic density in the condensed and vapor adatom phases, respectively, γ_i the surface

tensions and S_i the corresponding surface areas. There are three interfacial tensions, i.e. the surface tension of the cluster, γ_{cv}, the substrate to vacuum, γ_{sv} and cluster to substrate, γ_{cs}. The surface tensions and their areas are subject to the actual cluster shape. The first volume term in the total energy decreases with cluster size while the second surface term increases with cluster size due to the increase of surface area. The balance condition $\mathrm{d}G(r)/\mathrm{d}r{=}0$ estimates the stable cluster size.

In the initial stage of growth, nucleation is the dominant process because it reduces the total energy with atoms from the supersaturated adatom phase bonding to form clusters. With more clusters on the surface, the single atom concentration reaches steady state when the arrival flux is balanced by single atoms capture to existing clusters. Eventually nucleation reaches its maximum density when the adatom concentration is significantly reduced or the surface coverage of clusters is too large to be negligible. As a result, existing clusters continue grow without new clusters nucleating. Other processes contribute to the decrease of the cluster density, such as ripening and coalescence. These will be discussed in Sec. 1.2.

The rate equation model was developed by Zinsmeister, Stowell and Venables *et al.* etc.[26][37] for standard nucleation theory, using kinetic rate equations for the surface number density N_j of clusters consisting of j atoms. The surface number density is defined as the number of clusters per surface area. By defining stable clusters as those with size exceeding critical size i, and unstable clusters with those with $j < i$, the sum of all stable clusters N_x is written as,

$$N_x = \sum_{j=i+1}^{\infty} N_j. \tag{1.4}$$

In the case of nucleation under a constant deposition rate, both the single adatom phase and the condensed phase exist on the surface. Under the assumption that only single adatoms are mobile on the surface, the kinetic rate equations for the number density of various cluster sizes can be simplified into three groups [26],

$$\frac{dN_1}{dt} = R - \frac{N_1}{\tau_a} - \frac{d(N_x w_x)}{dt}, \tag{1.5}$$

$$\frac{dN_j}{dt} = 0, \text{ for j} \leq i, \tag{1.6}$$

$$\frac{dN_x}{dt} = \sigma_i D N_1 N_i - 2N_x \frac{dZ}{dt}, \tag{1.7}$$

with N_1 the single adatom concentration, N_j the concentration of clusters with j atoms, σ_i the capture cross section of momomers by clusters of i atoms, $N_x w_x$ the total number of atoms in stable clusters and Z the fractional coverage of the surface. The capture number σ_i describes the diffusion flow of monomers to an i-cluster, which is proportional to the active surface of the cluster in capturing process. Equation (1.5) gives the number change of monomers. The first two terms represent the deposition and re-evaporation process, respectively. The deposition rate R is defined as the number of atoms deposited per unit time and surface area. The time constant τ_a is for the re-evaporation, which can not take place in complete condensation. The last term in Eqn.(1.5) represents the total loss of single atoms to stable clusters with the average number of atoms w_x per cluster. Since clusters with number of atoms less than the critical cluster size i decay fast, their net growth rate is zero, as shown in Eqn.(1.6). There are two important terms affecting the density of stable islands N_x, shown in Eqn.(1.7). The first term is the nucleation rate as the number of stable islands formed per unit time and unit area on the surface, given by the areal density of critical clusters N_i and the rate at which these clusters gain an additional atom. The second term of Eqn.(1.7) is due to coalescence which causes N_x to decrease. The surface fractional coverage Z is related with N_x and w_x, and depends on whether it is 2D or 3D growth, assuming the shape of the stable islands being constant. Constant and simple shapes of clusters can be treated analytically. For instance, $Z = N_x w_x \Omega^{2/3}$ for 2D growth as a monolayer disk, where Ω is the atomic volume of the atom in the cluster. While this relation becomes $Z = N_x \pi^{1/3} (3\Omega w_x/2)^{2/3}$ for 3D growth as a hemisphere.

Based on the idea of local equilibrium achieved due to the decay of clusters size less than i, the relationship between N_1 and N_i was derived as the Walton Equilibrium relation[26]:

$$N_i = C_i {N_0}^{1-i} {N_1}^i e^{E_i/k_B T}, \tag{1.8}$$

where N_0 is the available nucleation sites per unit area, E_i is the binding energy of the critical cluster and C_i is a statistical weighting factor. When Z is not ignorable, the nucleation rate needs to multiply a simple correction for finite surface coverage $1 - Z$ since nucleation is presumed to only take place on the uncovered area of the substrate.

Table 1.1: Parameter dependencies of the maximum cluster density in the regime of complete condensation. Table from Venables et.al [26].

Regime	3D Island	2D Island
Complete	$p = 1/(i + 2.5)$	$p = i/(i + 2)$
	$E = (E_i + iE_d)/(i + 2.5)$	$E = (E_i + iE_d)/(i + 2)$

The rate equations (1.5)-(1.7) can be solved to give expressions for $N_x(t)$, the number density of stable clusters. The nucleation process can be divided into an initial transient stage and a subsequent steady nucleation stage. The transient stage occurs initially, in which the single atoms density N_1 increases linearly with time, $N_1 = Rt$. This stage goes on until the capture of diffusing single atoms by stable cluster becomes significant, and eventually the right side of Eqn.(1.5) reaches zero, which gives the steady-state condition $dN_1/dt = 0$. The scaling of N_x with deposition flux and temperature can be summarized as[26, 31],

$$\frac{N_x}{N_0} \sim (\frac{R}{N_0\nu})^p e^{E/k_BT}. \tag{1.9}$$

Table 1.1 lists parameters, p and E, for complete condensation of 2D and 3D islands. The expression of N_x shows fractional power dependence on flux R and exponential dependence on substrate temperature T.

1.2 Theory of Coarsening

Once the deposition flux is turned off after an initial island density is established through nucleation, the island density begins to decrease due to coarsening (Ostwald ripening). In Ostwald ripening big islands grow in size at the expense of small islands. This process, and its inherent dependence on island radius, is controlled by the chemical potential difference between islands and a 2D gas of adatoms. Smaller islands have a higher surface-to-volume ratio causing a higher surface tension and thus an increase of the chemical potential. The discrepancy of the surface tension of islands with different sizes is much smaller than in the nucleation stage where the volume free energy of clusters reduces significantly from the vapor phase. Therefore the coarsening rate is expected to be much slower than the nucleation rate. The Gibbs-Thomson effect is the expected driving force of cluster coarsening[54, 31].

The Gibbs-Thomson equation was applied to island growth under a zero deposition rate condition, that gives the concentration of single 2D atom gas in equilibrium with an island of radius r [55, 31],

$$\rho_e(r) = \rho_\infty \exp 2\gamma/(r\rho_s k_B T), \tag{1.10}$$

where ρ_∞ is the equilibrium concentration of an infinite large island, γ is the surface tension between the island and the substrate, and ρ_s is the density of the solid island. This equation can be applied to clusters when the cluster equilibrium shape remains unchanged. For 2D islands, the formula of the equilibrium concentration was derived as [31],

$$\rho_e(r) = \rho_\infty \exp\left(\frac{\gamma_{cv} + \gamma_{cs} - \gamma_{sv}}{h} + \frac{\gamma_e}{r}\right)/(\rho_s k_B T), \tag{1.11}$$

with h the height and γ_e the surface tension of the cylindrical island edge. The actual adatom concentration outside the island might be different from the Gibbs-Thomson value due to a kinetic barrier that an adatom must overcome to enter or leave the island.

The rate of material flux is limited by the mass transport between islands. There are two possible rate limited mechanisms for the mass transport, (i) surface diffusion and (ii) interface reaction limited transfer due to the energy difference between the equilibrium concentration at the surface of the islands, $\rho_e(r)$, and the actual concentration at the surface, $\rho(r)$. In the diffusion limited case, the driving force of mass transport is the difference of the actual adatom concentration at the island surface $\rho(r)$, and the average free adatom concentration between islands ρ_0. The interface limited case involves a kinetic barrier for atoms to detach from the island. The energy difference for an adatom to enter or stay outside an island determines the ratio of monomer concentration at the island edge site to its equilibrium concentration, $\rho_e(r)$, given by Eqn.(1.10). For a steady-state condition that the total mass transfer rates due to the two mechanism are equal, the mass transfer rate, dN/dt can be solved. The rate of change of the island radius is given by the mass transport rate together with the equation of $\rho_e(r)$ through $dn/dt = \rho_s dV_c(r)/dt$ with n mass of the material. A critical radius r_c is defined as the radius of those islands that are in equilibrium with ρ_0, $\rho_e(r_c) = \rho_0$. It is established such that islands having radii larger than r_c will slowly grow at the expense of islands having smaller radii than r_c. The universal form for

the rate of radius change was written as[31]:

$$\frac{dr}{dt} = -\frac{\beta}{r^m}(\frac{1}{r} - \frac{1}{r_c}), \tag{1.12}$$

where β is only a function of temperature and m is an integer number, 0, 1 or 2, depending on the mass transport process and dimensionality of the island growth.

The island size distribution, $f(r,t)$, can be derived through the conservation of mass. The equation of continuity gives:

$$\frac{\partial f(r,t)}{\partial t} = -\frac{\partial f(r,t)dr/dt}{\partial r}. \tag{1.13}$$

Assuming the invariance of the ratio r/r_c, the distribution function $f(r,t)$ can be separated to a time dependence function and a radial dependent function. An integration of Eqn.(1.13) using Eqn.(1.12) can solve for $r_c(t)$ with a given size distribution at $t = 0$, and the explicit time dependence of $r_c(t)$ is given as,[31]

$$r_c(r) = r_c(0)(1 + \frac{t}{\tau_c})^{\frac{1}{m+2}} \tag{1.14a}$$

$$\tau_c \propto r_c^{m+2}(0)/\beta, \tag{1.14b}$$

where the time constant τ_c depends on the value of m. This equation indicates that the critical size always follows a power law growth. The time dependence of the island number density can also be further derived as,

$$n = n(0)/(1 + \frac{t}{\tau_c})^{\frac{3}{m+2}}. \tag{1.15}$$

It can be concluded that both island number density and the single atom concentration decrease monotonically with time. The coarsening time constant is related to the initial island size distribution, temperature, the mass transport mechanism and whether the growth is 2D or 3D.

1.3 Quantum Size Effect

The physics of quantum size effects (QSE) in epitaxial metal films grown on semiconductors has received much interest over the past several years. Under certain growth condition,

metals deposited on semiconductors can give rise to confinement of the valence electron in the ultrathin film. The Pb/Si(111) system is one such interface exhibiting strong QSE. Due to the vertical confinement, the electronic energy states are quantized and lead to novel properties such as the thickness dependent stability of Pb film or islands. The growth of Pb on Si(111) has been studied with various surface science experimental techniques such as scanning tunnelling microscopy (STM) [4, 5], high-energy electron diffraction (RHEED) [1] and X-ray diffraction [6, 18, 19] etc. In this system, the Pb film has been found to follow a layer plus islands growth mode at low temperatures. In a typical temperature range of 150-250K, after the first Pb layer is completed (referred to as the wetting layer), Pb(111) islands start to form with uniform height, steep-edges and flat-tops on the surface[3, 4]. It has been shown that Pb islands have a very narrow height distribution and island heights differ by increment of two Pb layers under these growth conditions. The bilayer stability is partially understood in terms of energy oscillations of the total electron energy as quantum well states pass below the Fermi energy every two Pb layers[2, 12]. At even lower temperatures, the growth of Pb islands is suppressed due to the low adatom mobility[6]. In this low temperature regime the Pb film grows in a quasi layer-by-layer growth mode[13, 14]. The quasi layer by layer mode refers to the observation that the layer atom density varies up to about 6ML where a true layer-by-layer mode is established. Studies of films with different thickness (i.e. whether or not a film is stable with respect to the total energy landscape) have shown a thickness dependence of the film layer structure and its distortion relative to the bulk[14, 16]. This lattice distortion or strain has been related to the charge distortion due to electron confinement, which is also characteristic of QSE phenomena. In the following sections, a brief introduction of QSE is given.

1.3.1 Quantum Well States

Free-electrons confined in a one-dimensional infinite quantum square-well is the simplest way to represent an ultrathin metal film system. The potential $V(z)$ is zero inside the well ($0 \leq z \leq D$) and infinite elsewhere, where D is the width of the well. The width of the quantum well equals $D = Nd$, where d is the interlayer spacing and N is the integer number

of atomic layers in the film. The wave functions within the well are obtained by solving the Schrödinger equation with $V(z) = 0$ using the boundary conditions $\psi(0) = \psi(D) = 0$. The wave index for the allowed electronics states are:

$$k_n = \frac{\pi n}{D} \qquad n = 1, 2, 3 \ldots n_0 \tag{1.16}$$

with n_0 the total number of allowed states. Each of the allowed electronic states therefore has a wave functions in the form of:

$$\psi_k(x, y, z) = \sqrt{\frac{2}{V}} \sin(k_n z) e^{ik_x x + ik_y y}, \tag{1.17}$$

where V is the total volume. Within the Fermi sphere, the highest allowed electronics states has the quantum number $n_0 = int(\frac{k_F D}{\pi})$, where k_F is the Fermi wave vector. Therefore the total electronic energy of the film within a free-electron gas model can be written as [16]:

$$E = \frac{2V}{8\pi^3} \int_{|\vec{k}|<k_F} d^3\vec{k} \frac{\hbar^2 |\vec{k}|^2}{2m}, \tag{1.18}$$

$$= \frac{A\hbar^2}{8\pi m} \sum_{n=1}^{n_0} (k_F^4 - k_n^4), \tag{1.19}$$

where $A = V/D$ is the surface area of the film and m is the mass of the electron. When D increases, the number of allowed states decreases and the separation between them increases.

In reality, the quantum wells have a finite depth, where the potential is zero inside and V_0 elsewhere. The solutions of the Schrödinger equation for this boundary condition decay exponentially outside the well. The spillage of electronic charge density into the classical forbidden region can be described with a phase shift ϕ, which is related with the wave vector index number k_n,

$$2k_n D + \phi = 2\pi n \qquad n = 0, 1, 2 \ldots . \tag{1.20}$$

The phase shift is derived from the continuity conditions of both the wave functions Ψ and its derivative $\partial\Psi/\partial z$ at the boundary of the finite well [11]. Since $\phi = -\pi$ for infinite quantum well, the quantum number n starts from zero.

This simple square-well model does not take into account the effect of the crystal lattice and the band structure, which are important for understanding QSE in ultrathin metal

films. In a crystal electrons are no longer described by free electron plane waves, but Bloch waves. The potential in the horizontal xy-plane is periodic, while the potential in the z-direction is a square well. The wave functions within the well are therefore written as a product of two components, a Bloch wave function $\phi(x, y)$ and a free electron wave function $\psi_k(z)$ shown in Eqn.(1.17),

$$\Psi_k(x, y, z) = \phi(x, y)\psi_k(z). \tag{1.21}$$

As a result, the quantum well states have in-plane dispersion, giving rise to 2-dimensional energy subbands. As the well width D increases, the energy subbands pass below the Fermi level sequentially[12].

Thin metal films epitaxially grown on a semiconductor are bound by the vacuum on one side and the substrate on the other side, therefore the phase shift and potential barrier at each interfaces will be different. The total phase shift ϕ in Eqn.(1.20) is the sum of the phase shift at the metal-vacuum interface ϕ_v and that at the metal-semiconductor interface ϕ_s. On the vacuum side, the potential barrier is determined by the work function. At the metal-semiconductor interface, an electrons is confined to the film when its energy is within the band gap of the substrate.

1.3.2 QSE in physical properties

Early theoretical calculation on QSE properties of free standing waves in thin metal films were performed by F.K.Schulte [20]. His calculation were based on the density functional theory (DFT) developed by Lang and Kohn [21], showing that in a free-electron jellium model, electron densities, potentials and work functions all oscillate as a function of the film thickness with a period of half the Fermi wavelength without including band structure and crystal lattice. The free energy of the film has also been shown to have a thickness dependence. Experimentally, Pb grown on Si(111) showed oscillations in the films' electrical resistivity as a function of thickness. This was first experimentally observed during growth by electrical resistivity measurement and intensity oscillations in RHEED specular spots [22]. Oscillation due to layer-by-layer growth were modulated by an oscillation with a bigger period due to QSE. The period of the modulation was correlated with the discrepancy

between the lattice parameter and the half Fermi wavelength of Pb. For Pb(111) the lattice parameter $D = 2.86$Å and the Fermi wavelength $\lambda_F = 3.95$Å, which gives approximately $2D \approx \frac{\lambda_F}{2}$, indicate that every bilayer of Pb can approximately support three half Fermi wavelengths, therefore cause the observed bilayer oscillations.

A jellium model calculation also demonstrated that the total free energy of the film have a thickness dependence [20]. Quantum confinement and charge spillage at the interfaces are the two major effects that affect the free energy of the film and thus have a direct impact on the stability of the film. The thicknesses z are expected to be stable at local minimums of the total energy curve where $\partial E/\partial z = 0$ and $\partial^2 E/\partial z^2 > 0$. When the total free energy is at the local maximums of the free energy curve, it could be lowered by shifting its thickness to a larger or smaller value corresponding to stable thicknesses. Therefore the film are expected to grow with multiple-height of stable thickness, provided there is sufficient surface diffusion. The oscillatory behavior in the surface energy and work function of metal thin films have been confirmed by calculations beyond the free-electron jellium model, where the crystal band structure together with discrete values of film thickness were taken into account[23, 24].

First-principles calculations of both free-standing Pb films and Pb films on Si substrates were performed to study the oscillatory behavior of various physical properties due to QSE [12, 17]. For free-standing Pb films, energy levels of the QW states at $\bar{\Gamma}$ as a function of thickness were calculated using the local-density approximation. The energies of QW states were shown to cross the Fermi level for every increment in the film thickness of about 2.2 layers, and this 2.2-layer periodicity can also be obtained using the an energy dependent phase shift $\phi(\varepsilon)$ of the electronic wave function upon reflection at vacuum-metal interface, $\Delta N = \pi/k_F D$, where k_F is the Fermi wave vector measured from L. The phase shift at the metal-semiconductor interface would be different than that of the metal-vacuum interface, therefore the energies of the QW states would be changed for a given N, but the periodicity in thickness for the QW states would remain the same. The calculation for the Si-supported films were carried out by compressing the Si unit cell to match the Pb lattice constant. The relative surface energy $E_S(N)$ were calculated as a function of film thickness N for both

free-standing and Si-supported Pb films, shown in Fig. 1.3(a) and 1.3(b) respectively. The dotted curves are fits to the relative surface energy with a damped sinusoidal function,

$$E_s = \frac{A|sin(k_F dN + \phi)| + B}{N^\alpha} + C, \tag{1.22}$$

where A,B and C are thickness-dependent constant, ϕ is an interface-dependent phase shift and $\alpha \sim 2$ is a decay component. Both $E_S(N)$ curves exhibit oscillations with the same period as a result of quantum confinement. However, the change in boundary condition introduces a different phase shift, which makes the envelop function shift. The minimum at $N = 1$ in Fig. 1.3(b) corresponds to the formation of a one-layer wetting layer at the early stage of growth. Other local minima indicate their stability is favored by the energy landscape. Therefore Pb islands with uniform height are expected to form on Si(111), and increasing Pb coverage within a certain range will only lead to lateral growth of the islands.

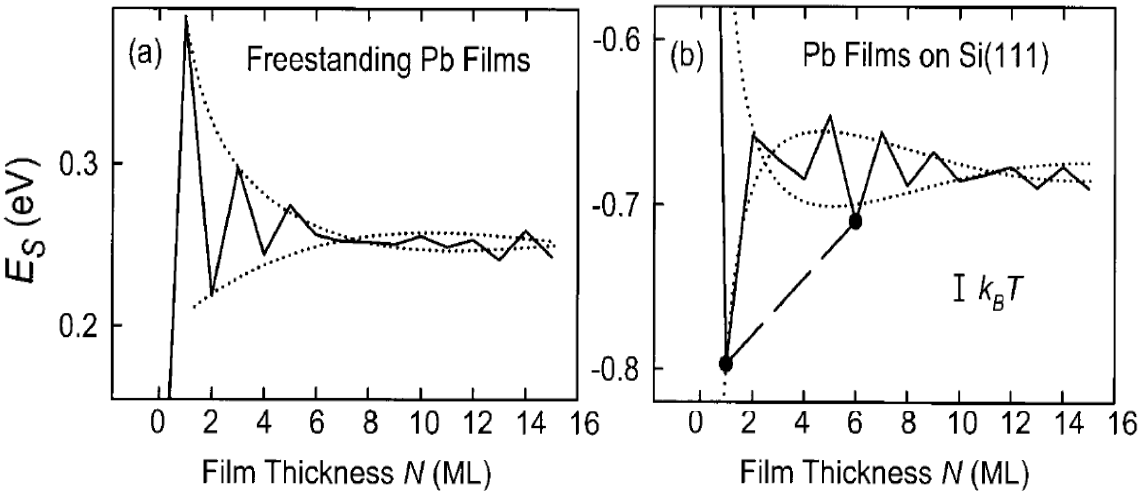

Figure 1.3: Calculated relative surface energy per surface atom as a function of layer thickness of an integer number N, for (a) freestanding Pb films; (b) Pb films on Si. The dotted curves represent envelope functions for the quantum oscillations. Figure from Hong *et al.*[17]

1.3.3 Preferred thickness and stability

The existence of preferred thicknesses have been reported by many experimentals for the Pb/Si(111) system. An STM image of Pb islands grown on Si(111) 7x7 substrate and its

height histogram are shown in Fig. 1.4 for illustration purposes. The histogram shows that the predominant island height is 7-layers. As STM experiments primarily probe the surface, islands height are measured with reference to the wetting layer. As will be shown later, the values of island heights is actually one layer larger as measured by x-ray diffraction. [40]

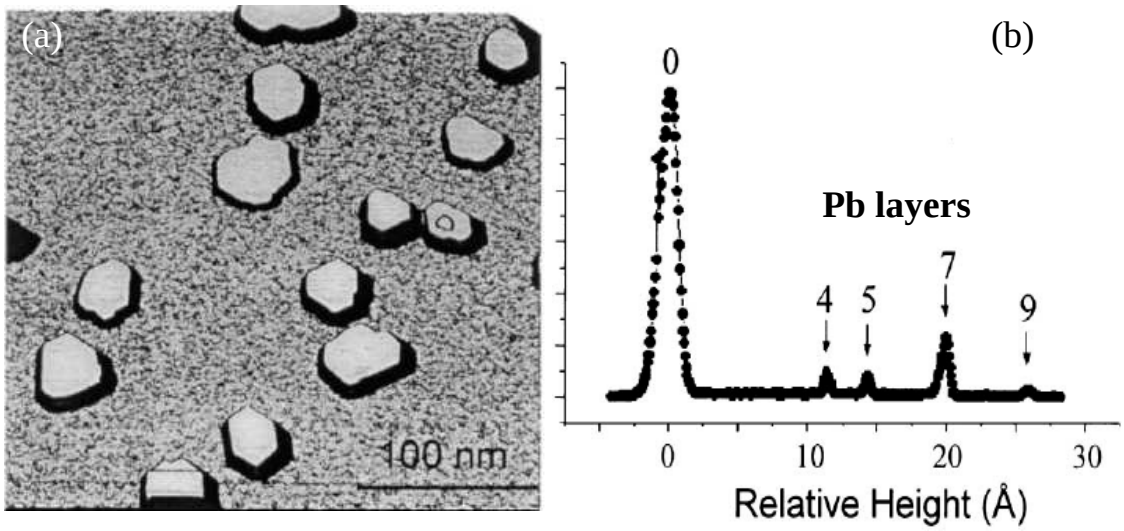

Figure 1.4: (a) A 300x300nm STM image of 3.2ML Pb deposited on the Si(111) 7x7, growing into flat-topped, steep-edge islands; (b) the island height histogram with preferred heights at 4, 5 and 7 monolayers of Pb. Figure from Su *et al.*[27]

The preferred island heights depend on both the Si substrate surface and the growth conditions. It has been shown that the Schottky barrier height (SBH) of the Pb/Si(111) interfaces affects the stability of the islands.[2]. The two atomic reconstructions of the substrate interface, Si(111) 7x7 and Si(111)$\sqrt{3} \times \sqrt{3}$-Pb, have different SBHs which are 0.70 eV and 0.95 eV, respectively[39]. The resulting preferred island heights from the two types of substrate interfaces are 7-layer to 5-layer, respectively[4]. The dependence of island heights on various growth conditions such as temperature, coverage and annealing process has been studied using STM combined with SPA-LEED[4]. The results were summarized in a kinetic phase diagram shown in Fig. 1.5. This phase diagram shows the type of islands that can form in the coverage-temperature plane. The heights marked in different regions are the most abundant heights. At a fixed coverage, the dominant island height increases in bilayer increments as temperature is increased. The bilayer stability further proves that

QSE is the driving force of the preferred island heights.

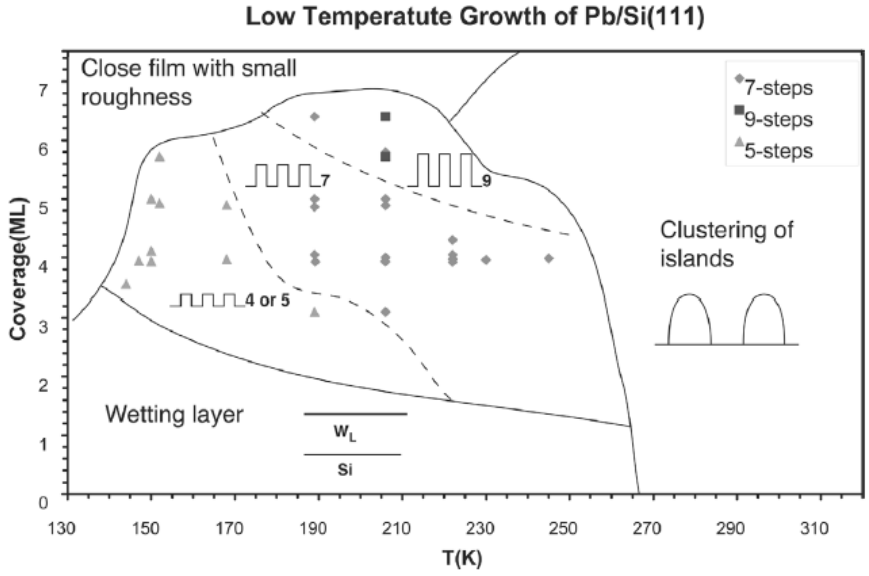

Figure 1.5: A kinetic Phase diagram for Pb grown on Si(111) 7x7 for coverage up to 10ML in a temperature range of 120-250K. Preferred island height will increase with bi-layer increment as the coverage or temperature are increased. Figure from Hupalo *et al.*[4]

While QSE is thought to play a role in Pb islands growth on Si(111), predicting QSE energies remains problematic. Two important parameters, the island height and the metal semiconductor interface structure, must be known before quantitative predictions can be made. The island height determines the quantum well depth while the interface structure determines charge transfer into the islands. The latter effect controls the Fermi level and thus is important in determining the total energy of a Pb island. While it is evident that the observed island heights are related to the electron confinement in the island vertical dimension, a detail understanding explaining why the islands form in the first place and why QSE is so strong in this system still remains. Furthermore, the arguments given above for QSE effects in the Pb/Si(111) system are based on energy minimization that are essentially thermodynamic arguments. The Pb islands are known to irreversibly transform to 3D clusters near room temperature. The question is therefore raised, what kinetic mechanisms allow islands to grow to stable heights where they subsequently increase their radius instead of continuing to grow to higher heights? It is this question and the structure of the Pb/Si(111) interface that are the subjects of this research.

CHAPTER II

SURFACE X-RAY DIFFRACTION EXPERIMENTS

2.1 Introduction

Surface diffraction is one of the most commonly used techniques to determine the atomic structure of surfaces. In the case of X-rays, both the theory and applications have been described in many books and reviews[46, 48, 47, 49]. Unlike electrons, X-rays weakly interact with the electron density which allows them to penetrate through very thick films and allows simple single scattering theories to be used in data analysis. By the same token, their surface sensitivity is low. To compensate for low scattered intensity from surfaces, x-ray sources for surface scattering must be intense. Synchrotron X-ray sources have the advantages of not only high fluxes but high q-resolution, and a high degree of coherence. The cost and complexity of the intense X-ray sources have been balanced by the simplicity in data analysis since it is a weakly-interacting probe. The characteristic X-ray wavelength is in the order of an angstrom, $\lambda = f(E)$, which corresponds to the typical interatomic spacing in a solid. Therefore the X-rays diffracted from a solid with periodic arrays of atoms, reveal the positions of the atoms within the crystal structure. While real space imaging methods such as scanning tunnelling microscopy (STM) measure the atom positions through the electron distribution near the Fermi energy, surface X-ray diffraction measures the Fourier transform of the inter-atom correlation function. This technique can be used for different purposes to obtain a variety of information about the properties of the surface.

This chapter starts with a brief introduction to the crystal lattices, mainly the face-centered cubic(*fcc*) and diamond structures due to their relevance to this work. Surface reconstruction of the substrate plays an important role in kinetics studies, and therefore is discussed. The basic kinematic theory of X-ray diffraction is then introduced, and reciprocal lattice will also be presented and related to the real-space crystal lattice as an important concept in description of diffraction phenomena. The diffracted intensity from a crystalline

sample is derived and formulated quantitatively. An overview of experimental methods used in this research work will then be introduced, including the synchrotron radiation source, ultrahigh vacuum chamber, surface diffractometer and sample preparation. Finally, the transverse rod scan and specular reflectivity measured for the Pb/Si(111) systems will be discussed. Specific formulas are derived to fit the experimental data.

2.2 Crystal Lattice

Most solids have periodic arrays of atoms that form a crystal lattices. Crystalline solids are composed of orderly arrangements of atoms, ions, or molecules through the repetition of some identically configured unit cells. The unit cell by definition is a volume of space that can fill up the entire crystal space without intervening. The type of unit cell with a single lattice point is called a primitive unit cell. Each lattice point in a crystal can be $\vec{r} = n_1\vec{a}_1 + n_2\vec{a}_2 + n_3\vec{a}_3$, where $\vec{a}_1$, $\vec{a}_2$ and $\vec{a}_3$ are primitive vectors.

In general, crystalline solids have rigid shapes with clearly defined faces. Particular attention will be paid to the face-centered cubic (*fcc*) and diamond lattice structures, which are the structures of Pb and Si, respectively. Figure 2.1(a) shows a cubic unit cell of a *fcc* lattice, where there are atoms positioned at each corners and in the center of each face of the cube. The *fcc* lattice is a closed packed structure on a cubic array because spheres of equal size occupy the maximum amount of space. A primitive unit cell can be chosen to describe the *fcc* lattice, which is rhombohedron and includes only one atom, shown as the shaded region in Fig. 2.1(a). Other unit cells with more symmetry can always be chosen if their shape is more convenient to work with.

Si shares the same structure with diamond that can be represented as the *fcc* lattice with a two-point basis. The basis consists of one point at the origin $\vec{0}$ and the other located along the body diagonal of the cubic cell by one quarter the length of the diagonal $\vec{R} = \frac{a}{4}(\vec{x}+\vec{y}+\vec{z})$, where the lattice constant a is the length of one edge of the cubic unit cell. As shown in Fig. 2.1(b), the additional sites other than the normal *fcc* sites are shown in open circles within the cubic cell. Each white circles locates relative to one of the *fcc* sites by the vector $\vec{R}$, therefore the diamond structure can also be viewed as two interpenetrating *fcc*

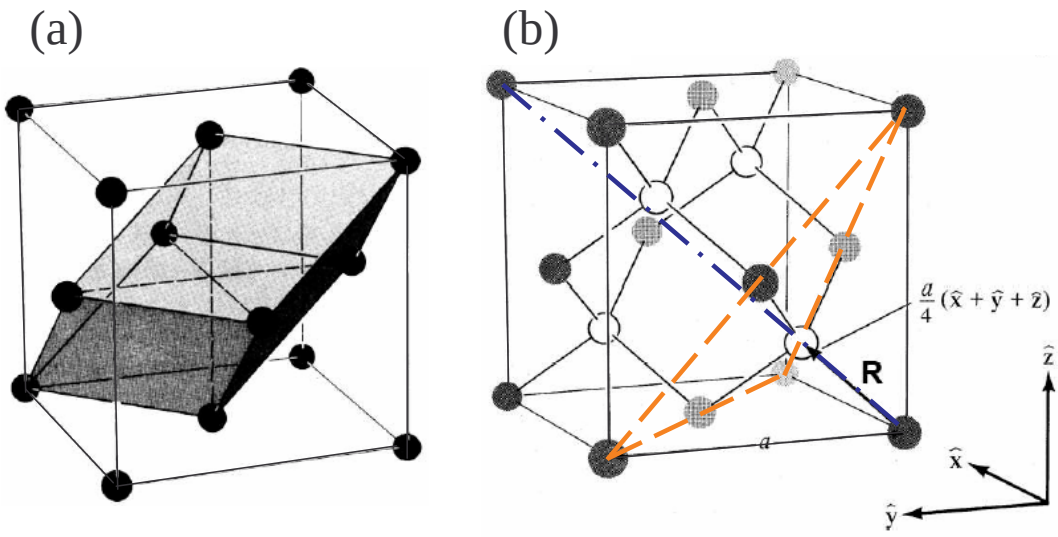

Figure 2.1: (a) Cubic unit cell of the *fcc* lattice. The primitive unit cell is shown as the shaded region which contains one atom. (b) Cubic unit cell of the diamond lattice, which is the *fcc* lattice with a two-point basis. The additional atoms to the normal *fcc* sites are shown in open circles. Nearest neighbor bonds have been drawn in solid lines. The (111) direction is shown in a blue dot-dashed line while the plane outlined with red dashed lines is the (111) atomic plane. Figures from Ashcroft *et al.*[49]

lattice displaced by $\vec{R}$ to each other. Nearest-neighbor bonds are drawn as solid lines in the diagram, which indicates that the four nearest neighbors of each point are positioned at the vertices of a regular tetrahedron. In this work, the substrates were commercial single crystal Si(111) wafers. The notation of Si(111) refers to the crystal facet of the wafer surface, which is the (111) crystal plane. An atomic plane in a crystal is denoted by the vector normal to the plane. In this case, the indices are based on cubic coordinates. Therefore the [111] direction is along the body diagonal of the cubic unit cell and normal to the (111) plane, as shown in Fig. 2.1(b). The atoms on (111) planes in a *fcc* lattice are located on hexagonal nets[50]. The crystal axes in the (111) plane are along the diagonal of two perpendicular cubic faces of the cubic unit cell, while the third axes is along the body diagonal. One choice of the primitive vectors are:

$$\mathbf{a} = \frac{a}{2}(\vec{x} - \vec{z}); \mathbf{b} = \frac{a}{2}(\vec{y} - \vec{z}); \mathbf{c} = \frac{a}{2}(\vec{x} + \vec{y} + \vec{z}), . \tag{2.1}$$

which gives the area of the surface unit cell $A = \frac{\sqrt{3}}{4}a^2$. For the Pb/Si(111) system, it is more convenient to work with hexagonal coordinates since one of the crystal axe coincides

with the surface normal.

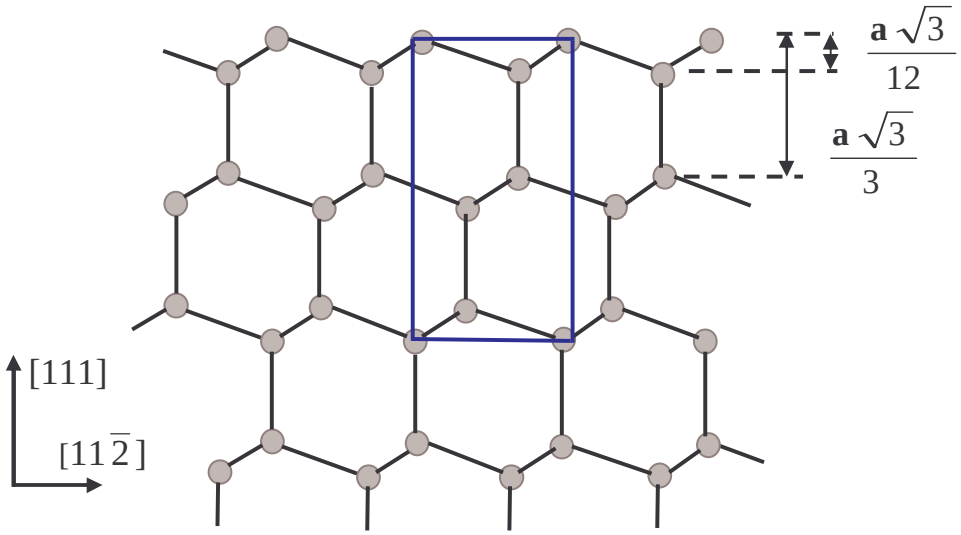

Figure 2.2: Side view of Si(111) atomic layer structure with interlayer spacings shown. A unit cell is marked in a blue frame, which indicates totally six atoms per unit cell. The surface termination is between double layers that has less number of dangling bonds.

The Pb films grown on these Si(111) substrates through thermal evaporation is oriented along the [111] direction as well. Since there are three (111) atomic planes within one cubic unit cell, the interlayer spacing of Pb atomic layers is one third of the body diagonal length of the cube $\frac{a\sqrt{3}}{3}$. In the case of Si, the two *fcc* sites in the diamond structure are displaced from each other by $\frac{a}{4}(\vec{x}+\vec{y}+\vec{z})$, which is equivalent to a distance of $\frac{a\sqrt{3}}{4}$ in the [111] direction. As a result, there is an additional plane above each *fcc* (111) atomic plane with a length of $a\frac{\sqrt{3}}{4}$, which is below the next atomic plane with a length of $a\frac{\sqrt{3}}{12}$. Therefore the lattice of Si(111) has a bilayer structure in hexagonal coordinate systems, in which one unit cell contains six atoms, as shown in Fig. 2.2. The termination, planer truncation of the bulk, of Si(111) surface was believed to be between the bilayers because it has three times less number of dangling bonds than the termination in the middle of the bilayers[7].

2.3 Surface Reconstruction

The structure of a crystal surface can be quite different from its bulk structure. Truncation of the bulk crystal to form a surface results in dangling bonds. The surface atoms can

shift from their bulk positions to remove the excess energy associated with the dangling bonds and therefore minimize the surface energy. This kind of rearrangement is called a *surface reconstruction*. Reconstruction can also be caused by different kinds of atoms being absorbed on the surface.

There could be more than one type of reconstruction for a surface depending on the formation conditions. The studies of Pb/Si(111) system mainly work with 7×7 or $\sqrt{3} \times \sqrt{3}$ reconstructions of the Si substrate. The 7×7 reconstruction can be obtained by flashing the substrate to about 1250°C and annealing afterwards. Its structure was determined to be the dimer-adatom-stacking fault (DAS) model[7, 10]. In this model, there are 12 top layer adatoms, 42 two atoms in the second layer and 48 atoms in the third layer. A triangle halve of the 7×7 unit has a border formed with nine dimers in the third layer, and one of the triangle halve of the unit has a stalking fault in the second layer. The surface structure of the 7×7 reconstruction is shown in Fig. 2.3.

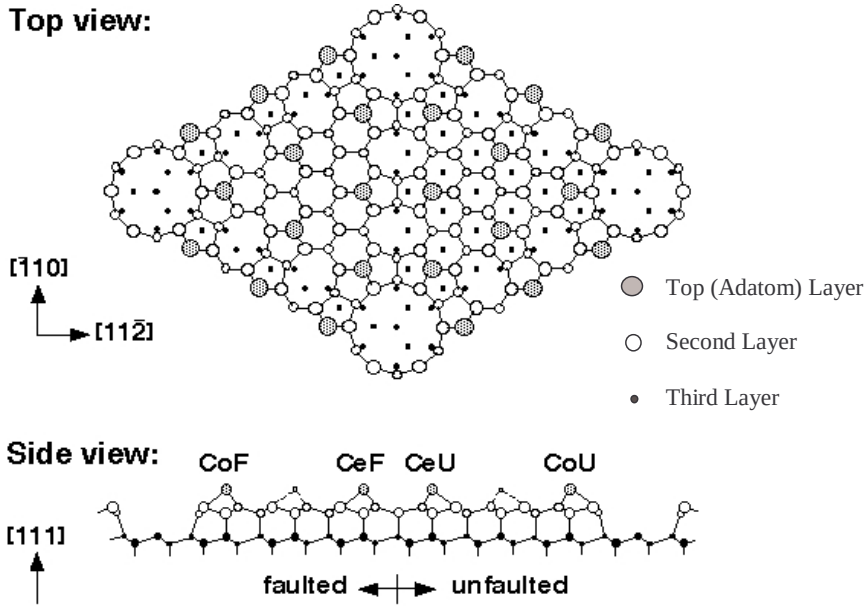

Figure 2.3: The surface structure of Si(111) 7×7 reconstruction.(a) Top view of the first three layers. (b) Side view of the structure that indicating the faulted and unfaulted halve of the 7x7 unit cell. Figure from Takanagi *et al.* [10]

The Pb/Si(111) $\sqrt{3} \times \sqrt{3}$ reconstructed interface has been used to grow smooth Pb films at low temperatures. After $\sim$ 1.1ML Pb deposited on Si(111)7×7, heat treatment

applied up to $\sim 400^{\circ}$ and annealing afterwards will result in $\sqrt{3}\times\sqrt{3}$ reconstruction[16]. At temperatures below $\sim$ 150K, the resulted bulk-like termination of Si(111) allows Pb films to grow layer by layer on the substrate.

2.4 Experimental Methods

The experimental instruments and methods are reviewed in this section. In this work, all experiments were performed using the intense monochromatic X-rays from a synchrotron source. The source will, therefor, be briefly reviewed. The experimental equipments involves a six-circle diffractometer, an ultrahigh vacuum (UHV) chamber and other surface analysis tools that will be discussed below.

2.4.1 Synchrotron X-ray Source at the APS

The studies using X-rays, a weak interacting probe, requires high-intensity monochromatic beam that is provided by the a synchrotron radiation source at the Advanced Photon Source (APS) at the Argonne National Laboratory. At the APS, positrons are accelerated to 7 GeV and injected into a 1104-meters-circumference storage ring, where the focused positrons beam is travelling at nearly the speed of light. Since the synchrotron storage ring is optimized for insertion devices, APS is referred as a "third-generation" light sources.

Predicted by the the special theory of relativity, synchrotron radiation is generated when charged particles are accelerated centripetally at a speed close to the speed of light c[52]. To force the high energy positrons into a circle, a series of bending magnets is used. At each of these magnets synchrotron radiation is produced. To achieve a much more intense X-ray source, the radiation source can be constructed by putting in insertion devices that consists of a series of periodic dipole magnets, equally spaced by a length λ and oriented in opposite directions. The static magnetic field is alternating along the length of the device, as shown in Fig. 2.4. Positrons travelling in this periodic magnetic field undergo oscillations and radiate. The dimensionless parameter $K = eB\lambda/2\pi mc$, with e the electron charge, B the magnetic field and m the positrons mass, characterizes the nature of the radiation. For $K << 1$, the radiation emitted from the positrons in each oscillation on its trajectory is in phase with the radiation from other oscillations. As a result, the total amplitude of the

radiated photons resides within a narrow band of energy, thus the radiation is coherent and the insert device is called an undulator. For $K >> 1$, the in-phase condition is not valid any more, the radiation is incoherent and the insert device is called a wriggler. At Sector 6ID-C of APS, where the experiments have been performed, an undulator has been used to provide high brilliance X-ray in the 3-40 keV energy range. In addition, the angular divergence of the x-ray beam is nearly 10^4 smaller than the beam produced at the bending magnets.

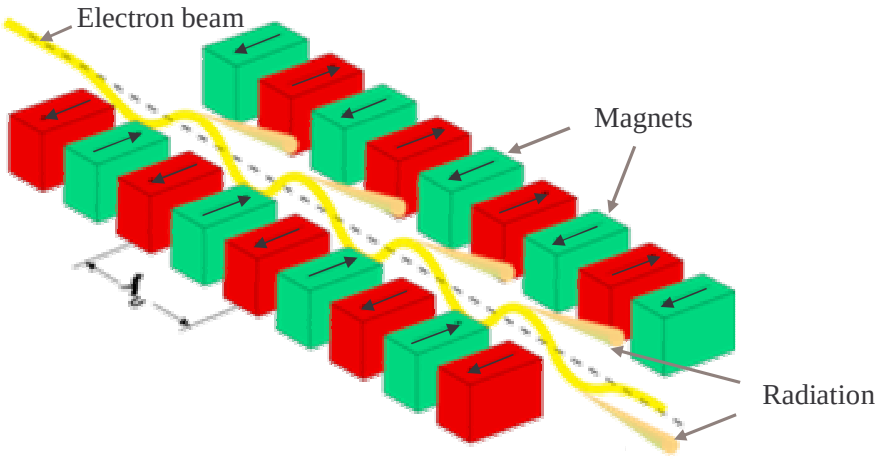

Figure 2.4: A schematic draw of the structure of an insert device (wriggler or undulator). Magnets of alternating polarities, are separated with distance λ.

Though the undulator radiation has a narrow band of energy, the X-ray beam energy is further selected using a double crystal Si(111) monochrometer. The incident angle of the beam to the first crystal is chosen to be the Bragg angle for the desired wavelength, which yields a sharp Bragg peak. Only X-rays of the corresponding wavelength will be diffracted from the crystal, the outgoing X-ray beam is therefore monochromatic. The crystal is cooled with liquid nitrogen for heat dissipation. The monochromatic beam then passes through a second crystal, which is set to the same Bragg angle but translated so that the outgoing beam maintains its initial direction for any energy selected.

2.4.2 Surface Diffractometer

All experiments in this work were performed in the surface X-ray diffraction station at Sector 6ID-C, operated by μ-CAT (Midwest University Collaborative Access Team). The

instrument consists of a six-circle diffractometer integrated with a UHV chamber and other surface analysis tools such as low energy electron diffraction (LEED) and Auger spectroscopy etc. Figure 2.5 shows the equipment with some of its major components marked. The highly focused intense X-ray beams enter the station through tubes filled with helium gas to reduce air scattering. A detector placed next to the exit of the tube uses parasitic air scattering to monitor beam intensity fluctuations due to accelerator current drifts or mechanical drifts in the x-ray optics. This monitor is used to normalized the scattered x-rays from the sample. X-ray beam size is adjusted by a pair of slits and usually chosen to be 0.2mm in the vertical directions by 0.5mm in the horizontal direction.

The incident and diffracted X-ray beams pass through and exit the UHV chamber through a beryllium window (a low Z scatter material). The large Be window yields a large angular range and thus a large portion of reciprocal space is made accessible. The sample and its holder are fixed on an internal rotatable χ arc with 100° rotation range. Thus the experimental sample geometry can be both vertical and horizontal. In this nomenclature we define the horizontal geometry to mean the sample normal is in the plane of the accelerator. LEED is normally used to observe the reconstruction structure of the initial surface during sample preparation. A displex coupled with a helium compressor is connected to cool the substrate below $\sim 60K$. There are two evaporators connected to the UHV chamber, one of which is an electron-beam evaporator for producing a flux of Pb atoms. Evaporation flux rates are calibrated using a method described in Section 2.4.4. A load-lock chamber is attached to the main chamber so that samples can be replaced without breaking the main chamber vacuum.

Figure 2.6 show a schematic drawing of the diffractometer where the azimuthal ϕ axis is not used. Thus the diffractometer has five degrees of freedom: the horizontal ν and perpendicular δ rotations of the detector, the horizontal μ and perpendicular η rotations of the sample, and the tilt motion χ of the sample. As mentioned the χ rotation allows the scattering geometry to be either horizontal or vertical. The horizontal geometry has been used to collect all transverse scans and reflectivity data. In this geometry the sample is mounted with its normal parallel to the beam polarization direction, as shown in Fig. 2.6.

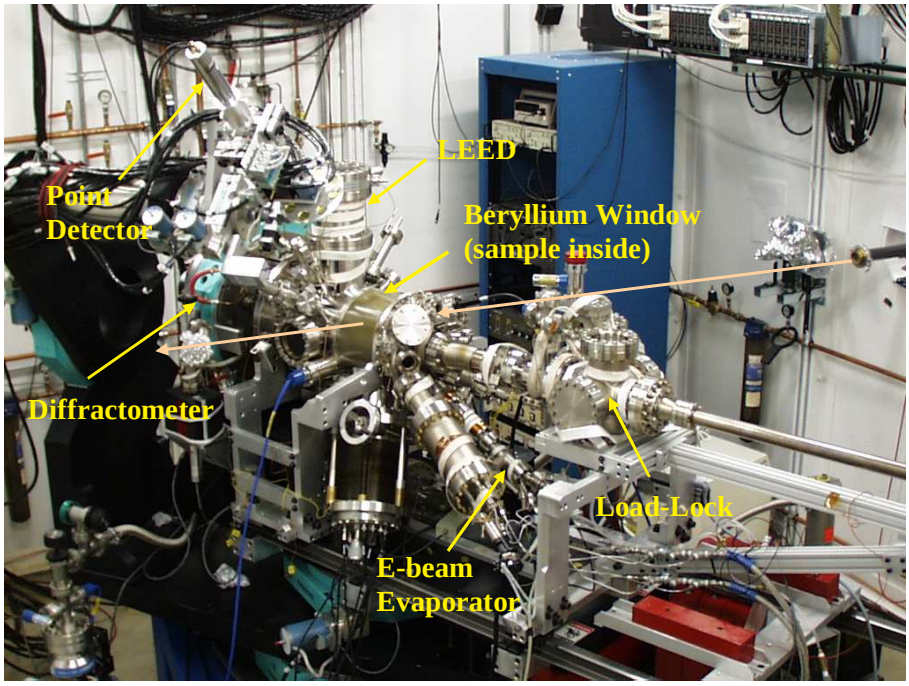

Figure 2.5: The surface diffractometer and UHV chamber in Station 6ID-C, μCAT. Major components are marked.

Therefore it has the advantage of not involving a beam polarization factor in calculating intensities. In addition, it allows the sample to directly face the e-beam evaporator, which ensures convenient and uniform deposition in the scattering geometry. In the horizontal geometry, both μ axis and δ axis move in a horizontal plane and determines the beam incident angle θ_i and outgoing angle θ_f, respectively. The diffractometer is moved with stepper motors having an angular resolution of 5 thousandth of degrees. The sample is positioned at the center of rotation of all axes.

Both point detector and charge-coupled device(CCD) detector have been used to collect X-ray diffraction data. The high-resolution Bicron point detector is mounted on the detector arm approximately 1000mm from the center of rotation, with angular resolution controlled by a pair of adjustable slits in front of it. Since background radiations can be easily blocked out with the slits, point detectors have the advantage of providing high resolution data with low background counts. However, measurements done using point detectors are time-consuming because a scan across a rod must count one point at a time (motor moving time

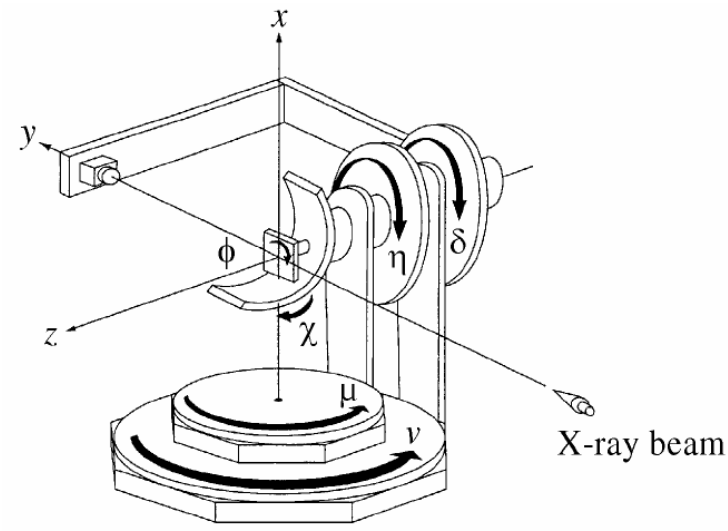

Figure 2.6: A schematic drawing of the '4S+2D' diffractometer.[33] The ϕ axis is actually fixed in the experiments. The sense of rotations, laboratory frame, and the incoming X-ray directions are shown as arrows.

are a significant fraction of counting time). For kinetics studies of thin film growth and coarsening where the characteristic kinetic time is of the order of 10 seconds, a CCD was used that is capable of collect the X-ray scattering data over a large region simultaneously (the minimum collection time is set by the CCD to computer dump time of 5sec). Once the sample has been lined up at a Pb Bragg reflection using the point detector, the CCD detector is substituted in the same position, with the detecting plate perpendicular to the beam. The data collected by the CCD detector represent a reciprocal space mapping of the surface. The geometry of the transverse rod scan in this work will be discussed in Section 2.6.1.

2.4.3 UHV Technology

The utility of the UHV chamber arises from the need of a clean surface for research purposes. Since a surface is always subject to contamination due to absorption of gas atoms, a vacuum environment can ensure a surface being kept clean for a certain amount of time so that studies of surface properties can be carried out. For instance, the time to form a monolayer gas atoms is in the scale of one second when pressure is 10^{-8}torr, but it is as long as 10^4seconds when the pressure is below 10^{-10}torr. Special operation procedures and

equipments are required to achieve ultra-high vacuum from atmospheric pressure. First of all, all instruments in the chamber including the substrate are required to be extremely grease-free. In addition to clean all parts with organic solvents, it is suitable to use materials with a low vapor pressure for parts in the chamber. For instance, flanges are attached with the chamber using copper gaskets instead of plastic o-rings. Secondly, because baking out is an important step to outgas the absorbed gases from the interior surfaces so that the system pressure can reach $\sim 10^{-10}$torr, the material used for the chamber and its inside parts are required to withhold temperature up to 150°C for ∼72hours. The UHV chamber is equipped with an ion pump, a titanium sublimation pump and a mechanical pump with a turbo. The mechanical pump together with a turbo pump is usually used to bring the chamber pressure down to the order of 10^{-7}torr and to pump the load lock.

2.4.4 Sample Preparation

The $8mm \times 10mm$ substrates were cut from commercial Si(111) wafers, cleaned in an ultrasonic with acetone and ethonone solvent. The sample was then mounted on a molybdenum holder and transferred into the UHV chamber. The holder has a hole slightly smaller than the sample size. This allows efficient electron bombardment heating of the sample from a tungsten filament placed right below the hole. The sample temperature is monitored by two thermocouples attached to the holder. An optical pyrometer is used to monitor the temperature when heating the sample above 700°C. Low temperature calibration of the thermocouple was made against a Ge diode mounted on a test sample in the holder.

After outgassing for hours at $\sim$ 700°C, the sample was flashed to $\sim$ 1250°C and annealing slowly back to room temperature. The heat treatment removed the oxide layer and formed 7×7 surface reconstruction, which can be observed using the LEED. This process was repeated several times to obtain a high quality Si(111) 7×7 reconstruction structure. The reconstruction could be recovered after removing deposited Pb when the sample was heated to 900°C.

Molecular beam epitaxy (MBE) method is used for depositing Pb atoms on the Si substrate. Since the melting temperature of Pb is lower than its evaporation temperature,

an electron-beam evaporator is used to produce the Pb atom gas. High purity Pb source was put in a molybdenum crucible with the crucible heated to high temperature through electron bombardment. The evaporation rate is proportional to the emission current between the filament and the crucible, which is regulated through a feedback circuit. To ensure high quality Pb atoms gas beam, the crucible and Pb source need to outgas at fairly high temperatures to remove impurities. The thermal isolation of the crucible is maintained through water-cooling. The Pb deposition is controlled by a shutter at the end of the crucible. The distance between the exit of the crucible and the substrate is about 200mm, providing a sufficient beam solid angle which allows the Pb atoms distributed uniformly across the sample.

The deposition flux rate is calibrated by monitoring the X-ray intensity oscillations at the anti-Bragg reflection of Pb film during deposition at very low temperatures, where the Pb growth follows the layer-by-layer mode. Layer-by-layer growth of a strong X-ray scatterer on a relative weakly scattering substrate results in parabolic cusps, the sequence of these cusps showing up allows us to determine the coverage. Figure 2.7 shows a typical X-ray diffraction growth oscillation. The scattering geometry was fixed at anti-Bragg diffraction ($l = 1.64$), and the scattering intensity measured as a function of time while Pb atoms were put on the substrate. The first peak should occur when the first Pb layer is complete. Since the second layer is out-of-phase with the first one, there should be a destructive interference when the second layer is complete. This process continues with successive layers so that peaks indicate odd-number layers and minima indicate even-number layers. However, as shown in Fig. 2.7, the peaks are not regularly spaced for low coverage, showing a disordering in the early stage of growth. Beyond approximately 6 oscillations, the period becomes regular, therefore the flux rate can be calibrated by the equally spaced oscillation at high coverages.

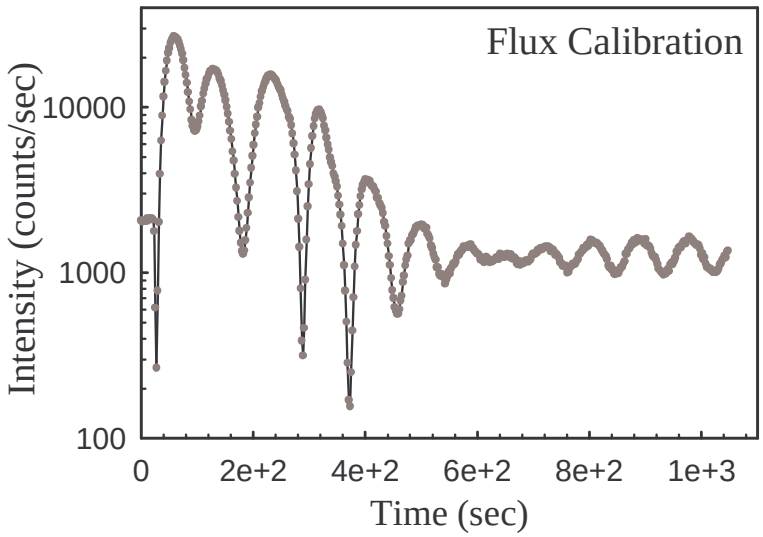

Figure 2.7: X-ray reflectivity growth oscillation measured at anti-Bragg position ($l = 1.64$). The irregular period of the oscillations at low coverages is due to disordering in the early growth. Beyond ~ 6 oscillations, the period becomes regular and has been used to calibrate the deposition flux.

2.5 Kinematic Theory

2.5.1 X-ray Diffraction by a Crystal

The X-ray diffraction technique has been widely used since the characteristic X-rays wavelength is on the order of interatomic distances in a solid. X-rays are essentially electromagnetic waves which can be represented as $e^{i\mathbf{k}\cdot\mathbf{r}}$ with wave vector $\mathbf{k}$;$|\mathbf{k}| = \frac{2\pi}{\lambda}$. When a plane wave with a wave vector $\mathbf{k}_i$ is incident on an atom and elastically scattered, the outgoing wave will have a wave vector $\mathbf{k}_f$, which has the same magnitude of $\mathbf{k}_i$ but usually with a phase shift. As the scattering cross section of an electron is approximately 10^6 times greater than a proton, the incident wave mainly interacts with the bound electrons of the atom[47]. For an electrons at positions $\mathbf{r}$ from the origin, the outgoing wavefunction can be written as:

$$\Psi = \frac{f}{D} e^{i(\mathbf{k}_f - \mathbf{k}_i)\cdot\mathbf{r}}, \tag{2.2}$$

where f is the atomic form factor and D is the distance from the detector to the electron. The form factor can be calculated from the atomic potential of an atom, assuming the single scattering limit. Moreover, if the outgoing wavefunction is assumed to be also a plane wave,

the form factor is only related to the momentum transfer vector[51], which is defined as:

$$\mathbf{q} = \mathbf{k}_f - \mathbf{k}_i, |\mathbf{q}| = |\mathbf{k}| \sin[(2\theta)/2]. \tag{2.3}$$

Here the 2θ is the scattering angle, as shown in Fig. 2.8 The exponential term in Eqn.(2.2) represents the phase factor. The phase is related to the atom position, which is arbitrary for one single atom involved in the diffraction. For X-ray scattering from a crystal, the phase is related to the interatomic distances.

The reflected waves from different atoms travel different lengths in the crystal and interfere with each other. The total reflected amplitude is the coherent sum of scattering from all atoms in the system,

$$A = A_0 \sum_j f_j(\mathbf{q}) e^{i\mathbf{q}\cdot\mathbf{r}_j}, \tag{2.4}$$

where A_0 is the amplitude of the incident beam. The difference of the travelling lengths need to be integer multiples of the X-ray wavelength for constructive interference to occur. In a crystalline lattice, the position vector $\mathbf{r}_j$ can be described by the position of the mth basis atom in the nth unit cell. This allows the scatting amplitude to be a product of sums over basis atoms and all cells,

$$A = A_0[\sum_{m\in cell} f_m(\mathbf{q}) e^{i\mathbf{q}\cdot\mathbf{u}_m}] \sum_n e^{i\mathbf{q}\cdot\mathbf{R}_n}, \tag{2.5}$$

in which $\mathbf{u}_m = u_a\mathbf{a} + u_b\mathbf{b} + u_c\mathbf{c}$ is each basis atom position in the unit cell relative to the cell origin, and $\mathbf{R}_n = h\mathbf{a} + k\mathbf{b} + l\mathbf{c}$ is the position of the unit cell from some arbitrary origin with integer indices h, k and l. The term in brackets is knows as the *crystal structure factor*, $F(\mathbf{q})$, the scattering amplitude from all atoms within the unit cell. The scattering intensity that is defined as the photon flux per unit solid angle is therefore given as:

$$I(\mathbf{q}) = AA^* = I_0|F(\mathbf{q})|^2 \sum_{i,j} e^{i\mathbf{q}\cdot(\mathbf{R}_i - \mathbf{R}_j)}, \tag{2.6}$$

where I_0 is the incident beam flux. The last term in Eqn.(2.6) represents the interference due to the organized arrangement of all unit cells. Suppose a 3D crystal contains N_a, N_b and N_c unit cells along the three directions in space, this interference term can be simplified

using the equation $\sum_{n=0}^{N-1} x^n = \frac{1-x^n}{1-x}$,

$$\sum_{i,j} e^{i\mathbf{q}\cdot(\mathbf{R}_i-\mathbf{R}_j)} = \frac{\sin^2(\frac{1}{2}N_a\mathbf{q}\cdot\mathbf{a})}{\sin^2(\frac{1}{2}\mathbf{q}\cdot\mathbf{a})}\frac{\sin^2(\frac{1}{2}N_b\mathbf{q}\cdot\mathbf{b})}{\sin^2(\frac{1}{2}\mathbf{q}\cdot\mathbf{b})}\frac{\sin^2(\frac{1}{2}N_c\mathbf{q}\cdot\mathbf{c})}{\sin^2(\frac{1}{2}\mathbf{q}\cdot\mathbf{c})}. \tag{2.7}$$

The interference function that consists of $\sin^2$ terms, have large peaks when $\mathbf{q}\cdot\mathbf{a}$, $\mathbf{q}\cdot\mathbf{b}$ and $\mathbf{q}\cdot\mathbf{c}$ are integer multiple of 2π. The peak intensity of each function is proportional to N_j^2 and width proportional to $1/N_j$. In addition, there are $N_j - 2$ interference fringes between two large peaks. In the limit of an infinite crystal, $N_a, N_b, N_c \to \infty$, these interference functions reduce to a series of Dirac Delta functions, which gives the intensity,

$$I(\mathbf{q}) = I_0|F(\mathbf{q})|^2\delta(\mathbf{q}\cdot\mathbf{a} - 2\pi h)\delta(\mathbf{q}\cdot\mathbf{b} - 2\pi k)\delta(\mathbf{q}\cdot\mathbf{c} - 2\pi l). \tag{2.8}$$

Therefore the intensity $I(\mathbf{q})$ is zero except when the constructive interference conditions are satisfied simultaneously,

$$\mathbf{q}\cdot\mathbf{a} = 2\pi h, \mathbf{q}\cdot\mathbf{b} = 2\pi k, \mathbf{q}\cdot\mathbf{c} = 2\pi l, \tag{2.9}$$

The above conditions to obtain a measurable diffracted intensity is known as *3D Laue Conditions*. The Laue conditions can therefore be interpreted as that the significant scattered intensity only occurs when the momentum transfer equal a reciprocal lattice vector, $\mathbf{q} = G = h\mathbf{a}^* + k\mathbf{b}^* + l\mathbf{c}^*$. The points in a 3D reciprocal lattice are called *Bragg points* because each of them corresponds to a momentum transfer vector $\mathbf{q}$ satisfying the *Bragg condition* $2dsin\theta = n\lambda$, were d is the distance between planes with normals in the G direction. The magnitude of the peak intensity at Bragg points depends on the crystal structure factor $|F(\mathbf{q})|^2$. Due to the modulation of the structure factor, the diffraction from some Bragg points may not be allowed and are the so-called *forbidden* reflections. In addition to the crystal structure, there are some experimental and geometric corrections that need to be taken into account in Eqn.(2.8). These include, beam polarization, sample size, detector acceptance angle, etc. and are listed in Appendix 1.

2.5.2 X-ray Diffraction by a Surface

Since a surface is regarded as truncated from a bulk crystal lattice and usually terminated with a specific reconstruction structure, the X-ray diffraction by a surface is approached

differently from that of a 3D crystal. The approximations of infinite crystal scale can only be applied to two of the three axes. When the basis vector **a** and **b** lie in the plane of the surface and **c** is along the surface normal, $N_a, N_b \rightarrow \infty$ while the number of atomic layers within the scattering surface N_c is finite. Thus the total scattered intensity is slightly deviated from Eqn.(2.8), assuming an attenuation coefficient per layer given by $\alpha = A_{n=1}/A_n \approx 1$ for X-rays penetrating the surface,

$$I(\mathbf{q}) = I_0|F(\mathbf{q})|^2\delta(\mathbf{q}\cdot\mathbf{a} - 2\pi h)\delta(\mathbf{q}\cdot\mathbf{b} - 2\pi k)\frac{1-\cos(N_c q_z c)}{1-\cos(q_z c)}, \tag{2.10}$$

This equation indicates a relaxed conditions for measurable scattered intensity from the 3D Laue conditions. The third Laue condition in Eqn.(2.9), $\mathbf{q}\cdot\mathbf{c} = 0$, is not required any more. In other word, all values of q_z are allowed for diffraction as long as the momentum transfer parallel to the surface, $\mathbf{q}_{||}$ equals the surface reciprocal lattice vector,

$$\mathbf{q}_{||} = h\mathbf{a}^* + k\mathbf{b}^*. \tag{2.11}$$

In reciprocal space, this 2D Laue conditions are represented by diffraction rods perpendicular to the surface instead of points. The lateral position of these rods are given by Eqn.(2.11). Since the interference function for a surface can be derived as a product of an infinite lattice truncated by a step function, the surface diffraction rods are also referred as *crystal trunction rods*(CTR). The CTRs from the (001) surface of a simple cubic lattice with an ideal bulk termination are shown in Fig. 2.8 for illustration purpose.

The intensity along the CTRs is modulated by the last term in the interference function in Eqn.(2.10), which is affected by several factors such as the film thickness, reconstructions and surface defects etc. The intensity along these rods is still peaked at the Laue conditions when $\mathbf{q}\cdot\mathbf{c}$ equals $2\pi l$. As the result, the modulation of intensity along the CTRs contains information on the vertical interlayer spacing in the surface region. The $(00l)$ rod is also called the specular rod because there is no momentum transfer in parallel to the surface. Therefore measuring the intensity along the $(00l)$ rod only probes vertical structural information. This will be discussed in detail in Section 2.6.

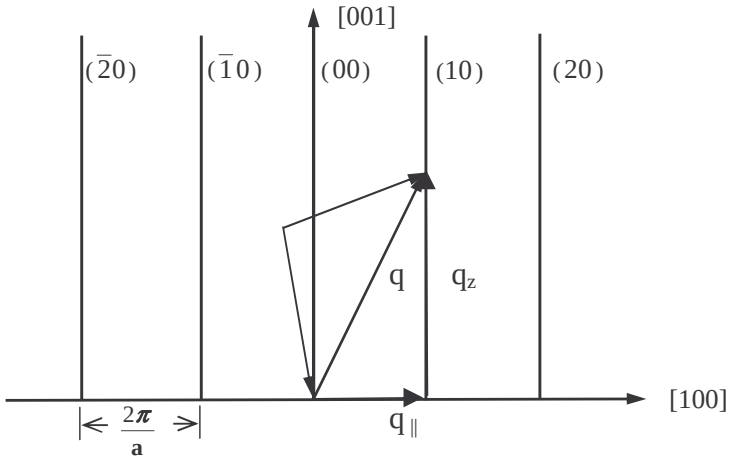

Figure 2.8: Surface diffraction rod of the (001) surface of a simple cubic lattice. Figures from Conrad *et al.*[51]

2.6 Specular Reflectivity of Pb/Si(111) System

X-ray reflectivity measurements is an important technique to identify vertical structural information of a surface within the X-ray penetration length. Qualitative information about the atomic structure of the ultrathin Pb films on Si(111) can be obtained by measuring the reflectivity along the specular rod. The specular reflectivity is sensitive to the positions of all layers and deviation from ideal layer positions within the X-ray penetration length. Such specular rod scans are sensitive only to vertical structure because the moment transfer of the X-rays is normal to the surface.

Since the specular reflectivity depends only on the perpendicular moment transfer vector, q_z, it contains no information about the lateral surface structure. The data can therefore be analyzed using a one-dimensional model. The scattered X-ray intensity $I(\Theta, q_z)$ is given as,

$$I(\Theta, q_z) = |F(\Theta, q_z)|^2, \tag{2.12}$$

in which Θ is the coverage in unit of Pb monolayer (1ML=9.43×10^{14}atoms/cm^2). The perpendicular moment transfer vector q_z will be written in terms of the Si(111) lattice parameter, $a = \sqrt{3}a_0$, where a_0 is the cubic lattice parameter for Si: $q_z = a^* l$, where $a^* = 0.668\text{Å}^{-1}$, and l is the dimensionless reciprocal lattice unit. The scattering amplitude $F(\Theta, q_z)$ is the coherent sum of the contribution from the Pb film and Si substrate, written

in terms of l,

$$F(\Theta, l) = F_{Si}(l) + \frac{\rho_{Pb}}{\rho_{Si}} F_{Pb}(\Theta, l), \tag{2.13}$$

where ρ_{Si} and ρ_{Pb} are the areal density of a Si(111) and Pb(111) plane, respectively. The weighting factor, ρ_{Pb}/ρ_{Si}, properly normalizes the amplitude per Si(111) 1×1 unit cell. Since Si has a diamond lattice structure and Pb has a *fcc* lattice structure, their relative areal number densities for the (111) plane are given by:

$$\frac{\rho_{Si}}{\rho_{Pb}} = 2(\frac{a_{Si}}{a_{Pb}})^2, \tag{2.14}$$

in which a_{Si} and a_{Pb} are cubic lattice constant for Si and Pb, respectively.

The Si substrate contribution contains two terms: (i) the amplitude from a bulk terminated surface and (ii) the amplitude from a Si(111)7×7 reconstructed surface lying on top of the bulk.

$$F_{Si}(l)_{bulk} = f_{Si}(1 + e^{-2\pi il/12})(1 + e^{-2\pi il/3} + e^{-4\pi il/3}), \tag{2.15}$$

where f_{Si} is the atomic factor for Si. The scattering amplitude of the substrate crystal is obtained by summing the contribution from an infinite Si bulk slap,

$$F_{Si}(l)_{crystal} = F_{Si}(l)_{bulk} \sum_{n=0}^{-\infty} e^{i2\pi ln} \alpha^n = \frac{F_{Si}(l)_{bulk}}{1 - \alpha e^{-2\pi il}}, \tag{2.16}$$

where α describes the attenuation of beam penetrating one Si atomic layer and $\alpha \simeq 1$ for an X-ray beam. The top layers of the substrate are assumed to retain the Si(111) 7x7 reconstruction structure of the conventional dimer, adatom and stacking fault (DAS) model[7][10]. In this model, there are 12 top layer adatoms, 42 two atoms in the second layer and 48 atoms in the third layer. As each layer of Si(111) 7x7 reconstruction represented by a height parameter z_j, the scattering from the surface reconstruction of the DAS model is:

$$F_{Si}(l)_{DAS} = f_{Si}[\frac{12}{49} e^{-2\pi ilz_1} + \frac{42}{49} e^{-2\pi ilz_2} + \frac{48}{49} e^{-2\pi ilz_3}]. \tag{2.17}$$

The height parameters, z_j, are obtained from the fit to a clean Si(111) reflectivity data and found to be consistent to Robinson and Vlieg[7]. Hereby the scattered amplitude of the Si substrate, $F_{Si}(l)$, is given as:

$$F_{Si}(l) = F_{Si}(l)_{bulk} \frac{-e^{2\sigma_{Si}^2 \sin^2(\pi l)}}{1 - e^{-2\pi il}} + F_{Si}(l)_{DAS}. \tag{2.18}$$

Note that the numerator of the first term includes a substrate roughness factor, $e^{2\sigma_{Si}^2 \sin^2(\pi l)}$. This term models the loss of intensity due to a finite density of Si steps (assumed to be made of Si bi-layer heights). σ_{Si}^2 is the root mean square deviation of the Si(111) surface due to these steps. All samples used in these experiments contain only bi-layer steps as determined from measurements of the (00l) rod Full Width Half-Maximum (FWHM) as a function of l[51].

There could be various ways to model the Pb films, depending on the actual film morphology. For low temperature deposition that Pb film follows layer-by-layer growth, the scattering amplitude can be represented with fractional layer occupancy parameters and average layer positions[16]. At the experimental temperatures in this work, Pb films follows a layer-plus-islands growth mode, thus the scattering amplitude can be described with surface fractional occupancy of islands of different heights and with different interlayer spacings. The actual model used to fit the experimental data in this work will be discussed in detail in next chapter.

2.6.1 Transverse Rod Scan

The X-ray diffraction pattern of a surface is in the form of perpendicular rods, as discussed in Section 2.5.2. These rods have a finite width due to the fact that real surfaces are subject to surface roughness, atomic steps and mosaics etc. Therefore the diffraction intensity along the rod must be integrated transverse to the rods. There are several methods to perform the transverse rod scan. After the incident angle θ_i and the outgoing angle θ_f, positioned by the point detector, have been set up for a given $\mathbf{q}$ on the specular rod, the scattering intensity can be measured while rotating the sample normal within the scattering plane which is the perpendicular plane defined by the vectors $\mathbf{k}_i$ and $\mathbf{k}_f$. The scattering geometry is shown in Fig. 2.9(a). This method essentially rocks the surface rod in reciprocal space around its initial position, therefore the term *rocking curve method*. When the sample normal is slightly shifted from its specular position by angle $\triangle\theta$, the momentum transfer

has a in-plane component parallel to the surface, $\mathbf{q}_{||}$, and a perpendicular component q_z,

$$q_{||} = k[\cos(\frac{2\theta}{2} - \triangle\theta) - \cos(\frac{2\theta}{2} + \triangle\theta)] \tag{2.19}$$

$$q_z = k[\sin(\frac{2\theta}{2} - \triangle\theta) + \sin(\frac{2\theta}{2} + \triangle\theta)]. \tag{2.20}$$

Given a very small rotation angle $\triangle\theta$, the two components can be approximately given as $q_z \simeq q$ and $q_{||} \simeq q\triangle\theta$ while $q = k\sin(\frac{2\theta}{2})$ is the magnitude of the momentum transfer. Since the scattering beam and detector position do not move, the magnitude of momentum transfer vector remains the same. The transverse scan itself measures the diffracted intensity as a function of in-plane momentum transfer $q_{||}$ for a specific value of q_z. Background subtraction together with integration over $q_{||}$ give the total intensity for the given diffraction rod.

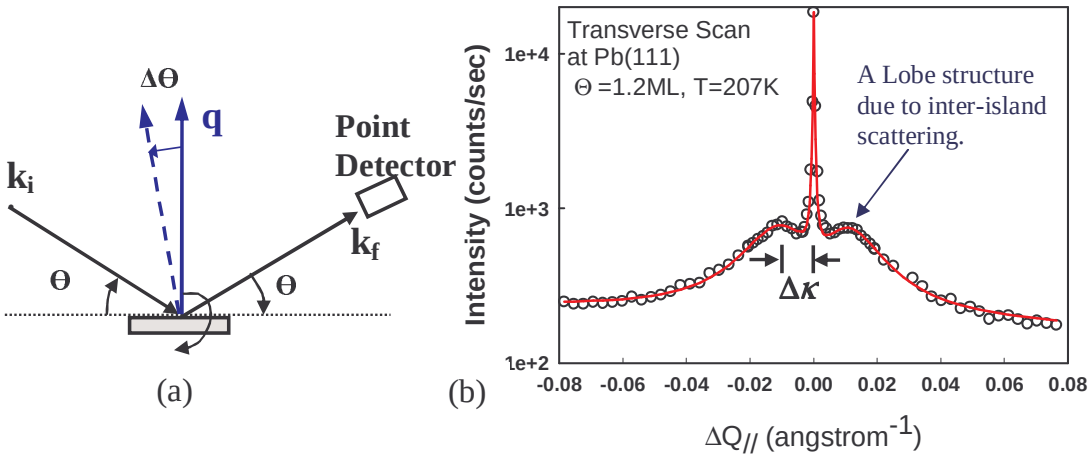

Figure 2.9: (a) The scattering geometry of the rocking curve method. Since the point detector only measures one point in space, the sample normal is rotated within the scattering plane with incident beam and the detector fixed. (b) Typical transverse scan at Pb(111) Bragg position. The lobe structure is due to inter-islands scattering.

The width of a specular peak varies with q_z and reveals the information of the surface morphology. The measured width, $\triangle\theta$, has several components due to mosiacs, step distributions and the detector slits angular acceptance etc., and can be written as,

$$\triangle\theta^2 = \triangle\theta^2_{\text{mosaics}} + \triangle\theta^2_{\text{steps}} + \triangle\theta^2_{\text{slits}} + \cdots. \tag{2.21}$$

The reciprocal width obtained from the transverse scan $\triangle q_{||}$ is related to both the scattering angle 2θ and angular width $\triangle\theta$ through $\triangle q_{||} \propto \sin(\frac{2\theta}{2})\triangle\theta$. Thus the broadening of the rod's

angular width observed at small scattering angle does not necessarily imply a broadening in reciprocal width. When $2\theta \rightarrow 0$, the angular width eventually becomes too large to determine. The point detector has an angular acceptance limited by a pair of entrance slits. The resolution of the rod intensity measurement arises from the finite width of the pair of slits. Since the slits accept intensity over a small angular range, the measured scattering intensity is actually an integral of the intensity over a finite area in reciprocal space. Normally one slit is narrowed to minimize the angular resolution, and the other slit is relatively wide to maximize the integration area. In all experiments, the horizontal geometry is used to take the transverse scans, i.e the sample is mounted vertically and the the μ axis of the diffractometer is used to rotate the sample around its normal. In that case, the slits are generally set to 0.02mm (horizontal)$\times$0.04mm (vertical) open.

For a surface that has an in-plane ordered structure, such as a uniformly distribution of islands, transverse rod scan will have additional peaks other than the specular one, typically in a form of lobe structure, as shown in Fig. 2.9(b). The correlation length, or the mean island separation $\langle L \rangle$, is related to the position of the lobe peaks relative to the Bragg peak($\pm\triangle\kappa$),

$$\langle L \rangle = 2\pi/\triangle\kappa, \tag{2.22}$$

where $\triangle\kappa$ is in reciprocal units. By a simple argument that the island separation is much larger than the island sizes, the number of islands per unit area, n, is determined by the mean island separation as,

$$n = 1/\langle L \rangle^2. \tag{2.23}$$

This method of determining average island density is known to be accurate to order one.[42] The effect of lobe shape on the value of n was found to be negligible as determined from 2D reciprocal space maps of the diffraction spots.

The rocking curve method using a point detector provides high resolution rod intensities, but requires long data collection times. A kinetic study of the early stage growth of Pb islands grown on Si(111) substrate employs a CCD detector to take transverse rod scan. The utility of the CCD camera lies in the ability to obtain snapshots of the reciprocal-space map of the surface on a very short timescale. The scattering geometry is shown schematically in

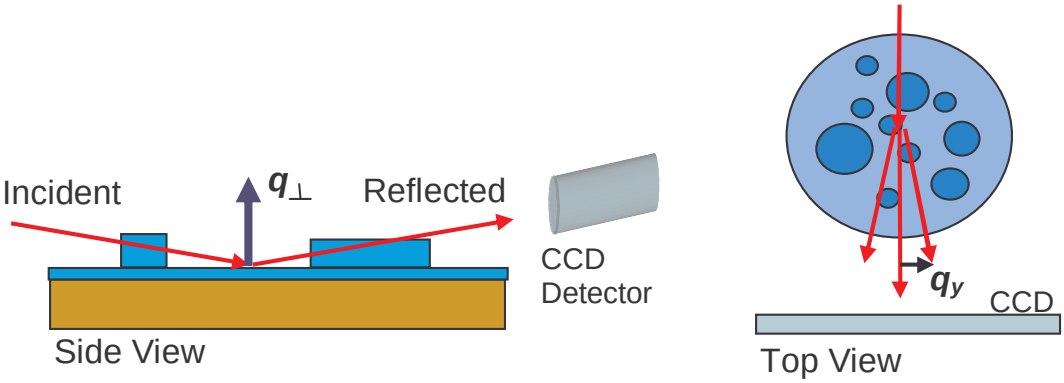

Figure 2.10: The scattering geometry using a CCD detector from a surface with presence of islands. The incident and reflected angels are lined up then fixed at Bragg reflection positions. The CCD image plate is placed perpendicular to the reflected beam. The top view exhibits the 2D feature of the image. The detector collects scattering within a range of q_y and q_x(perpendicular to q_y along the detector surface).

Fig. 2.10. After the sample and detector have been lined up and fixed at Bragg reflection, a MAR-165 CCD detector is placed at about 870mm from the sample at the same horizontal level, with detector plate perpendicular to the reflected beam. The CCD detector is capable of taking snapshots every 5 seconds because there is no motor motion required. There is a 5 second dead time for each image to be downloaded to the computer. The pixel size was calibrated to scattering angles by comparing the shift of a diffraction as the sample was rotated. For these experiments an $80\mu m \times \mu m$ pixel was used that corresponds to an angular resolution of 0.005 degrees.

The data collected by the CCD detector are images representing a reciprocal space mapping of the surface. Figure 2.11 show two images as examples that were taken from the surface during early growth and at a later time when more Pb had been deposited. The big bright circular area at the right side of the two images are from diffuse scattering from the Si(111) Bragg peak. The small bright spot within the dashed frame is the Pb(111) Bragg peak. At early time, there is no additional peaks other than the Pb Bragg(111) peak. With more Pb on the surface, a diffuse ring structure eventually shows up and grow around the Bragg peak.

The increase in diffuse intensity with Pb deposition can be analyzed to provide information on the development of islands on the surface. Ideally, the entire image would be

analyzed using a 3D model. However, such a model would be very labor-intensive to develop and would require much more computer processing power. An alternative way is to take slices of the data to turn the 2D images into 1D lines through a projection process. The dashed frame in Fig. 2.11 is a typical projection window used to analyze the data. Given the pixel size and the distance from the sample to the detector, peak separation in pixels can be converted to angular position, and eventually to moment transfer units.

The y axis of the images in Fig. 2.11 corresponds to the scattering intensity as a function of the moment transfer out of the scattering plane, q_y, as marked in Fig. 2.10. However, the x axis of the images corresponds to the scattering intensity as a function of moment transfers within the scattering plane, where both q_x and q_z are changing. As a result, the diffuse ring around the Pb(111) Bragg peak is elongated in the horizontal direction. For simpler data analysis, projections along the y axis have been performed. In general, the projection window is 25 pixels wide and 400 pixel long (dashed frame in Fig. 2.11). The horizontal location of the window can be chosen to be either centered at the Pb Bragg peak, or slightly shifted from the Bragg peak. By avoiding the intense Bragg peak, this shifting improves the resolution of the diffuse intensity and makes the data fitting easier. Note that the later time plot in Fig. 2.11 exhibits a lobe structure similar to the transverse rod scan taken by a point detector in Fig. 2.9. Once the peak separations have been obtained through data fitting, the mean island separation together with island density can be calculated using Eqn.(2.22) and Eqn.(2.23).

The major advantage of CCD detector is that the data can be collected in a very small time scale, which favors the kinetic study. However, the utility of CCD detectors has some disadvantages. Normally there are several hundreds of scans collected in a three-hour time period for each flux rate and temperature, the data analysis of so many 2D images are complicated and requires more computational workload. Also the CCD detector collects more background scattering than the point detector, which uses a pair of slits to efficiently blocking out photons diffusely scattered from other sources (such as the Be window). In addition, the very intense Bragg peak can saturate its corresponding pixels on CCD in a very short amount of time, which limits the exposure time. Since the lobe peaks are magnitudes

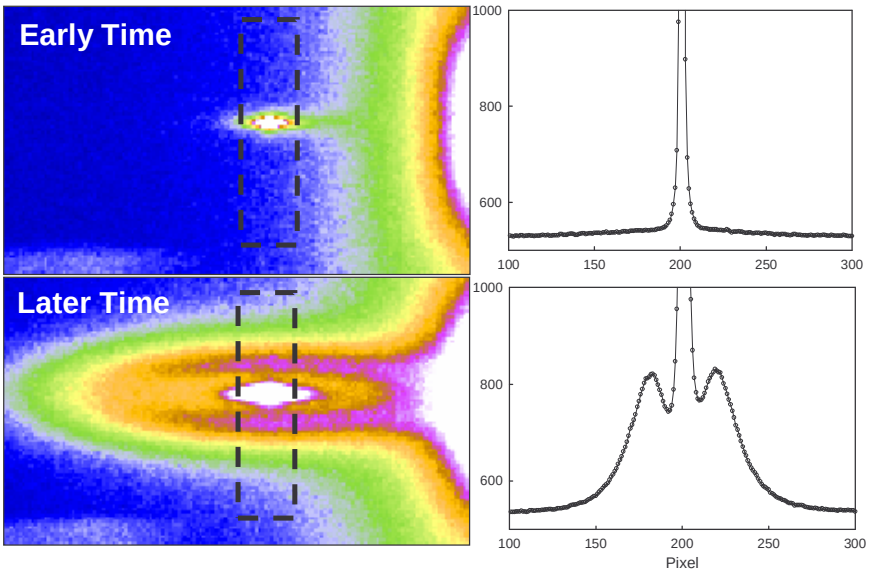

Figure 2.11: Images taken with a Mar-165 CCD detector during early growth and after a certain amount of Pb has been deposited. The big bright circular area at the right side of the two images are diffuse around Si(111) Bragg peaks. The small bright spot within the dashed frame are Pb(111) Bragg peaks. A diffuse ring structure shows up with Pb islands present on the surface.

weaker than the Bragg peak, the data statistics is limited by the data collecting time when the lobe intensity is of interest. This problem was improved by inserting known attenuators into the incident beam just before the Bragg peak saturated the CCD.

CHAPTER III

INTERFACE STRUCTURE OF PB ISLANDS ON SI(111) 7×7

3.1 Introduction

The Pb/Si(111) system has been studied intensively as a prototypical metal-on-semiconductor model that exhibits strong Quantum Size Effect (QSE). When a metal and a semiconductor are brought into contact, the Fermi levels in the two materials must be aligned in thermal equilibrium, causing charges flow from one side to the other.[53] The charge flow forms a space charge layer, depletion or accumulation, in the semiconductor, therefore a potential barrier (Schottky barrier) has to be overcome when an electron is excited from the metal into the conduction band of the semiconductor. The interface structure determines charge transfer into the islands and controls the Fermi level position, thus it is critical to determine the QSE energy levels and the total energy of a Pb island. It has been shown that the Schottky barrier height (SBH) of the Pb/Si(111) interfaces affects the stability of the islands.[2]. In order to form QSE metal islands on semiconductors, a smooth island-substrate interface is necessary to set up the electron standing waves that lead to the new quantum confined states, as observed in experiments.[40] How this occurs for the Pb-Si(111)7×7 system is a mystery because of the large lattice mismatch and the highly corrugated 7x7 reconstruction. Our recent work uses surface x-ray scattering to study the details of the island-Si interface under various growth conditions in order to address the issues of interface structure and its relation to the strong QSE observed in this system.

In this work, the scattering around the Bragg reflection has been studied using transverse rod scans at the Pb(111) Bragg position. The coverage dependence of the total intensity reveals that the Pb islands grow on top of the Si surface instead of on the wetting layer as previously reported[45, 38]. A scattering model has been presented to show that the

Pb nanocrystals have an interface with the Si substrate rather than with the Pb wetting layer. After the initial amount of Pb ($\sim$ 1ML) has been deposited on the Si(111) 7×7 substrate, crystallized islands start to nucleate on top of this monolayer-thick wetting layer as more Pb beyond a monolayer coverage is deposited. Although the wetting layer forms before island nucleation, the portion of the wetting layer below the island is transformed into fcc sites and is incorporated into the growing islands while the wetting layer structure between the islands remains the same as the islands grow. This interface picture provides a good explanation that the well defined boundary condition allows QSE effects to develop. Otherwise scattering from a rough wetting layer-island interface will destroy the coherence of the electron standing wave. However it does not explain how metal films grown on the highly corrugated Si(111) 7×7 surface can achieve a smooth metal-Si interface.

To address this question, specular reflectivity measurements of the Pb/Si system have been carried out. In order to determine the interface structure, an structure model has been formulated from which the X-ray intensity is calculated and compared to the data. The model calculation gives the best fit to the data with well-ordered *fcc* stacked Pb islands peaked at 8-layer. The analysis of the reflectivity data further supports that *fcc* islands extend to the substrate interface. Note that at this temperature and coverage LEED and STM measurements show that Pb islands grow to seven-layers high. With this model, the X-ray data is consistent with the island heights determined by using LEED and STM. The actual island height are 1-layer higher than determined by these techniques since they only view the surface topography and measure heights relative to the inter-island Pb wetting layer.

The experiments were performed using 12.4keV photon energy ($\lambda = 0.9998$Å). The Pb films were deposited *in situ* in UHV ($p \sim 2 \times 10^{-10}$Torr) from an e-beam evaporator on a Si(111) 7x7 substrate. The Si(111)7×7 reconstruction surface was produced using the technique described in Chapter 2 and exhibited sharp LEED spots. Coverage of Pb, Θ, are defined in units of the bulk Pb(111) surface density (1.0ML=1.89×10^{15} atoms/cm^2). Momentum transfer vector, $\mathbf{q}$, is defined in reciprocal lattice unit for the conventional hexagonal Si(111) unit cell ($a_0 = 5.4307$Å). The component normal to the surface is $q_z =$

la_0^*, and the component parallel to the surface is $q_{||} = ha_1^*$, where $a_0^* = 0.668\text{Å}^{-1}$ and $a_1^* = 0.771\text{Å}^{-1}$.

3.2 X-ray Scattering at Pb(111) Bragg position

3.2.1 Scattering Model

To quantitatively analyze the data of coverage-dependent scattering intensities, a model has been derived to calculate the reflected intensity from a distribution of islands. The scattering from the substrate was neglected because it is relative small comparing to the scattering from the Pb film. Let $\Theta(\vec{r})$ be the coverage(in Pb monolayer) of the *fcc* Pb film at a lateral position $\vec{r}$. The $\Theta(\vec{r})$ function essentially describes an one-dimensional island height distribution over the surface. Also let $h(\vec{r})$ be the height of the wetting layer upon which the *fcc* Pb crystal is formed, with its variance representing the surface roughness. The scattering amplitude consists of an in-plane component and a perpendicular component,

$$A(\mathbf{q}) = A_0 \sum_{\vec{r}} e^{iq_{||}\cdot\vec{r}} \sum_{j=0}^{\Theta(\vec{r})-1} e^{iq_z(dj+h(\vec{r}))}, \tag{3.1}$$

where d is the spacing between Pb(111) planes. Since q_z is near a Bragg point, $q_z d = 2\pi m + \delta$ with $\delta << \frac{1}{\Theta(\vec{r})}$, an approximation can be made for the sum,

$$\sum_{j=0}^{\Theta(\vec{r})-1} e^{iq_z dj} = \frac{1 - e^{iq_z d\Theta(\vec{r})}}{1 - e^{iq_z d}} \simeq \Theta(\vec{r}). \tag{3.2}$$

The condition $\delta << \frac{1}{\Theta(\vec{r})}$ might be invalid for very thick film, but it is a good approximation for the ultra-thin film in this work. Equation (3.1) can thus be written as,

$$A(\mathbf{q}) = A_0 \sum_{\vec{r}} e^{iq_{||}\cdot\vec{r}} e^{iq_z h(\vec{r})} \Theta(\vec{r}). \tag{3.3}$$

The differential scattering cross section at $\mathbf{q}$ is given by,

$$\begin{aligned} S(\mathbf{q}) = AA^* &= I_0 \sum_{\vec{r}} e^{iq_{||}\cdot\vec{r}} \sum_{\vec{r'}} \Theta(\vec{r}+\vec{r'})\Theta(\vec{r'}) e^{iq_z[h(\vec{r}+\vec{r'})-h(\vec{r'})]} \\ &= I_0 \sum_{\vec{r}} e^{iq_{||}\cdot\vec{r}} \langle \Theta(\vec{r}+\vec{r'})\Theta(\vec{r'}) e^{iq_z[h(\vec{r}+\vec{r'})-h(\vec{r'})]} \rangle_{\vec{r'}}, \end{aligned} \tag{3.4}$$

where the brackets refer to an ensemble average over the entire surface, $\vec{r}$ refers to the relative position to $\vec{r'}$, and I_0 is the incident beam intensity. Assuming that $h(\vec{r})$ is correlated on

very short distance and uncorrelated with $\Theta(\vec{r})$, we can write,

$$S(\mathbf{q}) = I_0 \sum_{\vec{r}} e^{iq_{||}\cdot\vec{r}} \langle \Theta(\vec{r}+\vec{r'})\Theta(\vec{r'})\rangle_{\vec{r'}} \langle e^{iq_z[h(\vec{r}+\vec{r'})-h(\vec{r'})]}\rangle_{\vec{r'}}. \tag{3.5}$$

Equation (3.5) of $S(\mathbf{q})$ can be written as the sum of a Bragg and a diffuse component, $S(\mathbf{q}) = S_B(\mathbf{q}) + S_D(\mathbf{q})$, while the Bragg component is only non-zero at $q_{||} = 0$. Integrating $S(\mathbf{q})$ over $\vec{q_{||}}$ gives the total integrated intensity as,

$$\int S(\mathbf{q}) dq_{||} = B\langle \Theta(\vec{r}+\vec{r'})\Theta(\vec{r'})\rangle_{\vec{r}=0} \langle e^{iq_z[h(\vec{r}+\vec{r'})-h(\vec{r})]}\rangle_{\vec{r}=0} = B\bar{\Theta^2}, \tag{3.6}$$

where B is a normalization constant. Correspondingly, the integrated intensity can be written as the sum of a Bragg and a diffuse component. The Bragg intensity is only related to the coverage in *fcc* Pb islands and the vertical displacive disorder of the wetting layer, σ^2, defined as the mean-square interface roughness between the Pb and Si,

$$\lim_{\vec{r}\to\infty} \langle e^{iq_z[h(\vec{r}+\vec{r'})-h(\vec{r'})]}\rangle_{\vec{r'}} = e^{-q_z^2\sigma^2}. \tag{3.7}$$

Therefore the integrated Bragg and diffuse intensity are given as, respectively,

$$I_B(\mathbf{q}) = \int S_B(\mathbf{q}) dq_{||} = B\bar{\Theta}^2 e^{-q_z^2\sigma^2} \tag{3.8}$$

$$I_D(\mathbf{q}) = \int S_D(\mathbf{q}) dq_{||} = B(\bar{\Theta^2} - \bar{\Theta}^2 e^{-q_z^2\sigma^2}), \tag{3.9}$$

with $\bar{\Theta}$ the average *fcc* Pb islands coverage over the entire surface. Since $\bar{\Theta}$ is constant for a fixed coverage deposition, the Bragg integrated intensity is determined by the wetting layer roughness. In the case where the wetting layer has atomic scale disorder correlated over a very short range, the portion of the diffuse scattering from the interfacial disorder at the buried interface can be neglected, i.e. the second term in the integration of Eqn.(3.6) is $e^{-q_z^2\sigma^2}$ instead of 1. Then the integrated diffuse intensity can be given by,

$$I_D(\mathbf{q}) = Be^{-q_z^2\sigma^2}(\bar{\Theta^2} - \bar{\Theta}^2) \tag{3.10}$$

where the term in the bracket represents the variance of island height distribution across the surface. Equation (3.9) and (3.10) shows that the integrated diffuse is determined by the island height distribution and the vertical roughness of the wetting layer.

3.2.2 Experimental Results

As a first experiment, stepwise deposition of Pb on Si(111) were carried out under the experimental conditions mentioned above for coverage up to 22ML. Initially Pb was deposited in 0.25ML increments at a rate of 0.39ML/min onto the Si(111) substrate with the flux rate calibrated to be within ±10%. Larger increment was taken for Pb coverage beyond 4ML at the same flux rate. The substrate temperature was held at 227K during deposition and for all subsequent measurements. This temperature was in the range of temperature where Pb growth follows the layer plus island mode. The Pb(111) Bragg position is located at $l = 3.27$ due to the smaller lattice parameter for Pb (4.9496Å). The scattering geometry was aligned and fixed at the Pb(111) Bragg positions. The deposition time plus the data collecting time was ∼10min for each coverage increment. After each increment, the deposition was interrupted and a transverse scan was taken through the Pb(111) Bragg position by collecting scattered photons while rotating the sample about its surface normal within the scattering plane. Some of the transverse rod scans at Pb(111) Bragg position were shown in Fig.(3.1). The x axis is the incident angle controlled by motor μ, rotating about its Bragg position. Note that a scan taken at the clean Si sample is subtracted from each scan, and the data set of each scan is scaled for illustration purposes.

The intense sharp peak at the center in Fig. 3.1 is the specular peak corresponding to the Bragg component at $q_z = 3.27$ and $q_{||} = 0$. The width of the Bragg peak is resolution-limited ($< 0.005°$). A diffuse lobe structure, a feature due to inter-island scattering (Henzler rings)[14], starts to show up for coverages greater than 1.2ML. The intensity of the lobe peak is order of magnitudes weaker than that of the Bragg peak. Assuming that the rocking angle is small, the position of the lobe peaks relative to the Bragg peak in unit of degrees, $\pm\triangle\mu$, can be approximately converted to the shift in moment transfer, $\pm\triangle q_{||}$, as $\triangle q_{||} = q_z \triangle\mu \frac{\pi}{180}$. And $\triangle q_{||}$ is related to the mean island separation, $< L >$, that $\triangle q_{||} = 2\pi / < L >$. The existence of the lobe peaks indicates three-dimensional islands forming on the surface. The mean island separation is found to be about 300Å at the early stage of island growth. The peak separation of diffuse lobes decreases with coverage and essential becomes unresolved when the lobe peaks merge with the central specular peak.

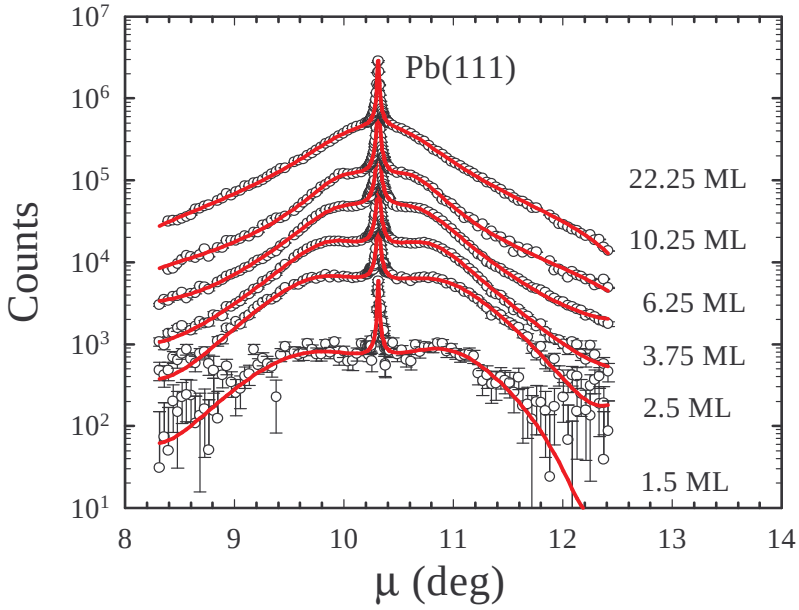

Figure 3.1: Transverse scans measured across the Pb(111) Bragg peak for selected coverages after stepwise depositions. The sample temperature is 227K and the deposition flux was 0.39 ML/min. Solid curves are fits using a Gaussian central peak and a pair of Lorentzians for the diffuse lobes.

In that case, the diffuse component mainly arises from short-length correlations such as thermal vibration and roughness at surfaces[29].

The Bragg peak and the lobe peaks in each transverse scan can be fitted using a Gaussian function and a pair of Lorentzian function, respectively, shown in solid curves in Fig. 3.1. The integrated intensities of both Bragg component and diffuse component can thus be obtained from these fits and plotted in a function of coverage in Fig. 3.2. Below 1.2ML, the Bragg intensity hardly varies with coverage, indicating that the first layer of Pb is highly disordered. Since the vertical disorder would strongly suppress the Bragg reflection, more Pb depositing on the surface does not result in high reflected intensity. The absence of diffuse intensity further suggests that the wetting layer has atomic-scale disorder correlated over only a very short length. The wetting layer density, $\Theta_w = 1.2$ML, is in excellent agreement with values from both low and room temperature growth studies of Pb on Si(111)[4, 6, 44]. Above 1.2ML, both Bragg and diffuse intensities increase with Pb coverage. The increase of Bragg intensity arises from the formation of *fcc* stacked Pb sites while the increase of diffuse

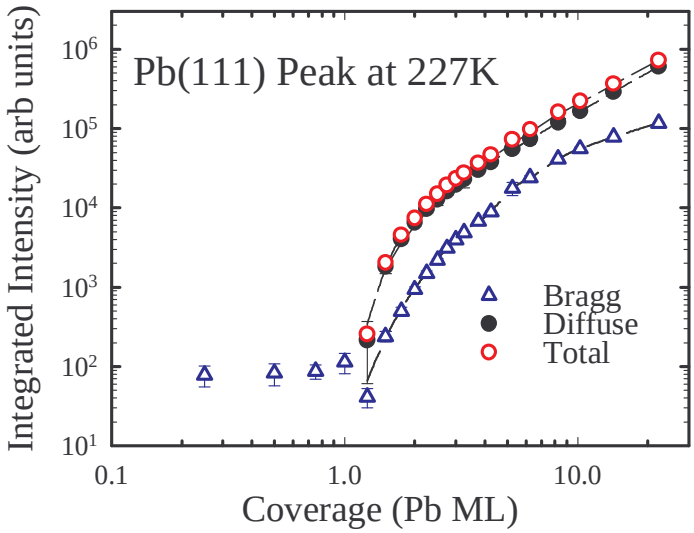

Figure 3.2: Integrated Bragg(open triangle), diffuse(open circle) and total(filled circle) intensity vs. Pb coverage taken at the Pb(111) Bragg position. The dashed curve is the Bragg intensity calculated for $\sigma = 0$.

intensity arise from the correlation of islands distributed on the surface. The behavior of both the Bragg and diffuse intensity indicate the onset of *fcc* stacked Pb islands only occurs above 1.2ML. The coverage dependence of the scattering around the Bragg reflection reveals the evolution of vertical ordering at the Pb-Si interface.

3.2.3 Analysis and Discussions

The growth behavior of both Bragg and diffuse intensities can by analyzed using the scattering model mentioned in Section 3.2.1. When the Pb coverage is less than Θ_w, Pb atoms fill adsorption sites on the Si substrate, forming a monolayer-thick wetting layer. The Bragg intensity is determined by the vertical position of these sites and the sequences of them being filled. The increment of each deposition is 0.25ML, thus there are not enough data points below 1ML to provide the vertical positions of the available adsorption sites. Additional experiments were taken to further study the coverage dependence of Bragg intensity in the early growth, which will be discussed in detail in Section 3.4. The increase of deposition coverage did not lead to the increase of Bragg intensity, indicating high roughness in the wetting layer that suppressed the Bragg intensity. Due to the absence of islands and the short correlation length of atoms in the wetting layer, the diffuse lobes were too weak to

be distinguished from the central specular peak. As a result, the Bragg intensity is not significant and there is no diffuse intensity.

With Pb coverage beyond Θ_w, Pb atoms start to nucleate on the wetting layer and grow into *fcc* crystallized islands, leading to the rise of both Bragg and diffuse intensities. Because the Pb(111) Bragg peak is strong above 1.2ML, we must assume that the islands are not nucleating on top of the rough wetting layer. Therefore, in order to fit the data it was necessary to assume that as islands form, parts of the wetting layer below the islands are transformed to *fcc* sites. Given the fractional surface coverage of islands p_i, the coverage in Pb islands (in unit of Pb monolayer) equals the total deposited coverage minus the wetting layer coverage between islands, i.e. $\bar{\Theta} = \Theta - (1 - p_i)\Theta_w$. Note that Θ_w is slightly greater than 1ML implies a higher wetting layer density than its bulk density. Approximations can be made when p_i is small so that $\bar{\Theta} = \Theta - \Theta_w$. Equation (3.8) of the integrated Bragg intensity can be rewritten as:

$$I_B(\mathbf{q}) = B(\Theta - \Theta_w)^2 e^{-q_z^2\sigma^2}, \tag{3.11}$$

with B a constant and $\Theta_w \sim 1.2$ML defined as the point when the diffuse lobes show up.

Equation (3.11) can be used to fit the X-ray scattering data. The roughness term σ was found to be zero in order to give a good fit to the Bragg intensity data in the range of $1.2ML < \Theta < 14ML$. The fit with $\sigma = 0$ is shown as the dashed curve in Fig. 3.2. This result suggests a smooth interface between the Pb nanocrystals and the substrate. It would be impossible to reconcile the increase in Bragg scattering at higher coverage if the Pb nanocrystals were to reside on top of the disordered wetting layer, otherwise the vertical displacive disorder at the buried interface would strongly suppress the Bragg intensity. Both the Bragg and the diffuse intensity versus Θ can be explained if the Pb islands transform material in the wetting layer beneath them into *fcc* Pb for $\Theta > 1.2$ML. A basic conclusion could be made that the Pb nanocrystals have a interface with the Si substrate rather than with the rough wetting layer.

Based on the analysis mentioned above, the picture of the surface interface is that there are isolated fcc stacked Pb islands on top of the flat Si substrate with a disordered wetting

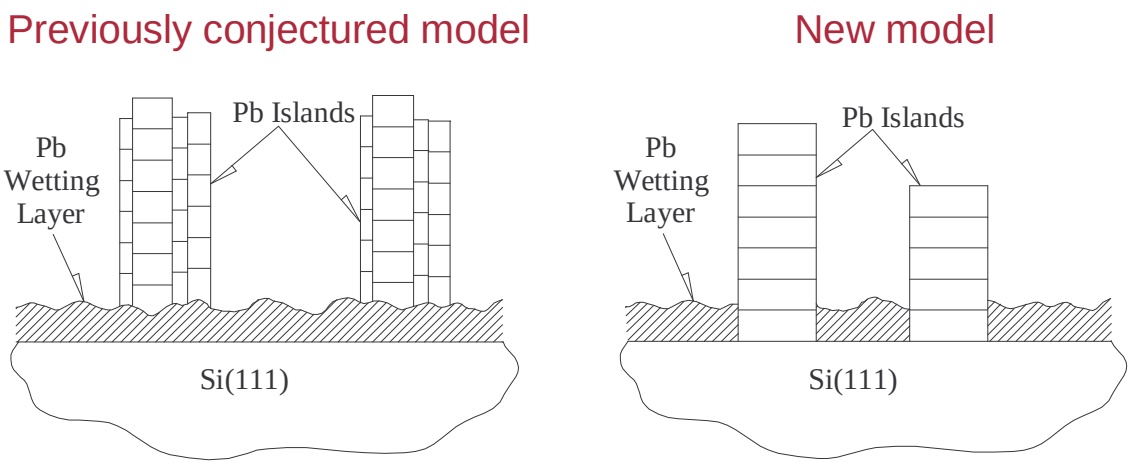

Figure 3.3: A schematic structural model illustrating the basic conclusion that the Pb nanocrystals have an interface with the Si substrate rather than with the wetting layer.

layer occupying the region between the islands. A schematic structural model is shown in Fig. 3.3. Instead of the previous conjectured model where the islands form on a highly disordered wetting layer, the Pb islands are directly on top of the Si substrate with the wetting layer between islands remain disordered.

For $\Theta > 14ML$, the dashed line of $\sigma = 0$ in Fig. 3.2 could not fit the data. The decrease of the Bragg scattering in comparison with the $\sigma = 0$ curve denotes a larger roughness. The increase in σ occurs near the coverage where the QSE islands begin to coalesce into a closed film, suggesting that it might arise from the misfit strain relaxation between the film and the substrate. This is demonstrated in Fig. 3.4 which compares transverse scans at the Pb(111) with those taken at the Pb(222) Bragg peaks. For the data taken at low coverage in Fig. 3.4(a), the diffuse scattering at both Bragg positions scales with $q_{||}$ and thereby exhibits the correlated behavior associated with inter-island scattering. However, in Fig. 3.4(b) taken at the higher coverage of $\Theta = 22.25ML$, the diffuse scattering scales not with $q_{||}$ but with the sample rocking angle, $\triangle\omega$, indicating a mosaic relationship coming from crystalline defects[29].

In conclusion, X-ray scattering data shows that Pb islands do not grow on top of a Pb wetting layer as previously conjectured. Instead islands nucleating on the wetting layer transform the Pb in the wetting layer beneath them into *fcc* sites within the islands. The

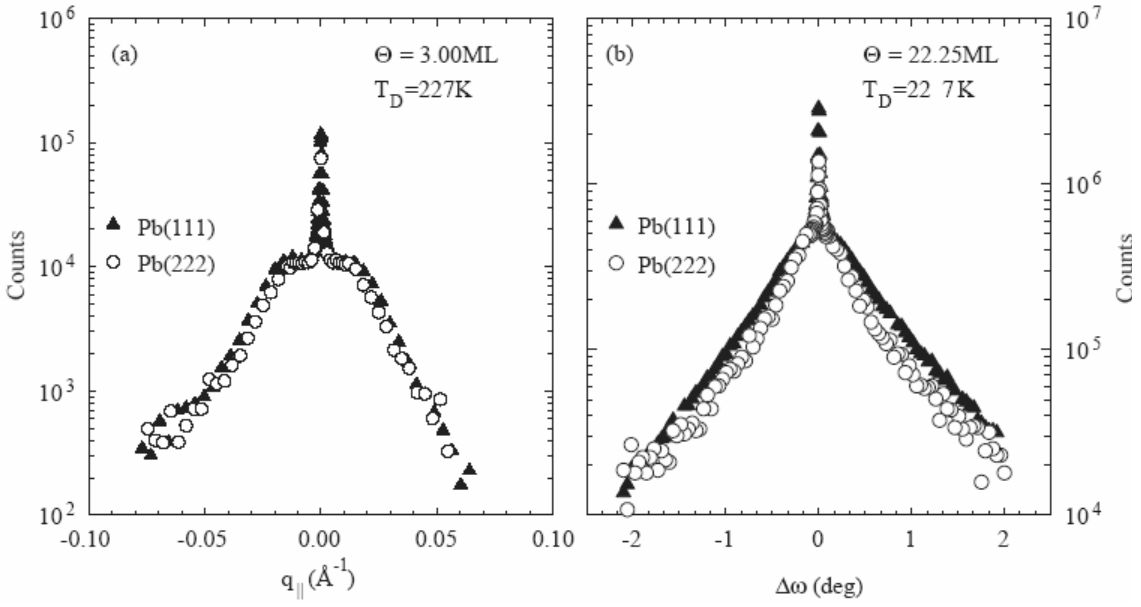

Figure 3.4: Comparison of transverse scans across the Pb(111) and Pb(222) Bragg position. (a) For $\Theta = 3ML$ the diffuse scattering scales with $q_{||}$, indicating correlated inter-island scattering. (b) For $\Theta = 22.25ML$, the diffuse scattering scales with the sample rocking angle $\triangle\omega$, indicating a mosaic-like disorder arising from crystalline defects.

surface therefore consists of Pb islands attached directly on top of the Si substrate with a disordered Pb layer between islands. This layer is gradually consumed as the islands grow in size and coalesces into a 2D closed film. These results have important implications for theoretical models used to predict the island height distribution, since they firmly establish the depth of the quantum well used to determine the island total energy contribution from electron confinement. Finally, the smooth island-substrate interface measured in these studies is consistent with the boundary condition for coherent electron scattering necessary to produce quantum well states in the islands.

3.3 Specular Reflectivity Analysis

3.3.1 Structural Model

To get more detail on the Pb-Si interface beyond integrated intensities, we have performed x-ray reflectivity measurements. This section outlines the structural model used to analyze the experimental X-ray reflectivity data. The specular reflectivity depends only on the perpendicular moment transfer, q_z, therefore a one-dimensional model can be developed to

fit the data. As the scattering from the Si substrate has been discussed in Section 2.6, only the scattering amplitude from the Pb film will be described.

The scattered amplitude, $F_{Pb}(\Theta, l)$, from the Pb film in Eqn.(2.13) must take into account a number of morphological requirements that are known to exist on the Pb/ Si(111)7 $\times$ 7 system. First, Pb grows in a pseudo Stranski-Krastanov (layer plus island) growth mode on Si(111)7 $\times$ 7 for temperatures between 150K to 290K[4]. Pseudo in this system means that the islands grow on top of the Si substrate and not on top of the wetting layer that fills the area between islands. This wetting layer is known to be vertically rough as demonstrated in the last section[40]. The model must therefor allow for at least two different Si-Pb separations; the Si-wetting layer, D_w, and the Si-island separation, D_0. Correspondingly, at least two vertical roughness terms are allowed; the wetting layer, σ_w, and the Pb islands ,σ. To describe the island height distribution, an occupancy parameter p_n is defined as the fractional surface area covered by all Pb islands with n layers thick, where p_1 is the 1-layer wetting layer coverage, as illustrated in Fig. 3.5. Given the number of layers in the highest islands, N, p_n is subject to two constraint equations for the total coverage, Θ, and for the total area:

$$\sum_{n=0}^{N} p_n = 1, \tag{3.12a}$$

$$\sum_{n=0}^{N} n p_n = \Theta. \tag{3.12b}$$

The $n = 0$ term allows for part of the surface to not be covered with Pb. This term, while not important for high coverages, will allow us to vary the wetting layer density when discussing data from surfaces with coverages below a monolayer Pb coverage. Both p_n and N have temperature and coverage dependencies.

The scattered amplitude from the Pb film can be written in a general form of the structure factor,

$$F_{Pb}(\Theta, l) = f_{Pb}\left(\sum_{j=1}^{M} p_{w,j} e^{-q_\perp^2 \sigma_{w,j}^2/2} e^{2\pi i l D_{w,j}} + \sum_{n=2}^{N} p_n e^{-q_\perp^2 \sigma_n^2/2} \sum_{m=1}^{n} e^{2\pi i l z_m}\right), \tag{3.13a}$$

$$p_1 = \sum_{j=1}^{M} p_{w,j} \ , \tag{3.13b}$$

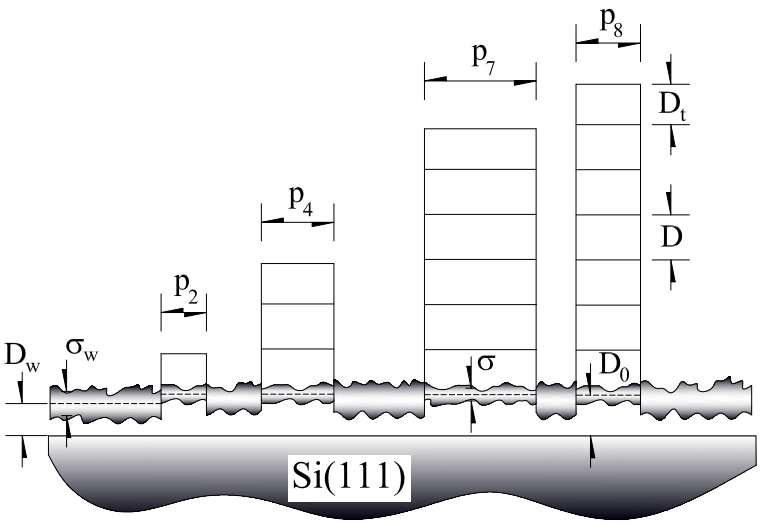

Figure 3.5: A schematic plot of Pb fcc islands grown on Si(111) substrate. For specular reflectivity, all islands n-layer thick can be represented as one island with a fractional surface coverage parameter, p_n. Note that the wetting layer sits at a height, D_w, that can be different from the island-Si spacing D_0.

$$z_m = \begin{cases} D_0 + (m-1)D & n > m \geq 1 \\ D_0 + (m-2)D + D_t & m = n \end{cases} . \tag{3.13c}$$

with f_{Pb} is the atomic factor for Pb. The first sum in Eq. (3.13a) is the amplitude scattered from the wetting layer. This term was written to allow for multiple, M, different wetting layer sites with different concentrations, $p_{w,j}$, roughness, $\sigma_{w,j}$, and positions, $D_{w,j}$ above the Si substrate. The second sum in Eq. (3.13a) is the amplitude scattered from Pb in the islands. The vertical disorder at the island-substrate interface for an n-layer island is modelled with a Debye-Waller term, σ_n, the square root of the mean deviation of the layer position. For simplicity we set $\sigma_n = \sigma$ for all islands. The $\sigma_{w,j}$ for the wetting layer are fit as free parameters.

The coordinates z_m in Eq. (3.13a) are the position of nth Pb atomic layer relative to the substrate. The Si(111)7×7 top layer (below the adatom position) is defined as $z = 0$. D_0 is the spacing between the bottom layer of an island and the substrate and D is the average layer spacing of bulk Pb in the island. To be general we have allowed the layer spacing of the top layer in the island, D_t, to be different from the bulk thickness D. This was done to account for small shifts in the top layer due to a lattice distortion. This relaxation is

the subject of much debate in the literature.[16, 39] The value of D_0 and D_t are generally different from the bulk thickness D due to the lattice distortion at the interfaces. The Pb thin film is bounded by the Si substrate at bottom and the vacuum at the top. Therefore, in principle the lattice distortions at the metal-semiconductor and metal-vacuum interfaces can be different. Since little experimental sensitivity was found to small distortions of the top layer, $D_t = D$ was used in all the subsequently fits discussed below.

To compare the data to the intensity calculated from the model structure, a fitting code was developed using the nonlinear Marquardt algorithm. The weighting method was chosen to treat the deviation of each point equally, $w_i = \frac{1}{y_i}$. At each l point, corrections such as Lorentz factor, footprint correction, effective sample area, polarization factor as well as compensating for internal momentum transfer using critical wave vectors for both the substrate and the film have been taken into account in the calculation (see Appendix I).[8] The clean Si(111) 7×7 surface reflectivity were measured before Pb deposition and fitted to determine an overall normalization factor, surface roughness and the height parameters of the reconstruction structure. These values are fixed for subsequent fits after the Pb has been deposited.

3.3.2 Experimental Results and Analysis

The specular reflectivity is measured by collecting a series of transverse scans at each q_z point along the surface specular rod. The incident angle θ_i increases symmetrically with outgoing angles θ_f along the specular rod in the scattering plane perpendicular to the surface. At each q_z point, an individual transverse scan is carried out to count the scattering intensity while rocking the sample normal within a small range. The diffraction intensity are obtained through background subtraction and in-plane integration. The specular reflectivity data represents the integrated intensity in a function of moment transfer perpendicular to the surface q_z.

Figure 3.6 shows the reflectivity and its fits after 3ML of Pb were deposited on Si(111) 7×7. While the substrate temperature was held at low temperatures of 227K, 3ML Pb were deposited with a flux rate of 1.08ML/min. The sample was immediately cooled down below

60K after deposition, and the specular reflectivity measurement was carried out afterwards. The relative high deposition flux rate and the quenching after deposition are applied so that the island distribution will not change due to coarsening. The data points were collected as the integrated intensities in a range of perpendicular moment transfer $0 < l \leq 12$, where l is in Si reciprocal lattice unit defined in Section 3.1. Based on this notation, the Bragg positions for Si(111) and Pb(111) are at $l = 3$ and $l = 3.27$, respectively. The very intense and sharp peaks at l =3 and 9 are Bragg peaks from the Si(111) substrate. The large peaks with certain widths at l =3.27, 6.47 and 9.81 are the Pb Bragg (111), (222) and (333) peaks, respectively. The small peaks between the Pb Bragg peaks are interference fringes from Pb islands of finite thickness. The scattering intensity of islands with n-layer height has $2(n-2)$ parabolic fringes between two consecutive Bragg peaks. The number of these fringes in Fig. 3.6 corresponds to a 8-layer thick Pb film though only 3ML of Pb were deposited. Therefore the Pb films is believed to take the shape of islands.

In addition to estimating the peak of the island height distribution by counting the interference fringes between Bragg peaks, the width of Pb Bragg peaks is another indicator of the island height. The higher islands result in narrower Pb Bragg peaks. The portion of reflectivity near the Pb(222) peak is shown in Fig. 3.7. It is easier to define the Pb(222) peak because of the forbidden Si(222) diffraction. The black solid line is the best fit with 8-layer islands while the blue dashed-dot and red dashed lines are for 7 and 9-layer islands, respectively. Both the Bragg peak width and the interference fringes support eight-layer islands covering the most surface area. The best fit to data gives the island height ranged from $6-10$, and peaked at $n = 8$ with a variance of 1.4-layers.

The Pb Bragg peak intensities depend on both the amount of Pb in fcc islands and the island roughness σ. The intense Pb(222)($l = 6.54$) and Pb(333)($l = 9.81$) Bragg peaks indicates the presence of well-ordered fcc stacking Pb islands, otherwise the roughness term, $e^{-q_z^2\sigma^2/2}$, will severely attenuate the constructive interference of Bragg peaks at high q_z's. As shown with the red dashed line in Fig. 3.6, Pb Bragg intensities are weaker in magnitudes with roughness $\sigma = 0.9$Å than those with $\sigma = 0.0$Å. The island roughness, σ, is found to be essentially zero to obtain the intensities at all the Pb Bragg peaks. Also the coverage

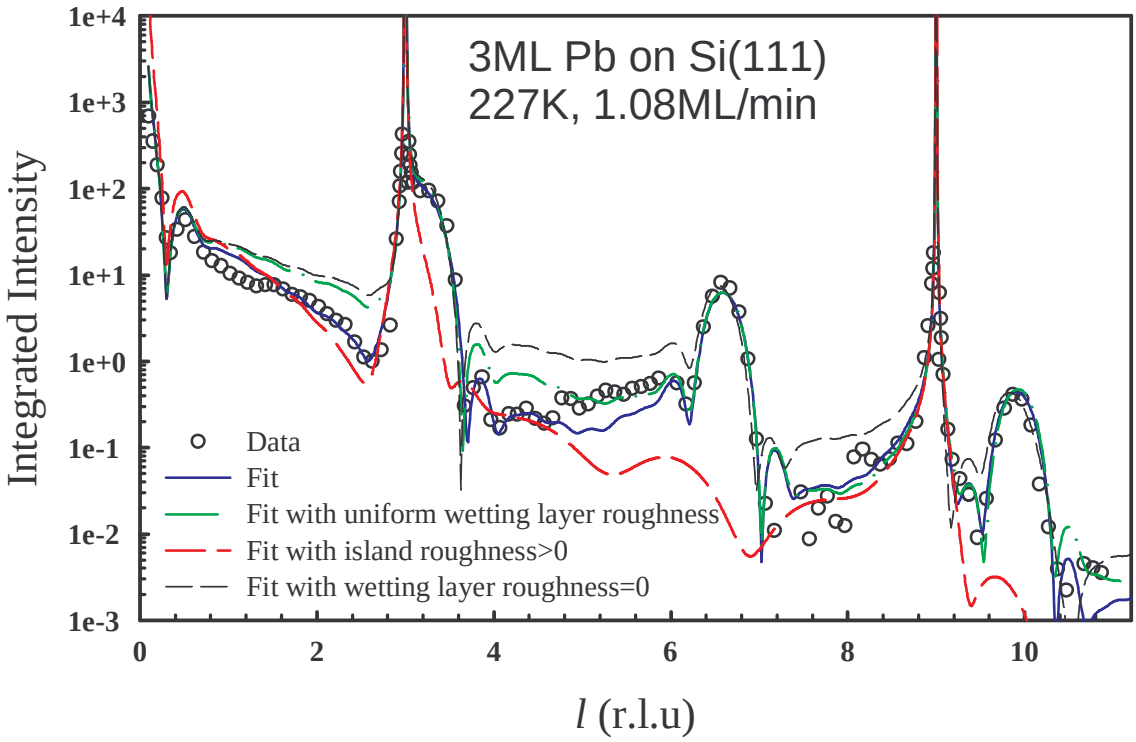

Figure 3.6: X-ray Reflectivity data of 3ML Pb on Si(111)7×7 at 227K(open circles). The intense peaks with certain widthes at $l = 3.27, 6.54$ and 9.81 are the Pb(111), (222) and (333) Bragg peaks, respectively. Blue solid line is the best fit using the model described in the text with wetting layer roughness σ_1 partially 1.02Å&0.0Å and island roughness $\sigma = 0.0$Å. Black dashed line is calculated from the same fit with $\sigma_1 = \sigma = 0.0$Å. Red dashed line is calculated from the same fit with $\sigma_1 = \sigma = 1.02$Å. Green dashed-dot line is the fit with the wetting layer uniformly rough $\sigma_1 = 0.3$Å.

in fcc islands is given at about 2.32ML, thus the one-layer wetting layer surface coverage, p_1=0.68, is determined through the total coverage constraint of Eqn.(3.12), that is, 68% of the surface is covered by the wetting layer.

The scattering of the wetting layer contributes to the background of the interference fringes. As shown with the black dashed line in Fig.3.6, the background calculated from a smooth wetting layer is much stronger than the measured data, indicating a certain level of roughness. However, it is quite hard to find an optimum wetting layer roughness σ_1 for such a long range of l. For instance, $\sigma_1 = 0.3$Å is able to fit the data well at high q's, but fails to work at low q's, as shown with the green dashed-dot line in Fig. 3.6. A better fit was achieved by allowing two different wetting layer sites; one with $\sigma_1 = 0.0$Å covering $\sim 40\%$

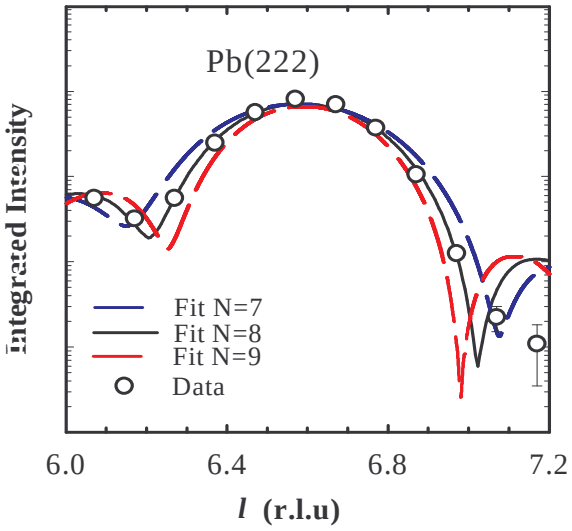

Figure 3.7: Reflectivity near to Pb(222) and fits with island height distribution peaked at 7, 8 and 9, which are blue dashed, black solid and red dashed lines, respectively.

of the wetting layer area and one with $\sigma_1 = 1.02 \pm 0.18$Å for the rest of the wetting layer.

The layer thickness parameters, D_w, D and $D0$, can also be attained from the reflectivity fits. The atomic inter-layer spacing in the film, D, is measured from the positions of the Pb Bragg peaks. The fit value for $D = 2.837 \pm 0.009$ is consistent with the bulk value. D_0 and D_w introduce phase shift term at the metal-semiconductor interface. They, therefore, produce modulations of the intensity near the Si and Pb Bragg peaks. For instance, they are responsible for the destructive dip near Si(111) peak at $\sim l = 2.6$. Islands are found to be $D_0 = 1.10 \pm 0.05$Å above the Si adatom layer and the wetting layer is found to be $D_w = 0.75 \pm 0.10$Å above the Si adatom layer. The fact that D_0 and D_w are much less than the bulk thickness represents Pb film growing on top of the Si second layer instead of the top adatom layer. In that case, the distances between the Pb film to the second Si reconstruction layer are $D_w = 2.42 \pm 0.10$Å and $D_0 = 2.73 \pm 0.10$Å. In next section, we will show in more detail the sequence of adsorption sites as the Pb atoms fill the first monolayer.

3.4 Pb-Si interface Formation during Early Growth

3.4.1 Scattering Model

One of the most interesting results of these early growth studies is how the Pb QSE islands nucleate on the highly corrugated Si(111)7×7 surface. An indication of the nucleation process is suggested in the reflectivities of the 3ML Pb films discussed in the last section. Fits to the data show that the island-substrate distance, D_0, and the substrate-wetting layer spacing, $D_{w,1}$, and $D_{w,2}$, are very different. Both $D_{w,1}$ and D_0 can be found with some accuracy from the reflectivity because they introduce a phase shift term in the scattered amplitude that is particularly pronounced near a bulk Si(111) Bragg peak. However, the 3ML reflectivities only give information about the islands-substrate structure after they have grown. The sequence of structural changes that lead to islands being farther from the surface requires measurements during the deposition of the first monolayer.

To understand the islands nucleation process, we need to be able to determine adsorption sites as the wetting layer grows or immediately after the wetting layer is complete. The early growth studies might show how a smooth island-Si interface develops on the highly corrugated Si(111)7×7 surface. Instead of measuring reflectivity or transverse scan across the Bragg point, which take too long compared to a monolayer deposition time, the Pb(111) Bragg peak at $l = 3.27$ will be followed as a function of time (these measurements are refer to as $I(\Theta)$ scans). As mentioned in Section 3.2.2, the transverse scans at Pb (111) below 1.25 ML deposition only have a single narrow peak, absence of diffuse scattering. Given sufficient detector angular acceptance allowed by the slits, the peak intensity can be measurement without any motor movement. Therefore the $I(\Theta)$ scans can be obtained quickly and are more applicable for low coverage deposition.

The reflected intensity at the Pb(111) position has a particularly simple description because it is independent of the Pb height distribution while the Pb coverage is accurately known from the calibrated evaporation source. Thus, specular intensity measurements at Bragg points as a function of coverage can be very useful to look at interfacial evolution on the atomic scale. We have calculated the reflected intensity of the epitaxy Pb film as a function of coverage in Section 3.2.1. However, in a simple model at fixed $q_z = 2\pi/d$,

we can demonstrated how the $I(\Theta)$ scans can illuminate the sequence of adsorption sites and their vertical displacement above the interface. Let $q_{||} = 0$ and $q_z = 2\pi/d$ (Pb(111) Bragg position) in Eqn.(3.3) and the total reflected amplitude is the coherent sum of the scattering from the film and the substrate,

$$\langle A \rangle = A_{Si} + A_{Pb}\langle e^{iq_z d_N} N \rangle. \tag{3.14}$$

Here A_{Si} is the Si substrate reflection amplitude that includes the 7×7 reconstruction and A_{Pb} is the scattering amplitude from a single atomic plane of Pb. The bracket indicates averaging over all possible configurations and d_N is the distance of the Pb layer from the substrate when there are N atomic planes of Pb. The N in the bracket is an approximation to the sum within the N-layer island crystal. Defining P_n as the fraction of the surface covered by n atomic planes of Pb($\sum_1^N P_n = 1$ and $\sum_1^N nP_n = \Theta$), and $e^{-iq_z d_0}\langle e^{iq_z d_N} N \rangle \equiv a_n e^{i\phi_n}$, where d_0 is a reference interfacial displacement, the total amplitude can be given as:

$$\langle A \rangle = A_{Si} + A_{Pb} e^{iq_z d_0} \sum_{n=1} nP_n a_n e^{i\phi_n}. \tag{3.15}$$

The reflected intensity $I = |\langle A \rangle|^2$ can now be conveniently expressed as,

$$I(\Theta) = I_0 |1 + \tilde{r}\tilde{\Theta}|^2, \tag{3.16}$$

where I_0 is the reflectivity without Pb, $\tilde{r} = \frac{A_{Pb}}{A_{Si}} e^{iq_z d_0}$ is a relative reflection coefficient that can be directly calculated and depends on the relative position of the adsorbed Pb atom. $\tilde{\Theta} = \Theta + \sum_{n=1} nP_n[a_n e^{i\phi_n} - 1]$ is a "complex coverage" that is equal to the known Pb coverage plus complex corrections due to displacement variations at the Pb/Si interface. What Eq. (3.16) shows is that $I(\Theta)$ is quadratic in coverage with a curvature that depends on the Pb position above the surface. As new adsorption sites are filled, with different vertical spacings, a cusp in $I(\Theta)$ will appear signalling the onset of these sites being filled.

3.4.2 Experimental Results and Discussion

Figure 3.8 show some examples of $I(\Theta)$ for various deposition fluxes at 227K. The parabolic curve is observed with 'cusps', indicating displacive transitions at the Pb/Si interface. There are two cusps in the data, a broad cusp near ∼0.2ML and a sharper cusp near ∼ 1.0ML.

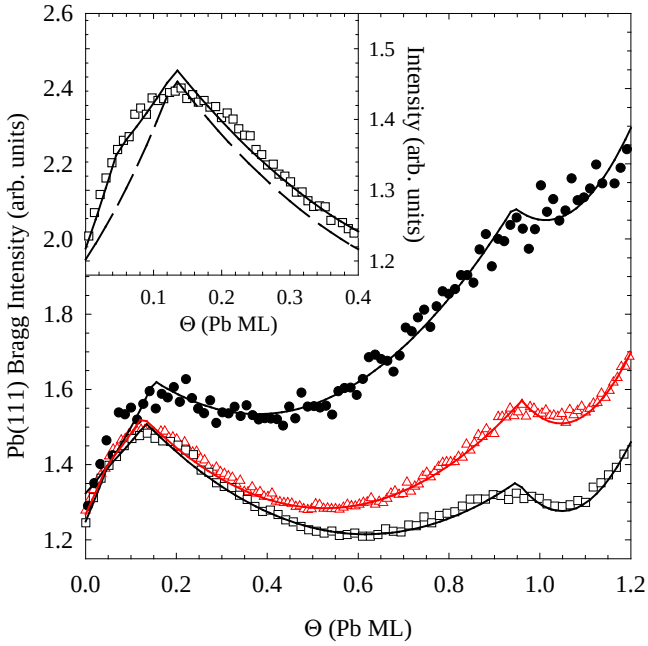

Figure 3.8: The Pb Bragg (111), $l = 3.27$, intensity versus Pb coverage for different deposition fluxes((△) 0.032ML/min, (□) 0.062ML/min, (•) 1.36ML/min). Substrate temperature is 227K. Solid lines are fits to model discussed in the text. Insert shows the low coverage intensity and a fit with (solid lines) and without (dashed lines) a 3-site wetting layer model

Remarkably good fits to the experimental intensity can be attained using Eqn.(3.16) and a simple model for $p_n(\Theta)$. With $q_z = 2\pi/d$ fixed and p_n determined by Θ, the substrate-wetting layer distance $D_{w,j}$, given j possible adsorption sites, as well as the substrate-island spacing can be determined. For simplicity these wetting layer sites are assumed to be filled sequentially as the Pb coverage is increased. STM studies at room temperature support this assumption.[44] At a critical coverage, Θ_c, Pb atoms were assumed to start filling sites on top of the wetting layer and forming n-layer islands. The solid curves in Fig. 3.8 show fits to the experimental data using this model where we assume for $\Theta < 1$ there is a single layer of Pb so that $P_1 = \Theta$ and $P_n = 0$ for $n \neq 1$. When islands form at higher coverage, they are known to be several monolayers tall, which implies that they only minimally cover the surface. Thus, for $\Theta > 1$ we assume $P_1 \sim 1$ and $\sum_{n=1} nP_n = \Theta - 1$ as well as that all islands have the same distance from the substrate, regardless of their height: $a_n e^{i\phi_n} = a_2 e^{i\phi_2}$ for $n \geq 2$. Once the phase shifts due to displacement variation are provided by the fit, we can calculate the Pb-Si distances.

The first observation is that reasonable fits to the low coverage data ($\Theta < 0.14$ML) requires three rather than the two wetting layer sites suggested by the reflectivity data. The requirement for the additional site is shown clearly in the inset of Fig. 3.8. For this data the film was grown at low fluxes to allow an adequate density of data points with reasonable counting statistics. The dashed line in the insert shows a fit with only two wetting layer sites, which fails to reproduce the rapid rise in the data for $\Theta < 0.05$ML. Thus an additional absorption site is required in the model calculation. The first available site was found to locate at $D_{w,1} = 2.16 \pm 0.04$Å with surface coverage $p_{w,1} = 0.05$. Note that the roughnesses $\sigma_{w,1} = 0.0$Å for the first site. The slope change at $\Theta \sim 0.05$ML occurs when additional Pb starts to fill the second site. The fits to the data gives the second site at $D_{w,2} = 2.34 \pm 0.04$Å with $p_{w,2} = 0.09$.

Once these two sites are essentially filled the third wetting layer site begins filling with a mean height above the surface of 2.74Å. At $\Theta \sim 0.14$ML, the increase of I with coverage ceases and I starts to decrease with coverage. This turnover means a quite different vertical spacing of a third site. The rounded curve at $\Theta \sim 0.14$ML in Fig. 3.8 might be caused by a mixture of sites being filled. The total surface coverage at the completion of the third wetting layer site is 0.96ML=0.05+0.09+0.82ML. This is the point of the high coverage cusp seen in Fig. 3.8. The roughness $\sigma_{w,3}$ for this site is very large, $\sigma_{w,3} = 0.51$Å indicating that there is a wide distribution of Pb-substrate distances for adsorption sites in the coverage range $0.14\text{ML} \lesssim \Theta \lesssim 0.82\text{ML}$. The fits to data can summarized that the available adsorption sites of the substrate are sequentially filled up to maximum coverages of $p_{w,1} = 0.05$ML, $p_{w,2} = 0.09$ML, and $p_{w,3} = 0.82 \pm .04$ML. The vertical distances above the substrate for these sites are; $D_{w,1} = 2.16 \pm 0.04$Å, $D_{w,2} = 2.34 \pm 0.04$Å, and $D_{w,3} = 2.74 \pm 0.04$Å. The vertical ordering of these sites are; $\sigma_{w,1} = 0.0$Å, $\sigma_{w,2} = 0.29$Å and $\sigma_{w,3} = 0.51$Å.

The surface coverages of the first two sites are consistent with room temperature STM studies of monolayer Pb grown on Si(111)7×7.[44] The $p_{w,1} = 0.05$ coverage (with $\sigma_{w,1} = 0$) would correspond to the three Pb atoms seen by STM to first cover the T_1 Si rest atom sites on the faulted side of the 7×7 surface (see Fig. 3.9(a)). The $p_{w,2} = 0.09$ coverage is slightly higher than would be expected to cover the three T_1 Si rest atom sites on the unfaulted side

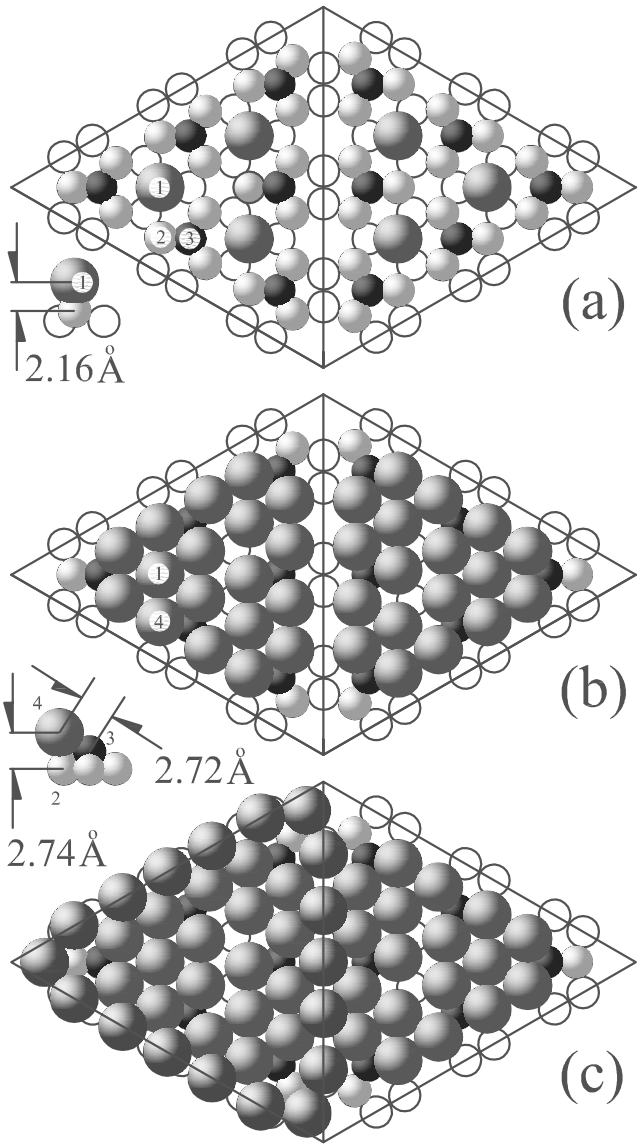

Figure 3.9: Ball models for different Pb coverages on the 7×7 unit cell. Black spheres are Si adatoms and large grey spheres are Pb atoms. Small grey spheres are top layer Si atoms and white circles are 2nd layer Si atoms. (a) 0.10ML of Pb on T_1 Si rest atom sites. Side view shows vertical spacing of Pb above the T_1 Si atom. (b) 0.61ML of Pb with 6-, 5-, and 4-fold rings filling the space between Si adatoms. Side view shows vertical spacing of Pb above the Si adatoms. (c) 0.92ML, Pb covers all sites in (b) plus sites above the Si dimers.

(5 rather than 3 Pb atoms). The slightly higher coverage of the second site compared to the expected filling of the 3 T_1 Si rest atom sites on the unfaulted side most likely reflects some disorder in the sequential filling of these sites and the $p_{w,3}$ sites that fill next. Indeed the model produces a sharper cusp in Fig. 3.8 compared to the experimental data consistent with some sites being occupied out of sequence. Also, a finite roughness, $\sigma_{w,2} = 0.29$Å, is needed to fit the data indicating that a number of sites with different vertical distances are being occupied simultaneously. A similar disorder is seen in the STM images in this coverage range.[44] Since the experiments performed here are done at a lower temperature than the STM measurements it is not surprising that some site filling disorder is observed.

Between 0.89ML and 0.98ML the Bragg intensity shows another cusp. The Pb-substrate distance of this site is 2.97 ± 0.03Å with a roughness of $\sigma = 0.0$. From previous diffuse scattering measurements we know that Pb islands begin to form once 1ML to 1.2ML of Pb is deposited.[40] Furthermore, the reflectivity data in Sec. 3.3 and the previous diffuse data show that Pb islands transform the Pb in the wetting layer below them to recrystalize into fcc sites. Because this cusp corresponds to the coverage where islands form and that the vertical order of the site is zero, this cusp could be identified as being caused by the displacive transition of wetting layer sites as they are incorporated into fcc sites in the islands. For $\Theta \gtrsim 1.1$ML, the Bragg intensity increases monotonically since the growth of *fcc* islands contributes to the the constructively Bragg scattering.

The mean displacement is $D_0 - D_{w,3} = 0.23 \pm 0.05$Å, meaning that the islands are farther from the substrate than the wetting layer. This is consistent with the 0.31 ± 0.1Å shift determined from the reflectivity results in Sec. 3.3. Note that the $I(\Theta)$ fits find that both the wetting layer and islands are ~ 0.2Å higher than those found from the reflectivity fits while the relative shifts are consistent. This difference could be caused by the lower sensitivity to the Pb-substrate spacing of the 3ML reflectivity data. Also the island-substrate distance, $D_0 = 2.97$Å, is slightly higher than the theoretical bond length, 2.86Å, for a Pb film grown on a bulk terminated Si(111) surface.[12]

These X-ray results, in particular the sequence of coverages and the displacive transition, reveals the reason why QSE effects in the Pb-Si(111) system are so strong. First, the

structure of the wetting layer is similar to that discussed by Ganz et. al.[44] but the additional vertical height information allows us to modify their original model. As in the STM model, the first three Pb atoms, are above T_1 Si rest atom sites between the Si adatoms on the faulted halve of Si(111) 7×7 unit cell, and the next three Pb atoms will fill the same sites on the unfaulted halve of the 7×7 unit cell, as shown in Fig. 3.9(a). X-ray data give the vertical spacing of Pb above the T_1 sites $D_{w,1} = 2.16 \pm 0.04$Å, much smaller than the sum of the covalent radii for Pb and Si(2.60Å)[19]. The adsorption sites on the flat substrate are on the same vertical position, therefore their roughness terms are small, consistent with the measured values $\sigma_{w,1} = 0.0$Å and $\sigma_{w,2} = 0.29$Å.

In the STM model at a maximum coverage of 0.61ML it was assumed that Si adatoms needed to be displaced to allow room for Pb atoms.[44] The X-ray data shows that the majority of atoms at 0.61ML move to 2.74Å above the surface. Using a Si adatom distance above the surface of 1.21Å[62], it is possible to arrange Pb atoms in 5-, 6- and 7- Pb atom hexagonal clusters with the bulk Pb-Pb bond distance filling the space between Si adatoms. This puts the Pb nearly equal distant from the substrate Si atoms and the Si adatoms, as shown Fig. 3.9(b). Therefore, at this coverage the seeds of fcc (111) Pb planes have been formed.

By 0.92ML (close to the measured value of 0.96ML) it is possible to fill all the cluster sites plus all the sites over the Si dimers, as shown in Fig. 3.9(c). Using a hard ball model with the bulk Pb-Pb bond length the roughness of the 0.92ML film in Fig. 3.9(c)) is calculated to be ~ 0.7Å, a bit larger than the 0.51Å measured. The data is therefore consistent with both the on-top and dimer sites being filled simultaneously as the coverage increases from 0.13ML to 0.92ML.

When and how the transition from this precursor *fcc* (111) rough film to ordered Pb islands is definitively shown in the $I(\Theta)$ scans. Once a coverage of ~ 0.96ML is reached Pb begins to grow in a second layer farther from the Si surface. Almost immediately all the Pb in the column below and containing the new second layer move up an additional 0.23Å from the substrate, indicated as the high coverage cusp in Fig. 3.8. The bonding of Pb atoms within the Pb nanocrystal are much stronger than the bonding of Pb-Si substrate,

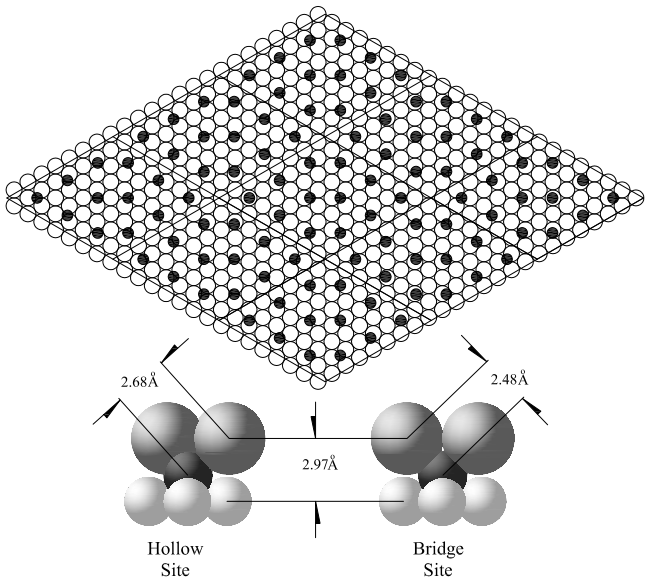

Figure 3.10: A Pb incommensurate film on the Si(111)7×7 surface. Black circles are Si adatoms and open circles are Pb atoms above the surface. The optimum hollow and bridge site Pb positions based on the experimentally determined island-substrate distance.

thus the vertical disorder of the different sites on the substrate hardly influence the vertical order of the Pb islands. This is supported by the fact that the roughness for the Pb islands formed with coverage more than 1.1ML is zero.

From the viewpoint of a structural model the transition allows a reasonably flat incommensurate Pb film to grow by "floating" above the Si adatoms. This is shown in Fig. 3.10. When the film lifts, the stronger Pb-Pb bond becomes more important than the weaker Pb-Si bond. This allows the Pb film to more easily compress to the density of a Pb(111) plane and incorporate Pb at sites above the Si dimers into the same plane. At a Pb-Si substrate spacing of 2.97Å the Pb-Si adatom bond length would be 2.68Å for the adatom in a Pb hollow site or 2.48Å for the adatom in a Pb bridge site. As Fig. 3.10 shows most Si adatoms lie in or very near either Pb hollow or bridge sites with only about 4-8% of the Pb sites directly above Si adatoms. The excess strain associated with these overlap sites could be relieved by allowing 4-8% Pb vacancies in the first layer of the Pb islands.

This sequence of structural changes explains why the Pb islands are essentially flat even though they are riding on top of a very corrugated Si(111)7×7 surface. More importantly it shows that the islands have flat tops and bottoms. It is this vertical order in the islands that

prevent incoherent electron scattering at the island-substrate boundary and allows electron standing waves to form. It is these electron standing waves that lead to new quantum states allowing QSE to be observed in the Pb- Si(111)7$\times$7 system.

CHAPTER IV

ISLAND COARSENING BEHAVIOR OF PB/SI(111) 7×7

4.1 Introduction

The nucleation, growth and coarsening of islands is described in terms of kinetics and thermodynamics [56]. When deposition results in adatom concentration that far exceed the adatom equilibrium concentration on the surface, and diffusion is slow at low temperatures, growth is controlled by irreversible kinetics such as adsorption of atoms from gas phase onto a surface and diffusion on the surface. Thermodynamics becomes important when the diffusion is very fast and equilibrium concentration is very large at high temperatures. As mentioned in previous chapters, the system of Pb crystalline islands on Si(111) exhibits a preference of island heights due to QSE. It is unclear how the preferred island heights are assembled and how the island morphology evolves with time. The preferred island heights are explained by equilibrium arguments yet the islands are known to be none-equilibrium structures that they irreversible decay to 3D domes above room temperature. Therefore kinetics must play an important role in the formation of preferred height islands.

As introduced in the first chapter, the nucleation, growth and coarsening of islands has been extensively described by a classical analysis[26, 31]. The island density n is predicted and found to scale as $n \propto (F/D)^{\chi}$, where D is the diffusion constant, F is the deposition flux and χ is a function of i, $\chi = i/(i+2)$, for a 2D growth. By measuring the flux dependence of the island density, one can determine χ and by measuring the temperature dependence, one can determine the activation energy for diffusion if χ is known. This theory only applies in very early growth and it is not well established how to interpret it in the presence of a wetting layer. We would expect it to apply for coverages just slightly above that for a completed Pb wetting layer.

Another way to study kinetics is to look at the coarsening behavior after the islands are formed and the deposition flux is turned off. In this regime, the island density slowly

begins to decrease due to coarsening (Ostwald ripening) where islands having radii larger than the critical radius r_C will slowly grow at the expense of islands having a smaller radii than r_C. This can be explained by the Gibbs-Thomson(GT) effect, which describes the variation of the adatom concentration around an island. The GT relation was shown to accurately describe the situation for 2D islands on metal surfaces.[35] Such systems have been extensively studied in 2 and 3 dimensions and are well known to lead to scaling behavior for $r_C(t)$ that evolves at long times as a power-law independent of the initial island density, n_0.[31] These scaling models give a time dependent island density as,

$$n(t) = n_0(1 + t/\tau)^{-\beta}, \tag{4.1a}$$

$$\tau \propto n_0^{-1/\beta}, \tag{4.1b}$$

where τ is the coarsening time constant and $\beta = 2/(m + 2)$ with m = 0, 1, 2, depending on the dimensionality as well as whether diffusion or attach/detachment dominates the kinetics. Note that when $t \gg \tau$, $n(t) \propto t^{-\beta}$ independent of n_0. In other words, the island density will approach the same value, given sufficiently long coarsening times.

Complementary surface X-ray diffraction techniques and STM have been used to explore the dynamics of the Pb islands on the Si(111) substrate. X-ray specular reflectivity contains information the islands height distribution and the island-substrate interface structure and thus has been measured under various growth conditions. A set of reflectivity data of 3ML Pb deposited under different conditions. An annealing affect can be seen by comparing films held at the same temperatures as the films were grown (208K - 227K) and those that are immediately quenched to 55K after deposition. In the latter case, the film is 'frozen' which allows us to measure the initial height distribution. In the former case, the film is partially annealed, providing sufficient atom mobility. This allows the islands evolve (both in height and in diameter) as a function of time. The annealing effect on the height distribution overwhelms the effects of temperature and flux within the experimental ranges.

Surface X-ray scattering and scanning-tunneling microscopy (STM) experiments have been performed on the initial formation of Pb islands grown on Si(111)-7$\times$7 to study the the nucleation and coarsening process. As will be shown from these experiments, most of

the results do not conform to current theoretical predictions, but shows an unusual flux rate dependence, a lack of scaling of the island densities evolving in time. The initial island nucleation exhibits a weak dependence on the deposition flux, as in standard nucleation theory. However a much lower island density were observed after deposition at high rather than low flux rates, contrary to the classical scaling theory of nucleation and Ostwald ripening. The coarsening time constants were found to be orders of magnitude shorter than those determined from Gibbs-Thomson driven decay previously measured on larger Pb crystals.[60, 61]

The STM observation of rapid evaporation of unstable 3-layer islands suggests the presence of another efficient decay mechanism that is related to QSE. These results indicates that the role of QSE in islands stability has a direct impact on coarsening in this system. This work shows the existence of novel and efficient pathways to self-organization that not only operate at much lower temperature but also result in sharper size distributions than those achievable through classical Ostwald ripening. These results have important implications for understanding the controlled growth and self-organization of nanostructures.

4.2 Specular Reflectivity

Figure 4.1 show a series of X-ray reflectivities and subsequent fits after 3ML of Pb were deposited on a clean Si(111)7×7 substrate under different conditions. It is known that the Pb island density evolves in time to lower densities in the temperature range of these experiments, especially when the films are grown at high flux rates.[59] The reflectivity results also reveal an additional dynamic of the Pb islands. The data (a)-(c) in Fig. 4.1 were taken with the sample held at the growth temperature during data collection. Since the collecting time for a set of reflectivity data takes $\sim$ 2hrs, these films have had time to partially anneal. On the other hand the data (d) in of Fig. 4.1 was taken after the sample was immediately quenched to 55K after deposition, freezing in the Pb morphology. Qualitatively, the quenched film has a very different reflectivity, with less defined interference fringes and a different background slope between the Pb Bragg peaks compared to the annealed films.

A quantitative comparison of the fits to the full reflectivities shows that the island height

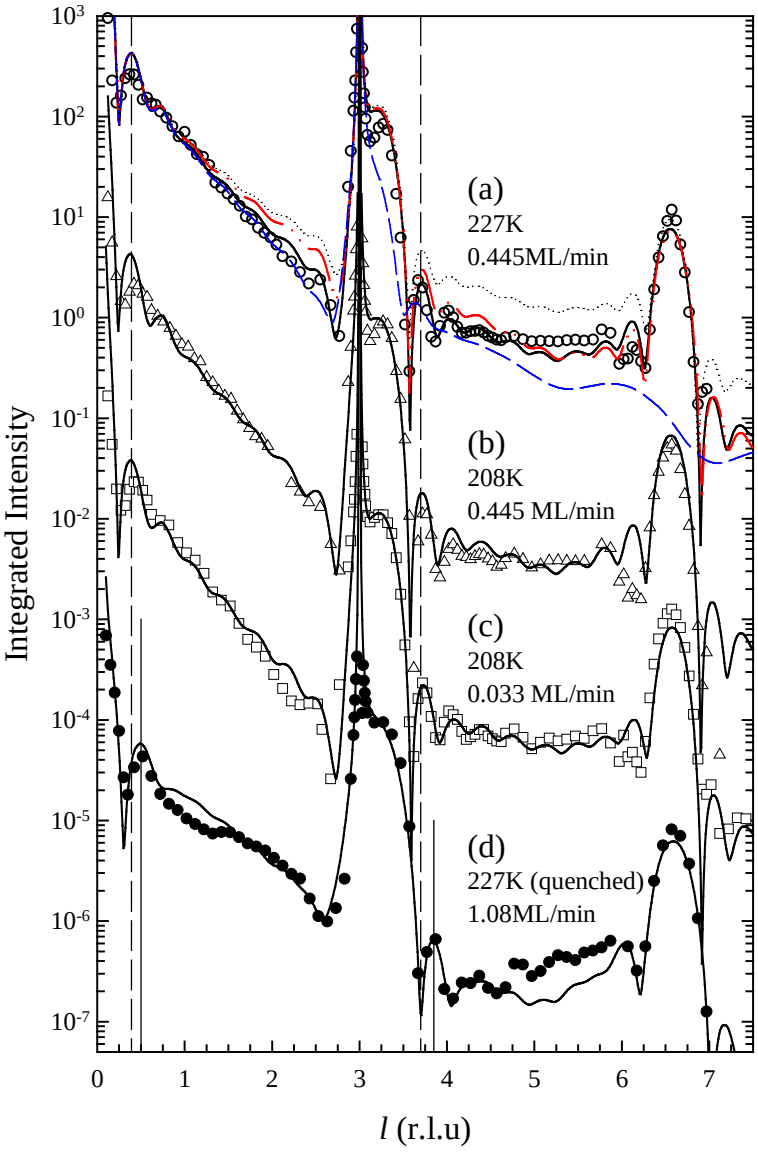

Figure 4.1: Specular reflectivities of a 3ML Pb film grow on Si(111)7×7 under different conditions as indicated. Data (a)-(c) were collected with the sample held at the same temperature as deposition. In data set(d) the sample was quenched to 55K immediately after deposition. Solid lines are best fits from the model described in the text, with two wetting layer sites: one rough $\sigma_{w,1} = 1.02$Å and one smooth $\sigma_{w,2} = 0.0$Å. In data (a) we also show fits with island roughness equal to wetting layer roughness $\sigma = \sigma_{w,1}$ (dashed line), smooth wetting layer $\sigma_{w,1} = 0$ (dotted line), and a uniformly rough wetting layer $\sigma_{w,2} = \sigma_{w,1} = 0.3$Å (dashed dot-dot line). Vertical dashed lines mark the position of two prominent interference fringes for scans (a)-(c). Solid vertical lines mark the position of two prominent interference fringes for scan (d).

distributions are different for the annealed and quenched film. This is most clearly seen by the shift to higher l of the two prominent interference fringes at $l = 0.39$ and $l = 3.70$ for the quenched film in Fig. 4.1. The island height distribution, p_n, for the reflectivities of Fig. 4.1 are plotted in Fig. 4.2. Only a single distribution from one annealed film is plotted because the distributions are almost identical within error bars. This could be because the annealing effect on the height distribution overwhelms the effects of temperature and flux within the experimental ranges. Figure 4.2 shows that the most abundant island height shifts from 8ML to 10ML as the films anneal. In other words the islands are not in equilibrium and evolve to higher dominant heights as a function of time, given sufficient atom mobility.

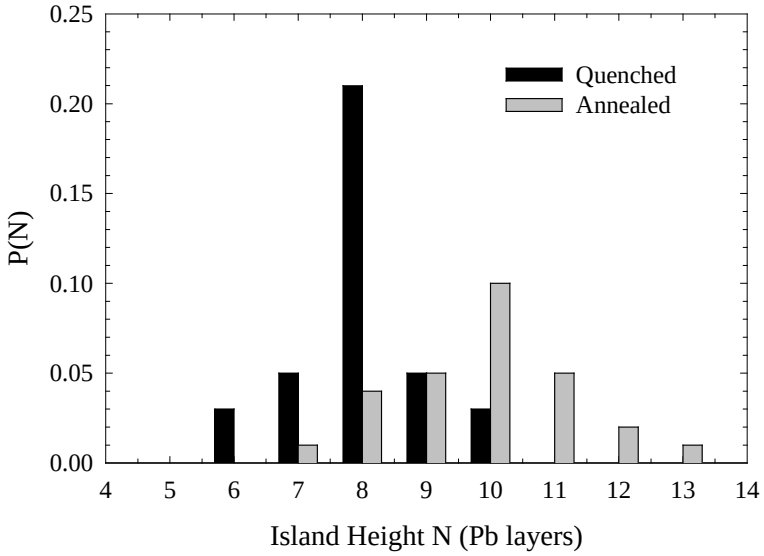

Figure 4.2: Island height histogram for two different 3ML Pb films grown at 227K. Solid bars are for a film that was quenched to 55K after deposition with a mean island height of 8ML. Grey bars are for a film held at 227K after deposition showing a mean island height of 10ML.

These structural studies reveal the morphology of the wetting layer and island-substrate interface. In previous studies it was shown that the islands grow on the Si substrate with near perfect fcc stacking ($\sigma = 0.0$Å) while the wetting layer between islands is rough.[40] This is clearly confirmed by the intense Pb(222)($l = 6.54$) Bragg peak. A finite roughness in the islands would lead to a rapid attenuation of the Bragg intensity at higher l. This is illustrated in Fig. 4.1(a). A fit to data set (a) with an island roughness equal to the wetting

layer roughness gives a very poor fit. The intense Pb(222) peaks are present in all reflectivity data sets in Fig. 4.1, thus the formation of well stacking *fcc* islands is reproducible.

In all the fits in shown Fig. 4.1, reasonable fits were obtained only if the structure of the wetting layer was considered properly (i.e a two component wetting layer as discussed in the previous chapter). Because reflectivities takes so long to acquire, they are not suitable for kinetics measurements. To follow the evolution of island formation we have studied the time dependence of the the diffuse Pb scattering that is associated with island size, density and height distribution.

4.3 Diffuse X-ray Scattering

In this work, island densities were determined by measuring the splitting of the diffuse lobes around the Pb(111) Bragg points. Assume a uniform distribution of island separations in all directions, the diffraction structure is a round ring centered at the Bragg point (Henzler rings).[15, 42] The radius of this ring structure is related to a characteristic length of the island separation. The splitting in reciprocal space, $\triangle\kappa$, is proportional to the mean island separation L, which gives the island number density $n \sim 1/L^2 \sim (\triangle\kappa/2\pi)^2$.

The temperature dependence of the initial island densities was first explored using a point detector to measure the difuse lobes. Figure 4.3 shows the data obtained from X-ray diffuse scattering experiments taken after the deposition of 1.2ML of Pb at flux 0.404ML/min for various temperatures. The substrate temperatures were in the range of $193K \leq T \leq 227K$. The Pb coverage was chosen to be 1.2 ML, the critical coverage at which Pb islands start to form. The data demonstrates that initial island density follows an Arrhenius law, $n \propto e^{\chi E/k_B T}$. This result is consistent with the prediction of nucleation theory. The energy term $-\chi E$ can be determined from the slope in Fig. 4.3, which was found to be at about 0.296 ± 0.019 eV. Both binding energy and diffusion barrier energy contribute to this energy term. Once the critical cluster size i and the binding energy are known, we can calculate the diffusion barrier. The standard way of measuring χ, and simultaneously make a real test for the applicability of classical theory, is to measure the flux dependence of the initial island density at fixed temperature. The classical theory expects

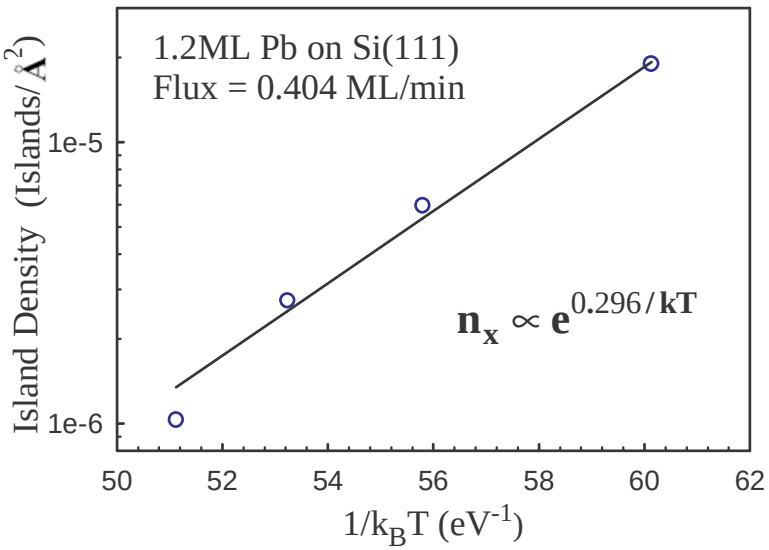

Figure 4.3: Island densities versus temperature for 1.2ML Pb on Si(111). It demonstrates the exponential dependence on substrate temperature T. These data were obtained from X-ray diffuse scattering measured after the deposition of 1.2 ML of Pb for various temperature at deposition flux 0.404 ML/min. The solid line is a exponential fit with energy barrier of 0.316 eV.

a power law relation $n \propto F^{\chi}$.

Figure 4.4 presents the time evolution of the island density obtained from diffuse X-ray scattering after 1.2 ML of Pb was deposited on the Si(111)7×7 surface for different flux rates with substrate temperature at 208K. Islands coarsening was observed in these experiments and shows that the Pb island densities shrinks with time. The deposition flux was in the range of 0.032ML/min to 0.467ML/min. A factor of two increment of the flux rates was chosen so that the data points are near equally spaced in logarithm scale to describe a power flux dependence of the island density, as predicted by the nucleation theory. After each deposition, the system was maintained at the same substrate temperature, with X-rays transverse scans across Pb(111) point taken for $\sim$ 3 hours. The positions of the Pb(111) peak and the lobe peaks were determined by a least-square fit with three Lorentzians lineshapes. These fits also give the peak widths and integrated intensities. The lobe structure in those transverse scans kept on shifting towards the Bragg peak and eventually merged with them, indicating an expanding of the coherent length on the surface. The island densities were calculated using the above method. The resulted island densities were observed to decrease

monotonically with time for all flux rates, as illustrated in Fig. 4.4(a). The time interval between each point is about 9 minutes which is the data collecting time using point detector.

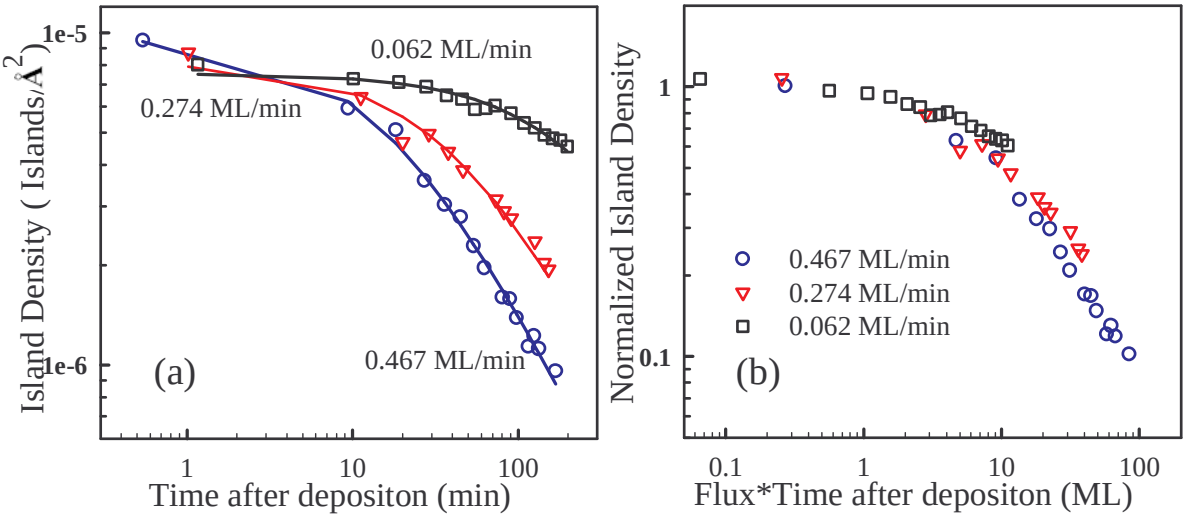

Figure 4.4: (a) Island densities vs time after deposition. The time evolution of the island density were obtained from X-ray diffuse scattering measured after the deposition of 1.2 ML of Pb at 208 K for various deposition fluxes F. The solid curves are fits using Eqn.(4.1a) with $\beta = 1$. It demonstrates the breakdown of the Ostwald ripening scaling: The curves do not approach each other at long times. (b) Normalized island density n/n_0 versus time scaled by flux. The curves tend to overlap, implying that n_0 is independent of the decay time, and the decay time is inversely proportional to the flux.

While the Arrhenius behavior is indicative of classical nucleation, the flux dependence of the initial island density shows the first problem of applying standard nucleations models to this QSE system. This data is obtained by fitting the coarsening scans. The decay of island density can be described by fitting to Eqn.(4.1a). These fits allow us to measure both the coarsening time τ, the initial island density, n_o and the exponent β. The coarsening data is shown in Fig. 4.4(a) along with their fits. Acceptable fits can be obtained for an exponent in the range of $1 \geq \beta \geq 0.7$. Fixing β for any value in this range does not change the subsequent trends in n_o or τ with flux, although they will change an overall scale factor. The initial island density derived from these fits is shown as a function of flux rate in Fig. 4.6(b). The data indicates a very weak fractional power dependence on flux rate. The solid curve shows a weak power law fit of n_0 on flux, $n_0 \propto F^{0.16\pm0.06}$. The

exponent is about 0.16, much less than the minimum value predicted by the nucleation theory (minimum $\chi = 0.33$ for a critical cluster size $i = 1$).

In addition to the weak flux scaling of the initial island density, Fig. 4.4(a) shows an even more problematic trend in the non-classical behavior of this system. The deposition flux is found to play an important role in the behavior of island coarsening. Islands formed at faster deposition rates tend to coarsen faster. The number of islands per unit area decreases almost by a factor of 10 for a deposition rate of 0.467ML/min in 3 hours while it only decreases by about a factor of 1.5 for a rate of 0.062ML/min for the same amount of time. According to standard scaling predictions for Ostwald ripening, all the curves in Fig. 4.4(a) should, at long times, approach together with a common time constant. The simulated values of island density for Ostwald ripening are shown as a function of time in Fig. 4.5. We can see that the two curve with a high and a low initial island density approach each other at long times.

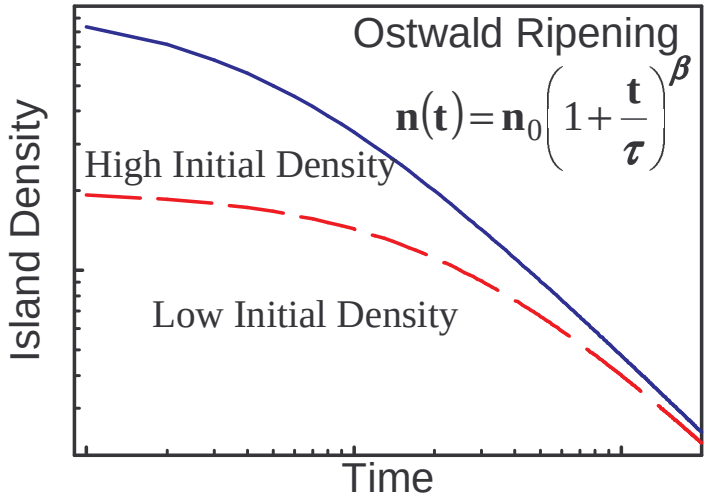

Figure 4.5: Simulated values of island density for coarsening (Ostwald ripening) versus time. The solid curve is for a high initial density and the dashed curve is for a low initial density.

In fact, when we normalize island density by dividing it by each initial density n_0, given by the fit using Eqn.(4.3), and plot versus equivalent monolayer time (product of time and flux), we find that all the data collapse to a single curve (shown in Fig. 4.4(b). This indicates that the coarsening is flux dependent. In other words the islands coarsen in a manner that

depends on how they were grown!

This is demonstrated more clearly if we plot the coarsening time constant τ, derived from fits with $\beta = 1$, as a function of flux rate. This is shown in Fig. 4.6(a). The coarsening time is found to vary nearly inversely with flux ($\tau \propto F^{-0.98\pm0.10}$). In fact, there is no trend indicating that τ depends at all on the initial island density as predicted by standard coarsening models (see the relation of Eq. 4.1b). Both the lack of scaling and the $1/F$ dependence of τ are very robust, persisting to coverages up to 3 ML and over the entire temperature range where Pb islands form. Note that, while coarsening might be occurring during growth, standard coarsening models do not depend upon how an initial island density is established. In these experiments, it is clearly important how the initial density is produced, and this marks the breakdown of the standard models in this system.

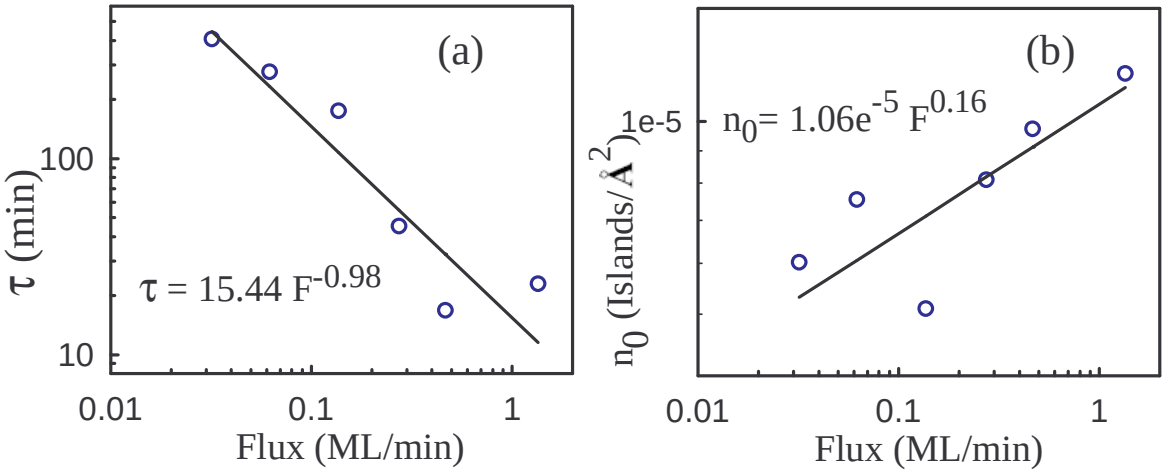

Figure 4.6: (a) Coarsening time constant versus flux rate. The time constant changes quickly with flux $\tau \propto F^{-0.98\pm0.10}$, showing that islands formed with faster deposition tend to coarsen faster. (b) Initial island density n_0 versus flux rate, indicating that n_0 depends only weakly on flux $n_0 \propto F^{0.16\pm0.06}$.

The experimental data discussed above were collected using a point detector. The collecting time ($\sim$ 9 minutes for one transverse rod scan) makes it hard to probe the kinetics of this system at early times since the decay time constants can be on the order of a minute. It is possible that the initial island densities obtained by a CCD are different from those by a point detector because the latter actually measures island density over a long data collection time. To check for this possibility, we used the CCD detector which

reduces the collection time from 9 minutes to 10 seconds. This allows us to confirm the point detector results an order of magnitude closer to the time when the deposition shutter is closed.

The experimental setup and data analysis of the CCD detector have been introduced in chapter two. The absolute quantities of the measurements might be slightly different from those of the point detector, but they should show the same time evolution trend of the island density. Figure 4.7 presents the island density, obtained from diffuse X-ray scattering collected using a CCD, as a function of time after 1.2 ML of Pb was deposited on the Si(111) surface for different flux rates at 227K. The time interval between each point is 10 seconds. Note that the temperature is 19 degrees higher than the previous experiments. Because the exposure time of the CCD is limited to avoid pixel saturation at Bragg reflection, the data statistics of the diffuse ring is limited as well. The lobe structure is better defined for a higher temperature so that we can determine island densities earlier.

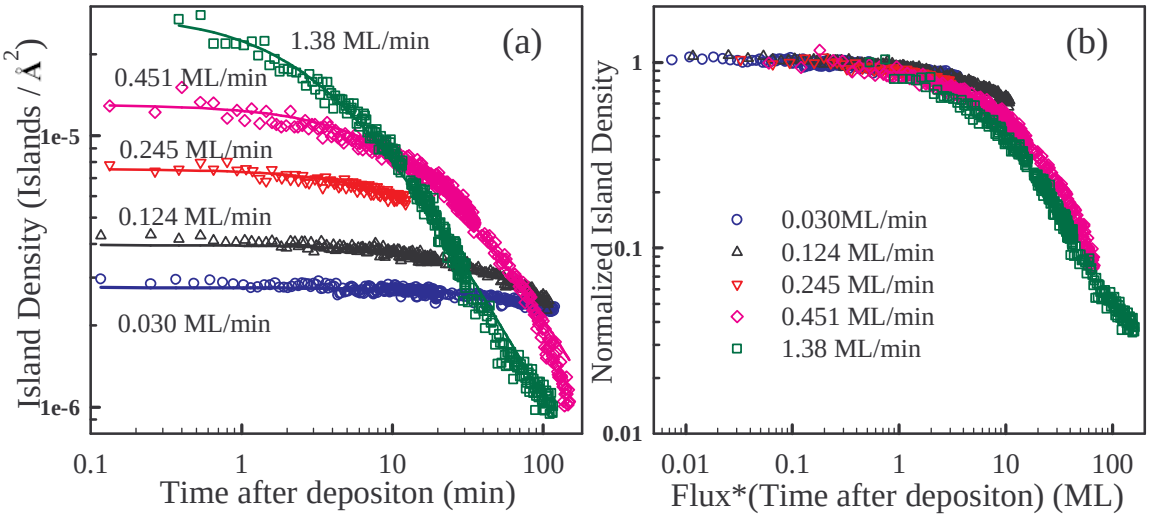

Figure 4.7: (a) Island densities versus time after deposition. These data are collected by a CCD detector after the deposition of 1.2 ML of Pb at 227 K for various deposition fluxes F. The solid curves are a fit using Eqn.(4.1a) with $\beta = 1$. (b) Normalized island density n/n_0 versus time scaled by flux. The curves tend to overlap, implying that n_0 is independent of the decay time, and the decay time is inversely proportional to the flux.

The data shown in Fig. 4.7(a) demonstrates the same time evolution features as those in Fig. 4.4. Faster deposition nucleate more islands, but these islands coarsen faster after

deposition. Note that this implies that given sufficient coarsening time, a much lower island density can be achieved through fast deposition. Very much the opposite of standard nucleation models. For instance, we can see from Fig. 4.7 that at 100 minutes after deposition, $n \sim 1.2e^{-6}/\text{Å}^2$ with $n_0 \sim 2.2e^{-5}/\text{Å}^2$ for the high flux 1.38 ML/min while $n \sim 2.1e^{-6}/\text{Å}^2$ with $n_0 \sim 2.9e^{-6}/\text{Å}^2$ for the low flux 0.0297 ML/min.

The CCD data have also been fitted using Eqn.(4.1a) to a given coarsening time constant and initial island density. Again, the coarsening time is found to vary strongly on flux so that all curves in Fig. 4.7(a) collapse to a single curve when the time axis is multiplied by the deposition flux (Fig. 4.7(b)). The coarsening time constant from the CCD data are shown as a function of the flux rate in Fig. 4.8(a). The solid curve is its power law fit of τ on flux, $\tau \propto F^{-1.14\pm0.12}$. The strong dependence of coarsening time on flux is reproducible within our temperature and coverage domain.

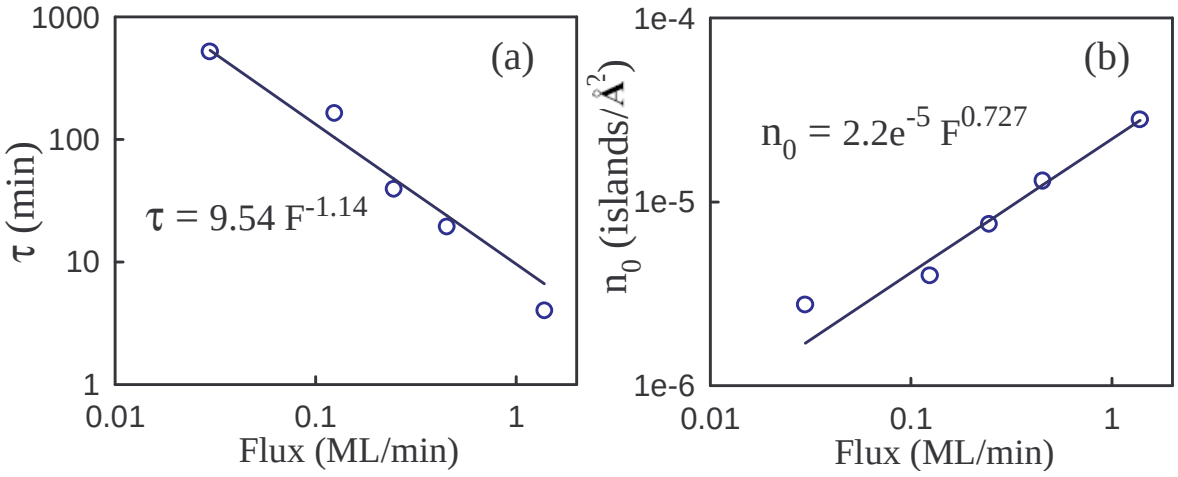

Figure 4.8: (a) Coarsening time constant versus flux rate. These data are collected by a CCD detector after the deposition of 1.2 ML of Pb at 227 K for various deposition fluxes F. The time constant vary strongly with flux $\tau \propto F^{-1.14}$, showing that islands formed with faster deposition tend to coarsen faster. (b) Initial island density n_0 versus flux rate, indicating that n_0 has a power law dependence on flux.

One difference in the CCD is that the initial island densities have a more classical flux dependence as shown in Fig. 4.8(b). The solid curve is its power law fit of n_0 on flux, $n_0 \propto F^{0.73\pm0.07}$. This may be because of the higher temperature of these experiments. Also because of the quick coarsening at high fluxes ($\tau \sim$ 5mins for flux 1.38ML/min at coverage

1.2ML), it requires the experiments be carried out as soon as possible after deposition with a short data collecting time. The fact that our scattering experiments were performed *in situ* and equipped with the intense synchrotron X-ray source and a CCD detector, makes it possible for us to find the flux dependence and extraordinary coarsening features in the Pb-Si system.

The novelty of the coarsening in this system is also manifested in the magnitude of the coarsening times that can be compared to those determined from Gibbs-Thomson driven decay previously measured on larger Pb crystals.[60, 61] In those studies, the rate of decay of an island having radius r positioned on a much larger circular terrace of radius was well described by: [57, 58]

$$\frac{dr}{dt} = \frac{-D_s\lambda_\beta}{r\ln(\rho/r)}(\frac{1}{r} - \frac{1}{\rho}), \tag{4.2}$$

where $D_s\lambda_\beta$ defines the detachment barrier of an atom from the island perimeter, and $D_s\lambda_\beta = (7 \times 10^{13}/kT) \times e^{-0.86\mathrm{eV}/kT}$ eVnm^3/sec.[57] In the limit of terrace radius much larger than the size of an island on the terrace, $\rho \gg r$, the decay rate of the island becomes $1/\tau \sim 3\pi^{3/2}D_s\lambda_\beta(n_0h/\theta)^{3/2}$, where θ/n_0h is the mean island area of n_0 islands per unit area at coverage θ with number of layers h. The decay time constant is given as $\tau \sim 10^6$ sec while our observed time constants are in the range of $10^2 - 10^3$ seconds, shown in Fig. 4.8. The island decay driven by Gibbs-Thomson effect therefore has a rate $10^2 - 10^3$ times slower than observed in these experiments.

Besides the flux rate, temperature and the Pb coverage are also important factors affecting when the islands start to form and how fast they coarsen. By continuing data collection during deposition, we were able to tell at which coverage the diffuse lobes show up, i.e. when islands start to form. These coverages were found to vary with temperature. At lower temperatures, islands emerge at higher coverages. These critical coverages have been roughly estimated to be $\sim$ 1.2 ML at 227 K, $\sim$ 1.6 ML for 208K and $\sim$ 2.0 ML for 198K. The effect of each factor on the decay time can be found by fixing one or two factors and varying the others.

To figure out the effect of coverage on the decay time, we fixed the temperature at 227K and took data at two deposition coverages: 1.2 ML and 2.0 ML. The obtained coarsening

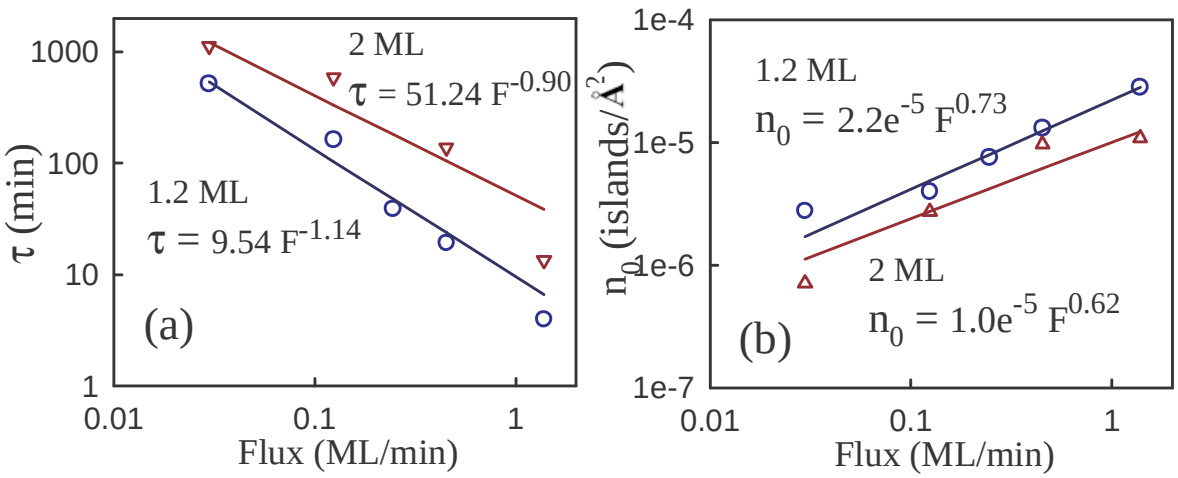

Figure 4.9: ((a) Island coarsening time versus flux rate at two coverages: 1.2ML and 2.0ML. The substrate temperature was maintained at 227K. The power law dependence on flux are given. (b) Initial island density versus flux rate for the two coverages.

time constants and the initial island density are shown in Fig. 4.9(a) and (b), respectively. We can see that τ is larger at 2ML than at 1.2ML for each flux measured.

The effect of temperature on the coarsening time was also explored by fixing the coverage at 2ML and taking data at two temperatures: 198K and 227K. The measured τ and n_0 are plotted versus $1/k_BT$ in Fig. 4.10(a) and (b), respectively. Even though we only have two temperature points to compare with, it is evident that at each flux n_0 is smaller at higher temperatures, as shown in Fig. 4.10(b). As was shown earlier in Fig. 4.3, the temperature dependence of n_0 in Fig. 4.3 follows the expected nucleation result independent of flux. In the standard Ostwald ripening, $\tau \propto n_0^{-1/\beta}$ shows that τ should be larger at smaller n_0, i.e. higher temperatures. We can see from Fig. 4.10(a) that this trend is true except for one flux rate, 1.38 ML/min, at which the two τ's are about the same within error bar. However, the scaling with n_o is still not sufficient to make the long time behavior of the coarsening data consistent with Ostwald ripening theory. This means that the temperature dependence must be more complicated than the simple scaling predicts.

Why does this system coarsen so fast and what is the origin of the flux dependence? Insight into the reason for the breakdown of the Gibbs- Thomson effect and the fast decay time is obtained by looking at the specific heights of the islands from STM experiments

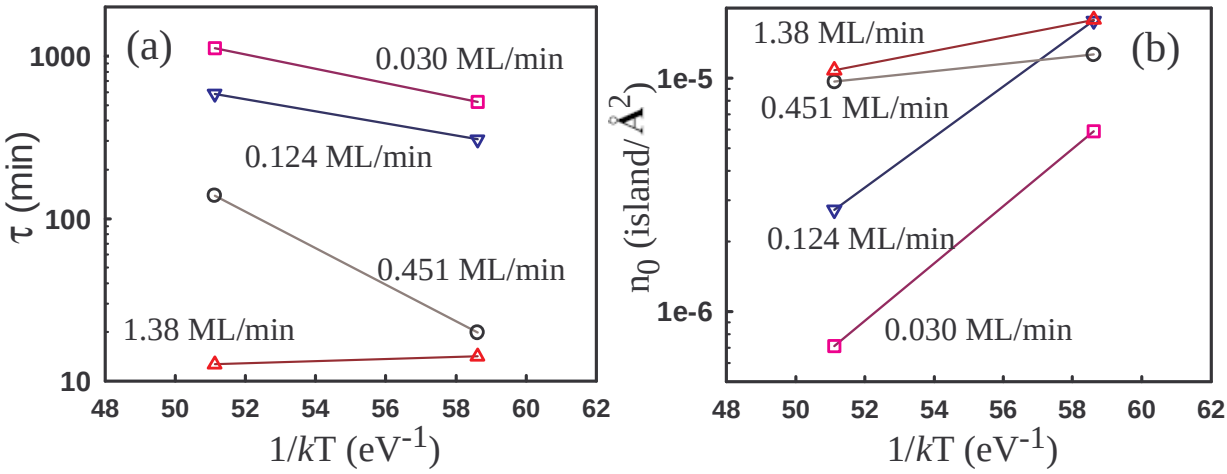

Figure 4.10: (a) Coarsening time versus $1/k_BT$ at different flux rates. The Pb coverage is 2ML. (b) Initial island density versus $1/k_BT$ at different flux rates.

performed under similar growth conditions.

4.4 STM Results

The scanning tunnelling microscopy (STM) is widely used to characterize surface topography at the atomic scale. The STM falls in the category of direct space surface probing techniques. Unlike reciprocal space probes measuring the Fourier transform of the atom correlation function, STM provides a three-dimensional profile of the atom arrangement of a surface by scanning an conducting tip over a surface to detect the weak electric current flow between the tip and the surface.[51] It measures a real space image of the distribution of atoms, or the electron distribution around the atom. The STM has a remarkable spatial resolution at the atomic scale to resolve individual atoms. The scan region of a STM image is generally in a size of microns.

The STM experiments were carried out in a variable temperature Omicron STM at Ames Lab by Professor Tringidis. The Pb deposition was calibrated based on determining the optimal coverage for the dense Pb-α-$\sqrt{3}\times\sqrt{3}$ phase (i.e., 4/3 ML). Figure 4.11 shows a series of images as a function of time after depositing 1.6ML Pb at 206 K at a high flux rate (0.5 ML/ min). After 74 min, the overall island density decreases by a factor of 2.5. Note, however, that the initial island density is comprised of islands having a range of heights.

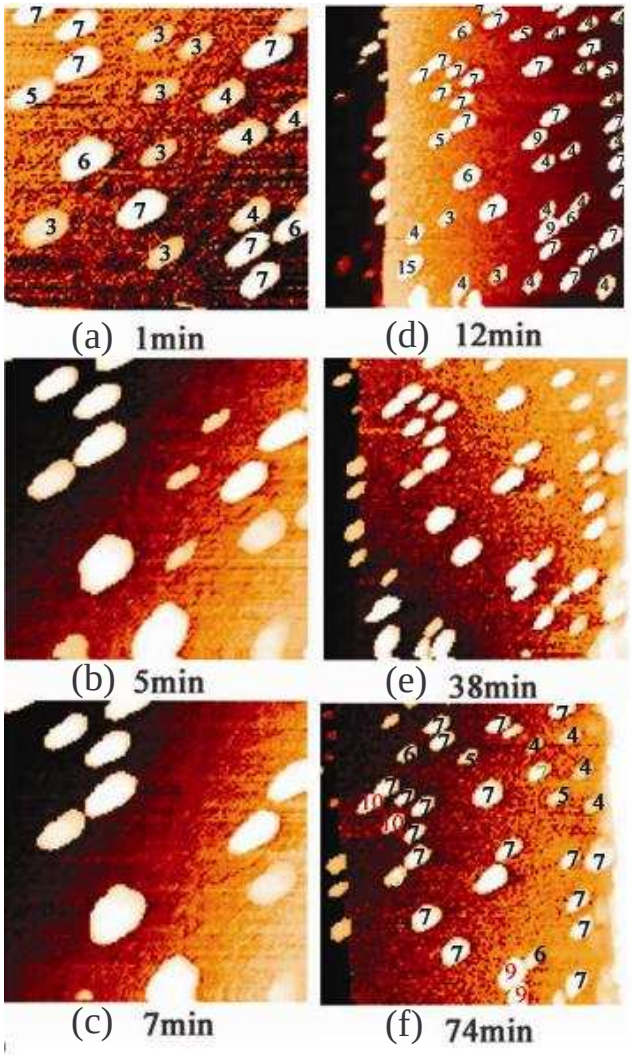

Figure 4.11: STM images of the coarsening of 1.6 ML Pb deposited on Si(111) 7×7at 203 K at a flux of 0.5ML/min. The times after deposition are shown for each image. The scale is $250 \times 250\text{nm}^2$ for (a) and $500 \times 500\text{nm}^2$ for (d). The tunnelling parameters were 2V at 1 nA. Each scan takes 0.5 min. The island height is marked on top of each island for image (a), (d), and (f) (height is measured with respect to the Pb wetting layer.) It can be seen that 3-layer islands are less stable than 4-layer ones and both of these are less stable than 7-layer islands.

The islands height is measured with respect to the Pb wetting layer and is marked on top of each island for Fig. 4.11(a),(d) and (f). Following the group of islands arranged in a crescent shape at the top left of the images, it is clear that the island heights evolve towards the superstable 7-layer islands[4, 40]. The 3-layer islands disappear extremely fast; the remaining 3-layer islands in Fig. 4.11(b) disappear in less than 2 min. These islands have approximately 1000 atoms in $\sim 7.0 \pm 0.4$ nm diameter. According to Eqn.(4.2), should decay $\sim 10^4$ times slower than observed. Clearly, atoms detach from these islands and diffuse until they are incorporated into the surrounding 7-layer islands. The majority of the 4-layer islands also disappear (some transform into higher height islands) but over a longer time scale compared to the 3-layer island decay time.

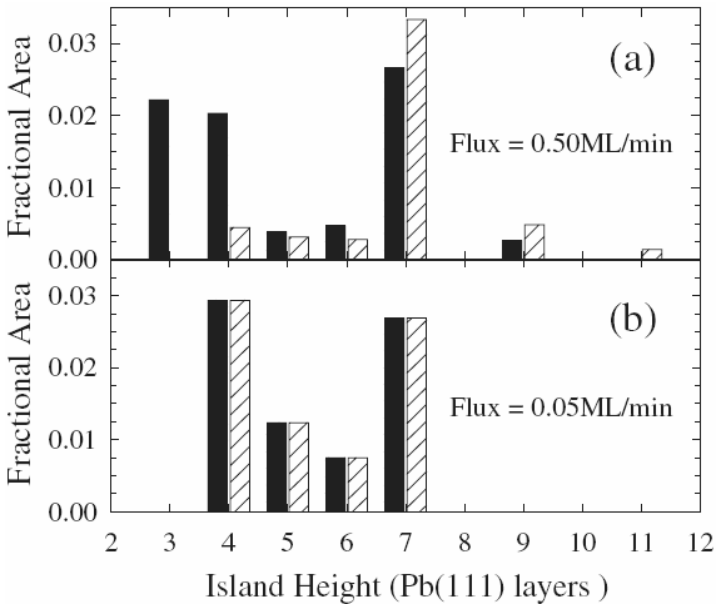

Figure 4.12: Histograms of the island height distribution for 1.6 ML grown at 203 K, measured 5 min after (black) and 74 min after deposition (cross-hatched). (a) shows a high flux rate deposition, 0.5ML/min, leading to a broad initial island height distribution with fast decay of unstable islands. (b) shows a low flux deposition, 0.05ML/min, leading to a narrower initial island height distribution with little change over time.

To be more quantitative, the height histograms of Pb islands has been measured before and after coarsening for both low and high flux rates at 206 K. Figure 4.12(a) shows the height histogram for a 1.6 ML film grown at $F = 0.5$ ML/min, both 5 min after deposition and 74 min later. The initial surface exhibits a relatively broad distribution of island heights,

which remarkably evolve to a single dominant population at 7 layers. [25] Populations having heights less than 7 layers decrease significantly after coarsening, especially the 3- and 4-layer islands. In contrast, the same amount deposited at a lower flux rate (0.05 ML/min), shown in Fig. 4.12(b), exhibits a relatively narrower initial height distribution. Within measurement statistics, this distribution remains unchanged even after 80 min. Note that the island density for the film in Fig. 4.12(b) remains essentially constant during the 80 min coarsening experiment.

The STM has been used to show that QSE plays an important role in the height stability of Pb islands in the system[4]. This STM results further prove that QSE has an impact on the kinetics of Pb islands nucleated on the substrate. The STM images shown in Fig. 4.11 and the data in Fig. 4.11 are consistent with the observed X-ray result that low flux islands coarsen slower. The decay of island densities in Fig. 4.7 and height histogram in 4.12 demonstrate that growth at high flux rates ultimately leads to a sharper monodispersed height distribution as well as a lower density, in stark contrast to the usual situation in epitaxial growth.

More importantly, the STM hints at a way to explain the x-ray coarsening data. In the next section we conjecture a model that predicts a number of the experimental trends based on stable and unstable height islands.

4.5 Discussions

The STM data shows that 3-layer islands are unstable. These islands have approximately 1000 atoms in $\sim 7.0 \pm 0.4$ nm diameter, far beyond the critical cluster size. This quasi-stable condition arises from QSE and should be included in the rate equation approach. In a simple extension of the nucleation rate equations 1.5 -1.7 two types of islands, stable islands N_{x2} and quasi stable islands N_{x1}. Note that the quasi-stable islands here are different from the so-called metastable islands smaller than the critical cluster size. The latter decays very fast. We assume, based on the STM data, that the quasi-stable islands nucleate according to standard models but decay at a slow rate. In addition they also transform into new stable islands. This transformation can proceed by a number of mechanism. For our case

we have chosen that material climbs up to the top of the quasi-stable islands and nucleates a second layer. This new two-layer island is more stable than the one-layer islands due to QSE. Note that the restriction to one-layer and two-layer islands is arbitrary. The only requirement for the model is that one type of islands is more stable compared to the other. The kinetic equations can be developed from Eqn.(1.5-1.7):

$$\frac{dN_1}{dt} = R - DN_1(\sigma_{x1}N_{x1} + \sigma_{x1}N_{x1}) - \frac{N_{x1}w_1}{\tau_o}, \tag{4.3}$$

$$\frac{dN_{x1}}{dt} = \gamma_i D N_1^{i+1} - \frac{N_{x1}}{\tau_C} - \frac{N_{x1}}{\tau_o} \tag{4.4}$$

$$\frac{dN_{x2}}{dt} = \frac{N_{x1}}{\tau_C}. \tag{4.5}$$

As before N_1 is the monomer density, i is the critical cluster size, R is the flux, D is the diffusion constant, σ is a capture cross section, w_1 is the average number of atoms in the quasi-stable islands N_{x1}. The total island density is $N_x = N_{x1} + N_{x2}$. The time constant for decay of an unstable islands is τ_o and τ_C is the time to convert N_{x1} islands into N_{x2} islands. The second term in Eq. 4.3 is the capture of monomers by all islands. The last term is a source of monomers from the decaying unstable islands. The first term in Eqn.(4.4) describes the increase of N_{x1} due to nucleation, and $\gamma_i = \sigma_i C_i N_0^{i+1} e^{E_i/kT}$, where E_i is the binding energy of a cluster, N_0 is the number of available sites on the surface and C_i is a geometric constant.

The equilibrium island density beyond the transient nucleation stage can be estimated by assuming steady state conditions, i.e, $dN_1/dt = 0$ (this is a very good approximation as determined by numerical results). If we further assume that nucleation of N_{x2} is slow, ie. τ_C large or $N_{x2} \ll N_{x1}$, then Eqn.(4.4) can be solved for the equilibrium monomer density,

$$N_1 = (R + \frac{w_1 N_{x1}}{\tau_o})/D\sigma_{x1}N_{x1}. \tag{4.6}$$

For early growth, we can meke two valid assumptions; τ_c is large and N_{x2} is small. In other words during few stable islands exist until a sufficiently long time has passed before unstable islands have a chance to transform into stable islands. Substituting Eqn.(4.6) into Eqn.(4.4) and assuming that the last two terms in Eqn.(4.4) are small (this assumption is

valid as long as τ_c is large or N_{x2} is small), we can solve the differential equation for N_{x1} in the limit $N_{x1}w_1 < R\tau_0$:

$$\frac{N_{x1}(t)}{N_{x2}(t)} \approx \frac{(i+2)\gamma_i}{\sigma^{i+1}D^i}^{1/(i+2)}. \tag{4.7}$$

Since the time to deposit a coverage Θ is $t = \Theta * \Omega/R$, where Ω is Pb(111) the surface density (1.0ML=1.89×10^{15} atoms/cm^2), N_{x1} can be written as a function of time, $N_{x1}(t) \propto t^{1/i+2}$. Substituting Eq. 4.7 into Eqn.4.5, we get the ratio of N_{x1}/N_{x2}, which is proportional to the flux,

$$\frac{N_{x1}(t)}{N_{x2}(t)} \approx \frac{(i+2)\tau_C R}{(i+3)\Theta\Omega}. \tag{4.8}$$

This ratio derived from the new rate equations (4.3)-(4.5) is approximately proportional to flux under the assumptions of early growth. Although more quasi-stable islands are nucleated at a high deposition rate, the ratio shown in Eqn.(4.8) tells us that less stable islands can be converted from the quasi-stable islands during growth, given a constant τ_C. Once the deposition is shut off $R \to 0$, the single atom density N_1 drops dramatically and the nucleation process ceases, most of the existing quasi-stable islands will decay over time, $N_{x1} \to 0$, and very little of them will convert to stable islands. Meanwhile N_{x2} will maintain almost the same value because $dN_{x2}/dt = N_{x1}/\tau_C \to 0$. As a result, after coarsening a long time, only the stable islands N_{x2} remain in the system, and the total number of them are less for a high flux deposition.

If we make the assumption that the coarsening time is related to the ratio of stable to unstable islands, i.e . $1/\tau \approx \frac{N_{x1}(t)}{N_{x2}(t)}$, then much of the coarsening behavior can be explained. The coarsening time is faster at high flux simply because the time to deposit a fixed amount of Pb is short compared to low fluxes. This means that at high fluxes there are fewer stable islands present at the end of deposition. Once the flux is turned off, the unstable islands rapidly decay leaving behind a small number of stable islands. Likewise this model predicts that the coarsening time for islands deposited at higher coverages will be longer because it takes more time to deposit the Pb. This gives the system more time to convert unstable islands to stable islands.

The experiments described above suggest the following picture for the growth of QSE nanocrystals. The initial island nucleation exhibits a power-law dependence on the deposition flux, as in standard nucleation theory. The types of islands that are produced, however, depend strongly on the flux rate. High flux rates generate a broader range of island heights that have a broader range of stability. This could be presumably because of the larger adatom concentration that drives a higher chemical potential. Thus, many of the islands are unstable and decay once the deposition flux is turned off. This quickly leads to a significantly lower island density. Conversely, lower flux rates generate a narrower height distribution of the more stable islands that decay slowly in time. For example, 3-layer islands are less stable than 4-layer islands and both of these are less stable than 7-layer islands. Correspondingly, the 3-layer islands decay very quickly at high fluxes followed by the 4-layer islands. At low flux, the 3-layer islands do not appear at all. It is curious that the 4-layer islands generated at low flux are not observed to decay. This could be related to the fact that these islands are larger in diameter. The average size of the 4-layer islands is 40 nm for low flux versus 18 nm for high flux rates. Thus, there could be a height-dependent critical lateral size defining whether a 4-layer island will decay or not. To account for the extremely fast decay times observed at high flux rates, collective effects must be operating that the detachment of a single atom can trigger highly correlated detachment of many more atoms. Although the microscopic origin of such processes still needs to be identified, they have tremendous implications about the self-organization in the epitaxial growth of nanocrystals.

In summary, the nucleation and coarsening of Pb islands grown on Si(111)-7×7 were studied to clarify the role of QSE in the final island morphology after coarsening. Complementary surface X-ray diffuse scattering and STM experiments show an unexpected and unusual flux rate dependence, a lack of scaling of the island densities, and island decay times that are orders of magnitude faster than expected from the classical analysis. Surprisingly, improved height and size distributions along with a much lower island density are observed after deposition at high rather than low flux rates, contrary to the classical scaling theory of nucleation and Ostwald ripening. The breakdown of the Gibbs-Thomson

effect that determines stability in terms of the island diameter is manifested in the lack of scaling of the island density as well as the remarkably fast time scales of the island decay. The evaporation of unstable 3-layer islands with 1000 atoms within less than 2 min suggests the presence of another far more efficient decay mechanism operating at low temperatures that is related to QSE. These discoveries have important ramifications for understanding the controlled growth of nanostructures and self-organization of nanostructures, especially at low temperatures, because they challenge standard wisdom and expectations in the field.

APPENDIX A

GEOMETRY CORRECTION

The geometry of real experiments affects the measured scattered X-ray intensities. Geometry-dependent corrections were applied to analyze the experimental data because these corrections are only subject to the scattering geometry, containing no information about the structure. Geometry corrections includes the polarization factor, the Lorentz factor, and the beam footprint area correction factor, all of which will be discussed below. The calculated scatting intensities will take into account these corrections by multiplying each of them.

The *polarization factor*, P, results from the different polarizations of the incoming and outgoing X-ray beams. In this work, the X-rays is polarized in the horizontal plane since the acceleration of the electrons in a synchrotron radiation source is in the horizontal plane. The polarization factor is given as $P = cos^2\phi$, where ϕ is the angle between the incident $\mathbf{k}_i$ and the projection of the outgoing $\mathbf{k}_f$ on the horizontal plane. When the scattering plane that determined by $\mathbf{k}_i$ and $\mathbf{k}_f$ is horizontal, ϕ is the angle between $\mathbf{k}_i$ and $\mathbf{k}_f$, $\phi = 2\theta$ and the polarization factor is, $P = \cos^2(2\theta)$. For vertical scattering plane, the polarization factor is $P = 1$.

The *Lorentz factor*, L, is the correction for integration volume change in angular space converting to that in reciprocal space.[9] Due to the sample defects, mosacity and angular dispersion of the beam etc, the scattered beam spreads in space. Therefore the actual intensity is obtained through integrating the scattered intensity within a finite region of reciprocal space. In practise, the integration is done in angular space because the scattered intensity is measured by scanning angles of the diffractometer. The integration intensity obtained in angular space can be converted to that in reciprocal space through the Lorentz factor. The Lorentz factor for the specular surface rod was given as $L = 1/\sin(2\theta)$ with rocking curve method.

The *Beam Footprint factor*, g_f, is the correction for the change of illuminated area of sample with different incident angle. The scattering intensity of a diffraction rod is proportional to the exposed area of the sample to the X-ray beam. In the specular geometry, the beam footprint seen from the detector is still the incident beam size, therefore it will not affect the detector angular acceptance. When the incident angle is small, the footprint of the beam on the sample might extend the sample size and the whole sample surface is illuminated. Otherwise a fraction of the sample surface is exposed, proportional to the beam footprint. the beam footprint correction is given as,

$$g_f = \begin{cases} 1 & \sin(\theta) \geq W_b/L_s \\ \sin(\theta)L_s/W_b & \sin(\theta) < W_b/L_s \end{cases} . \tag{A.1}$$

where θ is the incident angle to the sample surface, W_b is the beam width and L_s is the sample length.

The moment transfer vector, $\mathbf{q}$, with which theoretical models calculate the diffracted intensities, is calibrated as the internal wave vector in the film and the substrate, respectively. Since the refractive indexes for both the film and the substrate is greater than 1, according to Snell's law, the incident X-ray beam enters the sample with a smaller angle, θ', than its original angle θ. In specular geometry, the reflected angle of the beam within the sample is θ' as well. Here θ' and θ are angles relative to the horizontal surface planes. As a result, the moment transfer vector within the sample, $q' = 2k\sin(\theta')$ is smaller than that in vacuum $q = 2k\sin(\theta)$. The wave vector, q_c, resulted from the critical angle incidence is called the critical wave vector, below which the incident beam experiences total internal reflection. The internal moment transfer vectors in the sample are related to the critical wave vector,

$$q'_{\mathrm{Si}} = (q^2 - q_c(\mathrm{Si})^2)^{\frac{1}{2}} \tag{A.2}$$

$$q'_{\mathrm{Pb}} = (q^2 - q_c(\mathrm{Pb})^2)^{\frac{1}{2}}, \tag{A.3}$$

where q_c(Si) and q_c(Pb) are the critical wave vectors for Si and Pb, respectively.

REFERENCES

[1] M.Jalochowski, M.Hoffmann, and E.Bauer, Phys.Rev.B **51**, 7231 (1995).

[2] V.Yeh, L.berbil-Bautista, C.Z.Wang, K.M.Ho, M.C.Tringides, Phys. Rev. Letter. **85**, 5158 (2000).

[3] K.Budde, E.Abram, V.Yeh, M.C.Tringides, Phys.Rev. B **61**, R10602 (2000).

[4] M.Hupalo, S. Kremmer, V.Yeh, L.Berbil-Bautista, E.Abram, M.C.Tringides, Surf.Sci. **493**, 526 (2001).

[5] Z.Zhang, Q.Niu, and C-K. Shih, Phys.Rev.Lett. **80**, 5381 (1998).

[6] K.A.Edwards, P.B.Howes, J.E.Macdonald, T.Hibma, T.Bootsma, M.A.James, Surf.Sci. **424**, 169, (1999)

[7] I.K. Robinson and E. Vlieg, Surf. Sci. **261**, 123 (1991).

[8] E. Vlieg, A.W. Denier van der Gon, J.F. van der Veen, J.E. Macdonald and C. Norris *Surf. Sci.* **210**, 301 (1989).

[9] E.Vlige, J.Appl.Cryst. **30**, 532 (1997).

[10] K.Takayanagi, Y.Tanishiro, S.Takahashi, M.Takahashi, Surf.Sci. **277**, 367 (1985).

[11] N. V. Smith, N. B. Brookes, Y. Chang, and P. D. Johnson, Phys. Rev. B **49**, 332 (1994).

[12] C.M.Wei, M.Y.Chou, Phys. Rev. B **66**, 233408 (2002).

[13] K.R. Roos, M.C. Tringides, Phys. Rev. B **47**, 12705 (1993).

[14] A.Petkova, J.Wollschlager, H.L.Gunter, M.Henzler, Surf. Sci. **482**, 922 (2001).

[15] P.O.Hahn, J.Clabes, and M.Henzler, J.Appl.Phys. **51**, 2079 (1980).

[16] P.Czoschke, Hawoong Hong, L. Basile, and T.C. Chiang Phys. Rev. B **72**, 035305 (2005).

[17] Hawoong Hong, C.-M.Wei, M.Y.Chou, Z.Wu, L.Basile, H.Chen, M. Holt, and T.-C. Chiang, Phys.Rev.Lett **90**, 076104 (2003).

[18] T. -C. Chiang, Surf. Sci. Rep. **39**, 181 (2000).

[19] C.A.Lucas, D.Loretto, Surf. Sci. **344**, L1219, (1995)

[20] F.K.Schulte, Surf. Sci. **55**, 427, (1976)

[21] N. D. Lang and W. Kohn, Phys. Rev. B **3**, 1215 (1971).

[22] M.Jalochowski and E.Bauer, Phys.Rev.B **38**, 5272 (1988).

[23] P.J.Feibelman, Phys.Rev.B **27**, 1991 (1983).

[24] P.J.Feibelman, Phys.Rev.B **65**, 129902(E) (2002).

[25] M. Hupalo, V. Yeh, L. Berbil-Bautista, S. Kremmer, E. Abram, and M. C. Tringides. Phys. Rev. B **64**, 155307 (2001).

[26] J.A.Venable, G.D.T Spiller and M. Hanbuchen, Rep.Prog. Phys. **47**, 399 (1984).

[27] W.B.Su, S.H.Chang, W.B.Jian, C.S.Chang, L.J.Chen, and Tien T.Tsong, Phys.Rev.Lett. **86**, 5116 (2001).

[28] B.S.Swartzentruber, Y.-W.Mo, M.B.Webb, M.G.Lagally, J.Vac.Sci.Technol. A **7**, 2901 (1989).

[29] P.F.Miceli, C.J.Palmstrom, Phys. Rev.B **51**, 5506 (1995).

[30] A.R.Smith, K.-J.Chao, Q.Niu, and C.K.Shih, Science **273**, 226 (1996).

[31] M.Zinke-Allmang, L.C. Feldmann, and M.C.Grabow, Surf.Sci. Rep. **16**, 377 1992.

[32] K.Binder and D.Stauffer, Adv.Phys. **25**, 343 1976.

[33] H. You, J.Appl.Cryst., **32**, 614 (1999).

[34] P.Wynblatt and N.A.Gjostein, Prog.Solid State Chem. **9**, 21 (1975).

[35] K.Morgenstern, G.Rosenfeld, E.Lagsgaard, F.Besenbacher, and G.Comsa, Phys.Rev.Lett. **80**, 556 (1998).

[36] T.Michely, *J.Krug, Islands, Mounts and Atoms*, Springer-Verlag Berlin Heidelberg, Germany, 2004.

[37] G.Zinsmeister, Vacuum **16**, 529 (1966).

[38] T.Hibma, H.H. Weitering, D.R. Heslinga and T.M. Klapwijk, Appl.Surf.Sci. **48-49**, 209 (1991).

[39] A. Mans, J.H. Dil, A.R.H.F. Ettema and H.H. Weitering, Phys.Rev.B **66** 195410 (2002).

[40] Rui Feng, E.H. Conrad, M.C. Tringides, C. Kim, and P.F. Miceli, Appl.Phys.Lett. **85**, 3866 (2004).

[41] Rui Feng, E.H. Conrad, C. Kim, P.F. Miceli and M.C. Tringides, Physica B **357**, 175 (2005).

[42] J.-K.Zuo, J.F.Wendelken, H.Durr and C.-L.Liu, Phys.Rev.Lett **72**, 3064 (1994).

[43] I. K. Robinson and D. J. Tweet, Rep.Prog. Phys. **55**, 599 (1992).

[44] E.Ganz, I.S Hwang, F.Xiong, S.K. Theiss and J.Golovchenko Surf.Sci. **257**, 259 (1991).

[45] I.B. Altfeder, K.A. Matveev and D.M. Chen, Phys.Rev.Lett. **78** 2815 (1997).

[46] J. Als-Nielsen and D. McMorrow. *Elements of Modern X-Ray Physics,* John Wiley & Sons, Chichester, 2001.

[47] B. E. Warren. *X-ray Diffaction,* New York, 1969.

[48] L. H. Schwartz and J. B. Cohen. *Diffraction from Materials, second edition,* Springer-Verlag Berlin, Heidelberg, 1987.

[49] N. W. Ashcroft and N. D. Mermin. *Solid State Physics,* Harcourt College Publishers, Philadelphia, 1976.

[50] M.P.Marder. *Condensed Matter Physics*, John Wiley & Sons, New York, (2000).

[51] E.H. Conrad, *Handbook of Surface Science* ed. N.V Richardson and S. Holloway, Vol.1 p271-360, Elsevier, Amsterdam, (1996).

[52] J.D.Jackson. *Classical Electrodynamics*, John Wiley & Sons, New York, (1999).

[53] Hans Luth, *Surfaces and Interfaces of Solids*, Springer-Verlag, Beilin Heidelberg, (1993).

[54] I.M. Lifshitz, and V.V.Slyozov, J.Phys.Chem.Solids **19**, 585 (1961).

[55] B.Krishnamachari, J.McLean, B.Cooper, and J.Sethna, Phys.Rev.B **54**, 8899, (1996).

[56] Ruud M.Tromp, James B.Hannon, Surf.Revs & Letts, **9**, 1565, (2002).

[57] K. Thurmer, J. J. Reuut-Robey, E. D.Williams, M. Uwaha, A. Emundts, and H. P. Bonzel, Phys. Rev. Lett. **87**, 186102 (2001).

[58] M. Uwaha, J. Phys. Soc. Jpn. **57**, 1681 (1988).

[59] C.A.Jeffrey, E.H.Conrad, R.Feng, M.Hupalo, C.Kim, P.J.Ryan, P.F.Miceli, and M.C.Tringides, Phys.Rev.Lett. **96**, 106105 (2006).

[60] M.Nowicki, C.Bombis, A.Emundts, and H.P.Bonzel, Phys.Rev.B **67**, 075405 (2003).

[61] J.G.McLean, B.Krishnamachari, D.R.Peale, E.Chason, J.P.Sethna, and B.H.Cooper, Phys. Rev. B **55**, 1811 (1997).

[62] S.Y.Tong, H.Huang, C.M.Wei, W.E.Packard, F.K.Men, G.Glander and M.B.Webb J.Vac.Sci. Technol A **6(3)** 615 (1988).

VITA

Rui Feng was born in Anhui province, China, in 1975. She received a B.S in Electrical Science and Engineering from Nanjing University, Nanjing, China, in 1995. Then she worked for more than four years in NYK Line nanjing office. This enjoyable job did not stop her desire for advanced education. In 2000, she started her graduate study in USA. She received an M.S. in physics from Northern Illinois University in 2002 and her Ph.D. in physics from Georgia Tech in 2006.